ADAPTIVE DECISION-DIRECTED CHANNEL EQUALIZATION AND LASER PHASE NOISE INDUCED INTER-CARRIER-INTERFERENCE MITIGATION FOR COHERENT OPTICAL ORTHOGONAL FREQUENCY DIVISION MULTIPLEXING TRANSPORT SYSTEMS

MOHAMMAD EBRAHIM MOUSA PASANDI

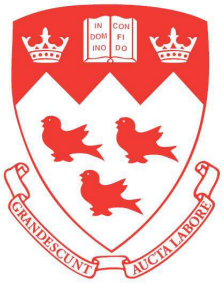

Department of Electrical and Computer Engineering
McGill University
Montreal, Canada

August 2012

A thesis submitted to the Faculty of Graduate Studies and Research in partial fulfillment of the requirements of the degree of Doctor of Philosophy

Abstract

The explosive growth of global Internet traffic has placed tremendous strain on both optical networks and optical transmission systems, underscoring the need for not only high-capacity transmission links but also for flexible, reconfigurable, and adaptive networks. Recent progress in complementary metal–oxide–semiconductor (CMOS) technology has facilitated the use of digital signal processing (DSP) in optical communication systems. Blessed with the revival of coherent optical transmission systems, over the past few years, DSP-enabled, software-defined optical transmission (SDOT) systems have led the fundamental paradigm shift from inflexible optical networks to robust, reconfigurable, plug-and-play optical networks.

Recently, coherent optical orthogonal frequency division multiplexing (CO-OFDM) has been intensively investigated as a promising modulation format for realizing coherent transmission systems. Although CO-OFDM has attracted significant interest in the research community, it has yet to leave a tangible impact on the commercial front due to implementation shortcomings, such as excessive overhead, and susceptibility to fibre nonlinearities and frequency/phase noise.

This thesis explores DSP-based solutions for CO-OFDM transmission systems, including two key original contributions. The first contribution is a novel adaptive decision-directed channel equalizer (ADDCE) that aims to reduce the required overhead in CO-OFDM transmission systems. ADDCE retrieves an estimation of the phase noise value after an initial decision making stage, by extracting and averaging the phase drift of all OFDM sub-channels, demonstrating zero-overhead phase noise compensation. Moreover, it updates the channel transfer matrix on a symbol-by-symbol basis, thus enabling a reduction in the associated overhead with pilot symbols. The second original contribution of this thesis focuses on the mitigation of the effect of the laser phase noise induced inter-carrier interference (ICI) in CO-OFDM systems. This interpolation-based ICI compensator estimates the time-domain phase noise samples using linear interpolation between the common-phase-error (CPE) estimates of consecutive OFDM symbols.

The performances of the aforementioned DSP equalization schemes are numerically and experimentally studied in reduced-guard-interval dual-polarization CO-OFDM (RGI-DP-CO-OFDM) transmission systems, and are found to demonstrate superior performance over conventional equalizers (CEs). In addition, a computational complexity analysis of the proposed equalizers is provided, which confirms a low implementation complexity.

Résumé

La croissance explosive du trafic globale sur Internet a crée une pression importante sur les réseaux optiques et les systèmes de transmission optiques; ce qui suggère le besoin de liens de transmission de haute capacité ainsi que de réseaux adaptables, reconfigurables et flexible. Les récents progrès dans les technologies de semiconducteurs métal-oxyde complémentaire (CMOS) ont facilité l'usage des traitements de signaux numériques (DSP) dans les systèmes de transmission optique. Grâce au retour en force du système de transmission optique cohérent ces dernières années, les systèmes de transmission optique régis par logiciel et supportés par les traitements de signaux numériques ont mené la transition fondamentale des réseaux optique inflexible vers des réseaux optique robuste, reconfigurable, prêt à brancher et utiliser.

Depuis peu, le format de modulation par multiplexage fréquentiel orthogonale en optique cohérente (CO-OFDM) est profondément étudier comme format de modulation particulièrement prometteur pour réaliser des systèmes de transmission cohérents. Malgré le fait que les CO-OFDM aient réussi à susciter un grand intérêt dans la communauté de recherche, ils leur restent encore à avoir un impact plus tangible dans le secteur commercial. Ce non-déploiement commercial est attribué aux difficultés d'implémentations, notamment à l'information superflue excessive nécessaire et à la susceptibilité accrue aux nonlinéarités de la fibre optique et aux bruits de fréquence et de phase.

Cette thèse explore certaines idées de DSP pour des systèmes de transmission CO-OFDM, incluant deux contributions originales. La première étant un égalisateur de canaux à adaptation dirigée par décision (ADDCE) qui vise à réduire l'information superflue nécessaire aux systèmes de transmission CO-OFDM. ADDCE récupère une estimation de la valeur du bruit de phase après un stage initiale de décision en extrayant et en moyennant la dérive de phase de tout les sous-canaux OFDM, ce qui démontre une compensation du bruit de phase sans information superflue. De plus, cela ajourne la matrice de transfère du canal optique symbole par symbole, offrant une réduction de l'information excédante associés avec les symboles pilotes. La seconde contribution de cette thèse se concentre sur la mitiga-

tion de l'interférence inter-canaux (ICI) induite par le bruit de phase du laser dans les systèmes CO-OFDM. Ce compensateur de ICI basé sur l'interpolation estime le bruit de phase des échantillons dans le temps en utilisant une interpolation linéaire entre les estimations d'erreur de phase commune (CPE) de symboles OFDM consécutifs.

Les performances des algorithmes d'égalisations appliqués en DSP mentionnés ci-haut sont étudiées en simulations et expérimentalement dans un système de transmission en CO-OFDM sur double polarisation à intervalle de garde réduite (RGI-DP-CO-OFDM), ce qui démontre une performance supérieure vis-à-vis de l'égalisateur conventionnel (CEs). Plus encore, l'analyse de la complexité des algorithmes d'égalisateurs proposées sera fournit; confirmant une implémentation à faible complexité.

Acknowledgment

First and foremost, I offer my sincerest gratitude to my supervisor, Professor David V. Plant, for his endless encouragement, support and guidance. His insight and knowledge makes him an excellent professor, but his gentle, intelligence, and compassionate character makes him a remarkable person. In spite of his busy schedule, I never had any difficulty to arrange a meeting with him to discuss scientific or personal problems, and I always enjoyed his intelligence and vision. It is my great honour to be his student.

Many thanks to my talented colleagues: Benoît Châtelain, Zhaoyi Pan, Qunbi Zhuge, Xian Xu, Mathieu Chagnon, Mohamed Morsy-Osmen, Jon Buset and all the rest, who helped me in various forms to finalize this project. As a part of the work in this thesis, an experimental coherent optical transmission setup was realized in which my deep expression of appreciation goes to Benoit, Zhaoyi, Qunbi, and Xian for their invaluable help, motivating discussions and the contribution in the signal processing aspects.

I would like to acknowledge Professor Tho Le-Ngoc for providing the real-time oscilloscope in the early stage of the experiments. I would like to thank the entire Photonic Systems Group (PSG) and SYTACom staff especially Chris Rolston for their assistance.

Beyond optical fibre communications, which sometimes seemed to be nothing more than a never-ending race, I would like to acknowledge my friends in McGill Outdoors Club (MOC) for the fantastic outdoorsy experiences throughout the past four years. Special thanks to my best friend, my brother, Major Johnny Hlibchuk, for his friendship, generosity in sharing his invaluable life experiences and above all, the great time that we spent in mountains or on the saddle of our touring bikes!

My deepest love and appreciation goes to my parents for their support, kindness and patience in all and every stage of my life. They devoted their heart and soul to advance my education and encourage me to love learning and hardworking.

My sincere gratitude to you all,

Mohammad Ebrahim Mousa Pasandi

Publications and Contributions of the Author

The originality of the content of this thesis is manifested by several peer-reviewed journal and conference publications. These publications are in the form of 5 journal articles and 4 conference proceedings. In addition, the author of this thesis has contributed as the author and co-author of several other publications namely, 5 journal articles and 11 conference proceedings, which are not directly related to the content of this thesis. The list of the publications of the author of this thesis is noted below.

Referred Journal Articles Related to This Thesis

1. **M. E. Mousa Pasandi**, and D. V. Plant, "Data-aided adaptive weighted channel equalizer for long-haul optical OFDM transmission systems," Opt. Express 18, pp. 3919-3927 (2010).
2. **M. E. Mousa Pasandi**, and D. V. Plant, "Zero-overhead phase noise compensation via decision-directed phase equalizer for coherent optical OFDM," Opt. Express 18, pp. 20651-20660 (2010).
3. **M. E. Mousa Pasandi**, and D. V. Plant, "Non-iterative interpolation-based phase noise ICI mitigation for CO-OFDM transport systems," IEEE Photon. Technol. Lett. 23, pp. 1594-1596 (2011).
4. **M. E. Mousa-Pasandi**, Q. Zhuge, X. Xu, M. M. Osman, Z. A. El-Sahn, M. Chagnon, and D. V. Plant, "Experimental demonstration of non-iterative interpolation-based partial ICI compensation in 100G RGI-DP-CO-OFDM transport systems," Opt. Express 20, pp. 14825-14832 (2012).
5. **M. E. Mousa-Pasandi**, Q. Zhuge, X. Xu, M. M. Osman, M. Chagnon, and D. V. Plant, "Experimental Study of a novel adaptive decision-directed channel equalizer in 28 GBaud RGI-DP-CO-OFDM transport systems," Opt. Express 20, pp. 17017-17028 (2012).

Referred Conference Articles Related to This Thesis

1. **M. E. Mousa Pasandi**, J. Haghighat, and D. V. Plant, "Adaptive weighted channel equalizer for direct-detection optical OFDM transmission systems," in Proceedings of IEEE Photonics Society Summer Topicals'09, (Institute of Electrical and Electronics Engineers, New York, 2009), pp. 85-86.
2. **M. E. Mousa Pasandi**, and D. V. Plant, "OFDM data-aided channel equalizer for already-deployed direct-detection transmission systems," in Proceedings of IEEE Photonics Society Annual Meeting'09, (Institute of Electrical and Electronics Engineers, New York, 2009), pp. 717-718.
3. **M. E. Mousa Pasandi**, and D. V. Plant, "Improvement of phase noise compensation for coherent optical OFDM via data-aided phase equalizer," in National Fibre Optic Engineers Conference, OSA Technical Digest (CD) (Optical Society of America, 2010), paper JThA10.
4. **M. E. Mousa Pasandi**, and D. V. Plant, "Non-iterative interpolation-based phase noise ICI mitigation for CO-OFDM transport systems," in Signal Processing in Photonic Communications, OSA Technical Digest (CD) (Optical Society of America, 2011), paper SPMB6.

Referred Journal Articles not Directly Related to This Thesis

1. Y. Kim, S. Doucet, **M. E. Mousa Pasandi**, and S. LaRochelle, "Optical multicarrier generator for radio-over-fibre systems," Optics Express 16, pp. 1068-1076 (2008).
2. **M. E. Mousa Pasandi**, M. M. Sisto, S. Doucet, Y. Kim, S. LaRochelle, and L. A. Rusch, "Low-distortion optical null-steering beamformer for radio-over-fibre OFDM systems," IEEE J. Lightwave Technol. 27, No. 22, pp. 5173-5182 (2009).
3. Q. Zhuge, X. Xu, Z. A. El-Sahn, **M. E. Mousa-Pasandi**, M. Morsy-Osman, M. Chagnon, M. Qiu, and D. V. Plant, "Experimental investigation of the equalization-enhanced phase noise in long haul 56 Gbaud DP-QPSK systems," Opt. Express 20, 13841-13846 (2012).
4. Q. Zhuge, **M. E. Mousa-Pasandi**, M. M. Osman, X. Xu, M. Chagnon, Z. A. El-Sahn, -enhanced phase noise in RGI CO-noisrepsid fo noitartsnomeD" ,Plant .V .and D .(2012) .Lett .Technol .notohP EEEI ni noitacilbup rof detpecca ",OFDM systems

5. Q. Zhuge, X. Xu, Z. A. El-Sahn, **M. E. Mousa-Pasandi**, M. Morsy-Osman, M. Chagnon, M. Qiu, and D. V. Plant, "Pilot-aided carrier phase recovery for M-QAM using superscalar parallelization based PLL," submitted to Opt. Express (2012).

Referred Conference Articles not Directly Related to This Thesis

1. M. M. Sisto, **M. E. Mousa Pasandi**, S. Doucet, S. LaRochelle, and L. A. Rusch, "Optical phase and amplitude control for beamforming with multiwavelength Gires-Tournois Bragg grating cavities," in the Proceedings of the Fourth IASTED Internationl Conference on Antennas, Radar and Wave (International Association of Science and Technology for Development, Montreal, Quebec, 2007), pp. 238-243.
2. **M. E. Mousa Pasandi**, M. M. Sisto, S. LaRochelle, and L. A. Rusch, "Low distortion null-steering beamforming with a cascade of fibre Bragg grating Gires-Tournois," in Proceedings of IEEE Photonics Society Annual Meeting'07, (Institute of Electrical and Electronics Engineers, New York, 2007), pp. 114-115.
3. I. A. Kostko, **M. E. Mousa Pasandi**, M. M. Sisto, S. Larochelle, L. A. Rusch, and D. V. Plant, "A radio-over-fibre link for OFDM transmission without RF amplification," in Proceedings of IEEE Photonics Society Annual Meeting'07, (Institute of Electrical and Electronics Engineers, New York, 2007), pp. 339-340.
4. R. Liu, **M. E. Mousa Pasandi**, S. LaRochelle, J. Yao, K. Wu, and R. Kashyap, "OFDM signal transmission by direct modulation of a doped fibre external cavity semiconductor laser," in Optical Fibre Communication Conference and Exposition and The National Fibre Optic Engineers Conference, OSA Technical Digest (CD) (Optical Society of America, 2008), paper OThN5.
5. Y. Kim, **M. E. Mousa Pasandi**, S. Doucet, L. Rusch, and S. LaRochelle, "OSNR requirements for optical multicarrier generator for short range radio-over-fibre systems," in Conference on Lasers and Electro-Optics/International Quantum Electronics Conference, OSA Technical Digest (CD) (Optical Society of America, 2009), paper CTuJ6.
6. M. M. Sisto, **M. E. Mousa Pasandi**, L. A. Rusch, and S. LaRochelle, "Optical phase and amplitude control for beamforming with cascades of Gires-Tournois Bragg grating

filters," in Optical Fibre Communication Conference, OSA Technical Digest (CD) (Optical Society of America, 2010), paper OThF3.

7. C. Chen, **M. E. Mousa Pasandi**, K. Choquette, and D. V. Plant, "Transmission experiment using a coupled-cavity VCSEL for radio frequency conversion," in Optical Fibre Communication Conference, OSA Technical Digest (CD) (Optical Society of America, 2011), paper OThG3.
8. Q. Zhuge, **M. E. Mousa-Pasandi**, M. Morsy-Osman, X. Xu, M. Chagnon, Z. Elsahn, and D. Plant, "High Performance, Low Overhead CO-OFDM for Next Generation Fibre Transmission Systems," in Signal Processing in Photonic Communications, OSA Technical Digest (online) (Optical Society of America, 2012), paper SpTu2A.4.
9. Q. Zhuge, **M. E. Mousa-Pasandi**, X. Xu, B. Chatelain, Z. Pan, M. Osman, and D. V. Plant, "Linewidth-tolerant low complexity pilot-aided carrier phase recovery for M-QAM using superscalar parallelization," in Optical Fibre Communication Conference, OSA Technical Digest (Optical Society of America, 2012), paper OTu2G.2.
10. M. M. Osman, M. Chagnon, Q. Zhuge, X. Xu, **M. E. Mousa-Pasandi**, Z. A. El-Sahn, L. Chen, and D. V. Plant, "Training symbol based channel estimation for ultrafast polarization demultiplexing in coherent transmission single-carrier systems with M-QAM constellations," accepted to the European Conference on Optical Communication (2012).
11. Q. Zhuge, M. M. Osman, **M. E. Mousa-Pasandi**, X. Xu, M. Chagnon, Z. A. El-Sahn, C. Chen, and D. V. Plant, "Experimental demonstration of 28 Gbaud QPSK and 16-QAM zero-guard-interval CO-OFDM transmissions," accepted to the European Conference on Optical Communication (2012).

Contents

List of Figures

List of Tables

List of Abbreviations

ADC	Analog-to-Digital Converter
ADCCE	Adaptive Decision Directed Channel Equalizer
AOS	Acousto-Optic Switch
ASE	Accumulated Spontaneous Emission
ASIC	Application Specific Integrated Circuit
AWCE	Adaptive Weighted Channel Equalizer
AWG	Arbitrary Waveform Generator
B2B	Back to Back
BER	Bit Error Rate
BP	Back Propagation
CD	Chromatic Dispersion
CE	Conventional Equalizer
CLB	Configurable Logic Block
CMA	Constant Module Algorithm
CMOS	Complementary Metal Oxide Semiconductor
CO-OFDM	Coherent Optical Orthogonal Frequency Division Multiplexing
CP	Cyclic Prefix
CPE	Common Phase Error
CW	Continuous Wave
DAC	Digital-to-Analog Converter

DC	Direct Current
DCF	Dispersion Compensation Fibre
DDPE	Decision Directed Phase Equalizer
DEPN	Dispersion Enhanced Phase Noise
DFB	Distributed Feedback
DFE	Decision Feedback Equalizer
DFT	Discrete Fourier Transform
DGD	Differential Group Delay
DP	Dual Polarization
DPSK	Differential Phase Shift Keying
DSB	Double Side Band
DSL	Digital Subscriber Loop
DSP	Digital Signal Processing
DWDM	Dense Wavelength Division Multiplexing
ECL	External Cavity Laser
EDA	Electronic Design Automation
EDC	Electronic Dispersion Compensation
EDFA	Erbium Doped Fibre Amplifier
ENoB	Effective Number of Bits
E/O	Electro Optic
FDE	Frequency Domain Equalization
FDM	Frequency Division Multiplexing

FEC	Forward Error Correction
FFT	Fast Fourier Transform
FIR	Finite Impulse Response
FPGA	Field Programmable Gate Array
GML	Grouped Maximum Likelihood
ICI	Inter Carrier Interference
IDFT	Inverse Discrete Fourier Transform
IF	Intermediate Frequency
IFFT	Inverse Fast Fourier Transform
I/Q	In-phase/Quadrature
ISI	Inter Symbol Interference
ISFA	Inter-Symbol Frequency-Domain Averaging
LO	Local Oscillator
LPF	Low Pass Filter
LS	Least Square
MIMO	Multiple Input Multiple Output
ML	Maximum Likelihood
MZM	Mach-Zehnder Modulator
NGI	No Guard Interval
NRZ	Non Return to Zero
ODL	Optical Delay Line
O/E	Opto Electronic

OFDE	Overlapped Frequency Domain Equalizer
OFDM	Orthogonal Frequency Division Multiplexing
OOK	On Off Keying
OSA	Optical Spectrum Analyzer
OSNR	Optical Signal to Noise Ratio
PAPR	Peak to Average Power Ratio
PBS	Polarization Beam Splitter
PD	Photo Detector
PDL	Polarization Dependent Loss
PM	Phase Modulator
PMD	Polarization Mode Dispersion
PRBS	Pseudo Random Bit Sequence
PS	Pilot Symbol
PSC	Pilot Subcarrier
PSR	Pilot to Signal Ratio
QAM	Quadrature Amplitude Modulation
QPSK	Quadrature Phase Shift Keying
RF	Radio Frequency
RGI	Reduced Guard Interval
RODM	Reconfigurable Optical Add/Drop Multiplexer
RZ	Return to Zero
SC	Single Carrier

SDR	Software Defined Radio
SM	Single Mode
SMF	Single Mode Fibre
SDOT	Software Defined Optical Transmission
SISO	Single Input Single Output
SITO	Single Input Two Output
SNR	Signal to Noise Ratio
SSB	Single Side Band
SSMF	Standard Single Mode Fibre
TIA	Trans Impedance Amplifier
TISO	Two Input Single Output
TITO	Two Input Two Output
TS	Training Sequence
VHDL	VHSIC Hardware Description Language
WDM	Wavelength Division Multiplexing
WLAN	Wireless Local Area Network
WSS	Wavelength Selective Switch
XPM	Cross Phase Modulation
ZF	Zero Forcing

List of Symbols

$\vec{\alpha}$	PDL vector
β	two-sided 3-dB bandwidth of the phase noise process
$\vec{\beta}$	birefringence vector
γ	weighting parameter
Δ_G	length of the guard interval
Δf	subcarrier spacing
$\Delta OSNR_{PS}$	OSNR penalty due to pilot symbol insertion
$\Delta OSNR_{PSC}$	OSNR penalty due to pilot subcarrier insertion
$\Delta OSNR_{CP}$	OSNR penalty due to cyclic prefix insertion
$\overline{\theta}$	The vector of actual phase noise samples
ϕ_n^i	phase rotation at the n^{th} sample of the i^{th} OFDM symbol in time-domain
ϕ_D	phase dispersion due to the fibre chromatic dispersion
$\vec{\sigma}$	the Pauli matrix vector
σ	standard deviation of the noise for each subcarrier
Φ_{uu}	the auto-correlation matrix of u
$\Phi_{\theta u}$	the cross-correlation matrix between $\overline{\theta}$ and u
$A(t)$	generated OFDM waveform in time-domain
$\vec{A}(t)$	generated OFDM waveform vector in time-domain

A_l	l^{th} sample of the transmitted digital signal in time-domain
a_k	waveform of the k^{th} subcarrier
B	bandwidth of single-carrier signal
$B(t)$	received OFDM signal in time-domain
$B_c(t)$	frequency offset compensated signal in time-domain
B_l	l^{th} sample of the received digital signal in time-domain
C_{ADDCE}	complexity of the adaptive decision-directed channel equalizer
C_{CE}	complexity of conventional equalizer
C_{ICI}	complexity of the ICI compensator
CPE_i	common-phase-error for the i^{th} OFDM symbol
c	frequency-domain representation of the transmitted signal
c_0	speed of light
$c_{i,k}$	transmitted data symbol of the i^{th} symbol at the k^{th} subcarrier
$\vec{c}_{i,k}$	transmitted data vector of the i^{th} frame at the k^{th} subcarrier
$c'_{ki}(t)$	detected data symbol of the i^{th} symbol at the k^{th} subcarrier via matched filter
$\vec{c}'_{i,k}$	detected data vector of the i^{th} frame at the k^{th} subcarrier via matched filter
$DGD_{\max}$	maximum budget of the differential-group-delay
D_t	accumulated CD in the fibre link
$\hat{d}$	estimated DFT window timing

$\vec{e}$	error vector
f_k	centre frequency of the k^{th} subcarrier
f_{off}	frequency offset
$\hat{f}_{off}$	estimated frequency offset
f_0	frequency of the optical carrier
G	interpolation matrix
G_L	linear interpolation matrix
H	frequency-domain representation of the channel transfer matrix
$H_{i,k}$	frequency-domain representation of the channel transfer matrix for the i^{th} frame at the k^{th} subcarrier
h	frequency-domain representation of the channel transfer factor
$h_{i,k}$	frequency-domain representation of the channel transfer factor for the i^{th} symbol at the k^{th} subcarrier
h_k	frequency-domain representation of the channel transfer factor at the k^{th} subcarrier
h_k^{ISFA}	frequency-domain representation of the channel transfer factor at the k^{th} subcarrier by intra-symbol frequency-domain averaging
h_k^{ML}	frequency-domain representation of the channel transfer factor at the k^{th} subcarrier by maximum-likelihood
J	Jones matrix for the fibre link
M	number of bits per symbol

M_d	timing metric
m_{PS}	number of pilot symbols in a data block
m_{SYM}	number of data symbols in a data block
N_C	number of carriers in multi-carrier signal
N_{CD}	minimum number of equalizer taps for CD compensation
N_{CE}	number of data symbols in each block
N_{mc}	number of carrier in multi-carrier signal
N_{PMD}	number of PMD/PDL cascading elements in the fibre link
N_{PSC}	number of pilot subcarriers
N_{SC}	number of subcarrier in OFDM signal
N_1	FFT length of the first static FDE
N_2	FFT length of the second static FDE
N_3	FFT length of ICI harmonic estimator
n_{MP}	oversampling ratio
n'_{MP}	modified FDE oversampling ratio
$p_{i,k}$	k^{th} phase noise spectral component of the i^{th} OFDM symbol
Q	number of estimated harmonics in ICI compensator
R_{CE}	training symbol overhead
R_d	time-domain correlation function
r	frequency-domain representation of the received signal

$r_{i,k}$ frequency-domain representation of the received data symbol of the i^{th} symbol at the k^{th} subcarrier

$\vec{r}_{i,k}$ frequency-domain representation of the received data vector of the i^{th} frame at the k^{th} subcarrier before static overlapped frequency-domain equalizer

$\vec{\hat{r}}_{i,k}$ frequency-domain representation of the received data vector of the i^{th} frame at the k^{th} subcarrier after static overlapped frequency-domain equalizer

$\hat{S}_{i,k}$ subcarrier-specific equalized complex value symbol of the i^{th} symbol at the k^{th} subcarrier

$\vec{\hat{S}}_{i,k}$ subcarrier-specific equalized complex value vector of the i^{th} frame at the k^{th} subcarrier

$\vec{\bar{S}}_{i,k}$ subcarrier-specific detected complex value vector of the i^{th} frame at the k^{th} subcarrier for decision-directed estimation

$\bar{S}_{i,k}$ subcarrier-specific detected complex value symbol of the i^{th} symbol at the k^{th} subcarrier for decision-directed estimation

T_{mc} symbol duration of multi-carrier signal

T_s symbol duration of OFDM signal

T_{sc} symbol duration of single-carrier signal

t_d length of the channel delay spread

$w(n)$ additive noise

Chapter 1

Introduction

1.1. Overview

The arrival of the Internet deeply changed underlying communication infrastructures. The demand for high-capacity, long-haul communication systems is drastically increasing and annual global Internet traffic is expected to reach the zettabyte level by the end of 2015 [1]. Figure 1.1 shows Cisco's projection of global mobile data traffic for the year 2016. In 2011 alone, global mobile data traffic grew 2.3-fold, more than doubling for the fourth year in a row with an increase that was higher than anticipated [2]. Such phenomenal growth puts tremendous pressure on the existing infrastructures at every technological level from core to metro, and even on access networks, to increase the transmission throughput by ex-

ploiting the bandwidth, lengthening transmission reach, and having higher signal quality standards [3].

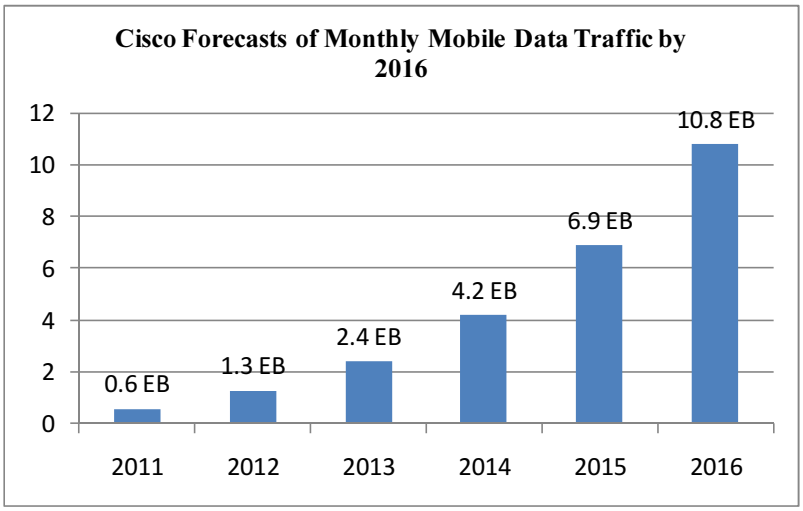

Figure 1-1: Cisco Forecasts 10.8 Exabytes per Month of Mobile Data Traffic by 2016 [2].

Optical fibre communication systems became possible due to the development of low-loss silica fibres and efficient double-hetero structure semiconductor lasers in the 1970s and the invention of the erbium-doped-fibre-amplifier (EDFA) in the 1980s; these led to rapid advances in wavelength-division multiplexing (WDM) and long-haul transmission systems [4,5]. In recent years, the realization of coherent detection as the most promising detection technique for achieving high spectral efficiency while maximizing power efficiency, combined with polarization multiplexing, allowed information to be encoded in all available degrees of freedom namely, in both the amplitude and phase of the electric field along with the two optical polarizations [6-8]. Once the outputs of an optoelectronic down-converter are sampled at the Nyquist rate, the digitized waveforms preserve full information of the electric field. This enables pre- and/or post-compensation of the fibre transmission impairments using digital signal processing (DSP) algorithms. Figure 1.2 depicts the trend in transmission capacity over the past three decades for both research and commercial systems. As can be seen, DSP-based transmission systems, combined with advanced modulation formats and WDM architecture, are pushing the record capacity higher and higher.

Optical transmission systems can generally be categorized into single-carrier and multi-carrier systems. The single-carrier scheme has been implemented in mainstream usage; it uses one carrier frequency, or equivalently wavelength, to transmit the data. In multi-carrier systems, however, the transmitted data is divided into many lower rate parallel streams to be transmitted over multiple carrier frequencies. Orthogonal frequency-division multiplexing (OFDM), patented in the U.S. in 1970 [9], is a particular form of multi-carrier transmission with densely spaced subcarriers and overlapping spectra.

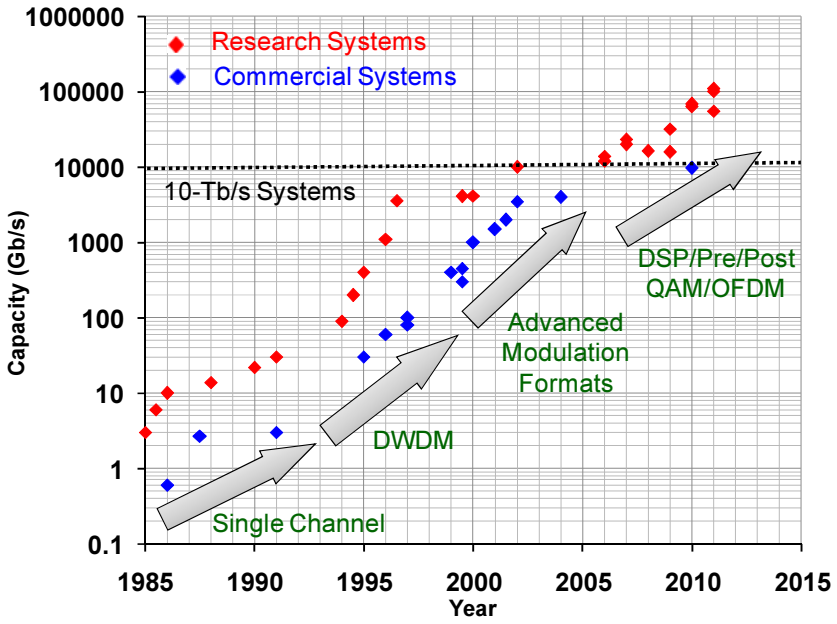

Figure 1-2: The trend of capacity versus year for optical fibre transmission systems.

Coherent Optical OFDM (CO-OFDM) combines the advantages of coherent detection and OFDM modulation [10]. It is robust to chromatic dispersion (CD) and polarization mode dispersion (PMD) with the introduction of the cyclic prefix (CP). Moreover, it enjoys easy channel equalization since the channel response can be estimated and further equalized on a subcarrier basis. With high spectral efficiency due to the subcarriers overlapping in the frequency-domain, CO-OFDM can also alleviate the required oversampling ratio and consequently the required electrical bandwidth at the transmitter and the receiver [10-12].

Since CO-OFDM emerged as an attractive modulation format in 2006, it has been considered an upgrade solution for the future of high-speed optical networks. Although, it has managed to attract a significant amount of research interest, it has yet to leave a tangible impact on the commercial front, compared to its single-carrier counterpart. This could be due to the following three factors: (i) both the research and industrial communities have been familiar with the implementation of the single-carrier scheme for decades (ii) coherent optical single-carrier transmission systems also managed to adopt novel, DSP-based compensation algorithms to achieve higher spectral efficiency and equalization performance (iii) CO-OFDM systems struggle as a viable and commercially reliable scenario due to their sensitivity to frequency/phase noise, fibre nonlinearity, and the excessive required overhead.

In this chapter, we briefly identify new trends in optical communication networks arising from rapid traffic growth, merging applications, and advancements in complementary metal–oxide–semiconductor (CMOS) technology. A brief background on CO-OFDM transports systems, and their associated merits, is provided. Then, we continue with a discussion regarding the original contributions of this work, and finally we layout this thesis.

1.2. New Era in Optical Fibre Communications

Ethernet via optical networks has become the undisputed technology of choice in terms of both cost and reliability [10]. In such systems, there are two major factors motivating the increase of transmission rates beyond the current capacity. The first is the explosive growth of bandwidth-rich applications [2]. Considering the phenomenal traffic growth due to the emergence of new applications, such as video communications and Internet TV, new requirements for both legacy and new optical networks have to be considered to cope with this ever-growing demand for bandwidth. Second, the migration of transmission systems to higher capacity is expected to reduce the installation, design, maintenance, and operational costs, together known by the term “dollar per transmitted bit”. In the following sections, we briefly explain a few trends in optical networks, taking into consideration the aforementioned requirements.

1.2.1. Dynamically Reconfiguration Networks

Although the link capacity can be enhanced through migration of the transmission speed to 400 Gb/s or 1 Tb/s, or by filling up more WDM channels, such growth of the optical transport capacity works only when transmitting information between point-to-point networks. However, transmission systems in the context of an optical network are required to dynamically add, drop, and route the wavelength channels at many individual nodes in order to accommodate the ever-changing pattern of data traffic. Reconfigurable optical add/drop multiplexers (ROADM) are known as a form of all-optical bandwidth management to save on unnecessary transponder costs associated with the optical-to-electrical (O/E) and electrical-to-optical (E/O) conversions [13,14].

The trend toward reconfigurable networks with transport speeds beyond 100 Gb/s poses three major challenges to the network design. First, the signal is extremely sensitive to the CD, PMD, ROADM filtering effects, and the imperfection of the optoelectronic components [15]. Second, to support long-haul transmission, optical PMD compensation is compulsory; however, optical PMD compensators are known to be lossy, bulky, and expensive. Third, conventional optical networks are inflexible compared to their radio frequency (RF) counterparts since they are more difficult to install, maintain, monitor, and administrate [10,14]. As such, an adaptive optical transmission system for an agile and reconfigurable optical network is essential for supporting high capacities and the ever-evolving user demand.

1.2.2. Digital Signal Processing (DSP) in Optical Fibre Communication Systems

Legacy optical transmission systems employ a dispersion management scheme that places a dispersion compensation fibre (DCF), usually at the amplification units, to compensate for the dispersion of the transmission link. The DCF could be distributed in a dispersion-mapped span [4]. Although such dispersion compensation schemes work well for transmission systems at 10 Gb/s and lower, it is challenging to perfect at 40 Gb/s and higher as both the cumulative CD and the CD slope of the DCF need to precisely match

those of the optical fibre link [16]. Any residual mismatched dispersion needs to be compensated for, using tunable optical dispersion modules. In addition, PMD tracking and compensation is essential for systems with rates of 40 Gb/s and higher. Deployment of optical PMD compensators at the receiver also is lossy, bulky, and expensive [17].

Following the recent progress in manufacturing ultra high-speed analog-to-digital converters (ADC) and digital-to-analog-converters (DAC) in CMOS technology, there has been great interest in using electronic digital signal processing (DSP) and electronic equalizers as replacements for all-optical compensating modules. Compared to their optical counterparts, the electronic equalizers offer smaller footprints, higher adaptability, and the crucial advantage of lower cost. A major breakthrough in DSP technology for optical transport systems happened in 2004 when researchers from Nortel published their pre-distortion equalizer that demonstrated 5000 km transmission over standard single-mode fibre (SSMF) without the need for an optical dispersion compensator [18]. This work was followed by the subsequent revival of coherent optical communications, leading to an abundance of research on the topics of DSP-based single-carrier and multi-carrier transmission systems [10,19,20].

1.2.3. Software-Defined Optical Transmission

In the 1980s, the concept of software-defined radio (SDR) was introduced in wireless communications to facilitate dynamically adapting to the multi-user environment with different analog and digital standards, instead of relying on dedicated hardware units [21]. For modern optical transmission systems, the emergence of multiple advanced modulation formats for the existing 40 Gb/s and 100 Gb/s, as well as the next-generation 400 Gb/s and 1 Tb/s, Ethernet transport systems motivates the same tendency towards software-defined optical transmission (SDOT). With SDOT, the transponder can be adapted to multiple standards and/or multiple modulation formats. An intelligent SDOT can also dynamically set up the physical link without human intervention and can accurately report the channel parameters, such as optical-signal-to-noise-ratio (OSNR), CD, and PMD [22].

The introduction of SDOT places the focus on automation and reconfigurability, and will inevitably lower the associated operational costs. Figure 1.3 depicts the basic diagram of a point-to-point optical network based on SDOT. The DSP-enabled SDOT will be leading the fundamental paradigm shift from inflexible optical networks to robust, plug-and-play optical networks in the near future [10,23].

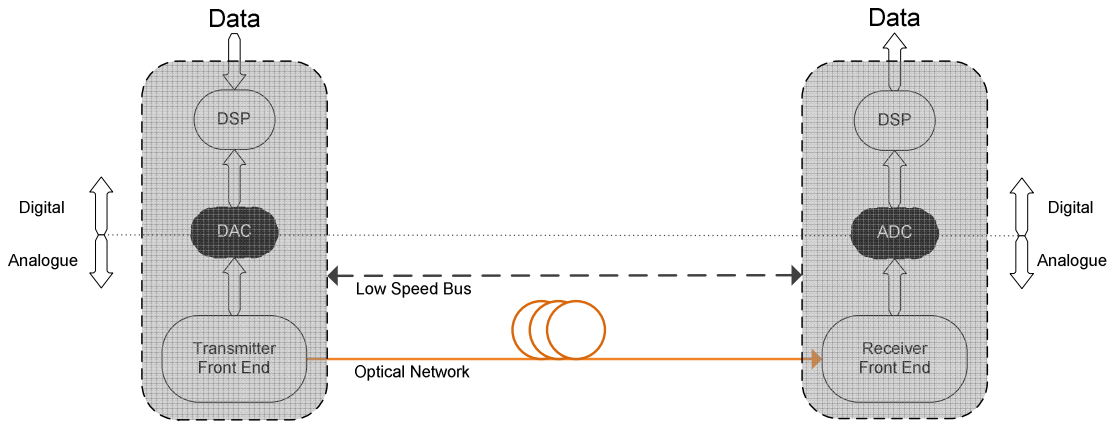

Figure 1-3: Diagram of a software-defined optical transport system.

1.3. CO-OFDM in Optical Fibre Communications

Orthogonal frequency division multiplexing (OFDM) is a special class of multi-carrier modulation that has been exploited in almost every major wireless communication standard, including wireless LAN (IEEE 802.11 a/g, also known as Wi-Fi), digital video and audio standards (DAV/DAB), and digital subscriber loop (DSL). In addition, the two competing fourth-generation (4G) mobile network standards, worldwide interoperability for microwave access (WiMAX, or IEEE 802.16) from the computing community, and long term evolution (LTE) from the telecommunication community, have both adopted OFDM as the core of their physical layer interface.

In the optical communication community, OFDM has recently gained attention, especially after being proposed as an attractive long-haul transmission format in coherent and direct detection [10,11,24]. Experiments on CO-OFDM transmission at 400 Gb/s and 1

Tb/s by various groups have placed optical OFDM in the race as a candidate for the next generation of Ethernet transport systems [25,26,27].

Although the arrival of CO-OFDM is recent, it has inherited a similar controversy to that which is familiar in the wireless community—the debate about the superiority of single-carrier versus multi-carrier transmission [28]. However, the objective of this thesis is not to compare single-carrier and OFDM approaches. It is known that OFDM is advantageous with regard to computational efficiency due to the use of the fast Fourier transform (FFT) and oversampling ratio; however, the single-carrier that incorporates cyclic prefix based on blocked transmission and pulse-shaping can achieve the same purpose [10]. The major advantages of CO-OFDM have to do with the following three unique intrinsic features: (i) it can support scalable spectrum partitioning from individual subcarriers to a sub-band, up to the entire OFDM spectrum, which provides flexibility at the device level and also at the system level compared to single-carrier transmission; (ii) it is straightforward to incorporate pilot symbols and subcarriers simultaneously with the data subcarriers, enabling rapid and convenient schemes for both monitoring and estimating the optical channel; and (iii) it supports adaptive transmission via bit and power loading to optimize the transmission rate and power of each subcarrier, based on the channel characteristics, to mutually maximize the bandwidth efficiency and the signal quality.

With features of new generation, reconfigurable, software-defined, agile, optical networks in mind from section 1.2, over the next few subsections we briefly discuss selected interesting characteristics of CO-OFDM systems.

1.3.1. Scalability to Ultra High-Speed Transmission

Considering the investment and effort required to redesign and reinstall transmission systems, it is critical to identify a technology with maximum possible life span that can be adapted to the next generation of the products with minimum modification in the physical layer. CO-OFDM may be one of the ideal future-proof technologies that can be scaled to ever-increasing transmission speeds. Since the data in CO-OFDM is managed in the frequency-domain, it is relatively simple to partition the entire broad OFDM spectrum into

many sub-bands whenever a bandwidth bottleneck occurs for the DAC/ADC signal processing elements. The sub-bands can be very closely spaced in such way that the intrinsic orthogonality between subcarriers extends to the sub-bands and therefore, the spectral efficiency would not be compromised. This technique ensures a smooth migration path of CO-OFDM from 40 Gb/s up to not only 100 Gb/s but also to 1 Tb/s, by expanding the spectrum via OFDM band-multiplexing. By doing so, the hardware and software designs developed for 40 Gb/s will very likely be reusable at 100 Gb/s, or even at 1 Tb/s, without a major design overhaul.

1.3.2. Transmission Agnostic to the Physical Link

The optical fibre links deployed over the past three decades comprise fibres with different CD, PMD, and loss, as well as varying span distances and mechanical stabilities [10]. Such a large divergence in the design and implementation parameters makes it difficult for conventional modulation formats, such as direct-detection non-return-to-zero (NRZ) and return-to-zero (RZ) on-off-keying (OOK), or differential-phase-shift-keying (DPSK), to meet the challenges for high-speed transmission. CO-OFDM, with its convenient method of adaptive equalization based on the pilot subcarriers and pilot symbols, is an ideal candidate for meeting these challenges.

1.3.3. Network Self-Monitoring

CO-OFDM is heavily dependent on the channel estimation in order to perform equalization. Therefore, various important system parameters can be acquired without the need for monitoring devices. Parameters such as CD, PMD, laser phase noise, OSNR, nonlinearity, and Q-factor can be extracted from CO-OFDM receivers [29,30]. These are important parameters that can be exploited for network monitoring and maintenance.

1.3.4. Sub-Wavelength Bandwidth Access

Commercial optical transmission systems are gearing up for deployment of 400 Gb/s and even 1 Tb/s products within the next couple of years. 1 Tb/s products can be used for support not only between major nodes but also for a smaller intermediate node to economically

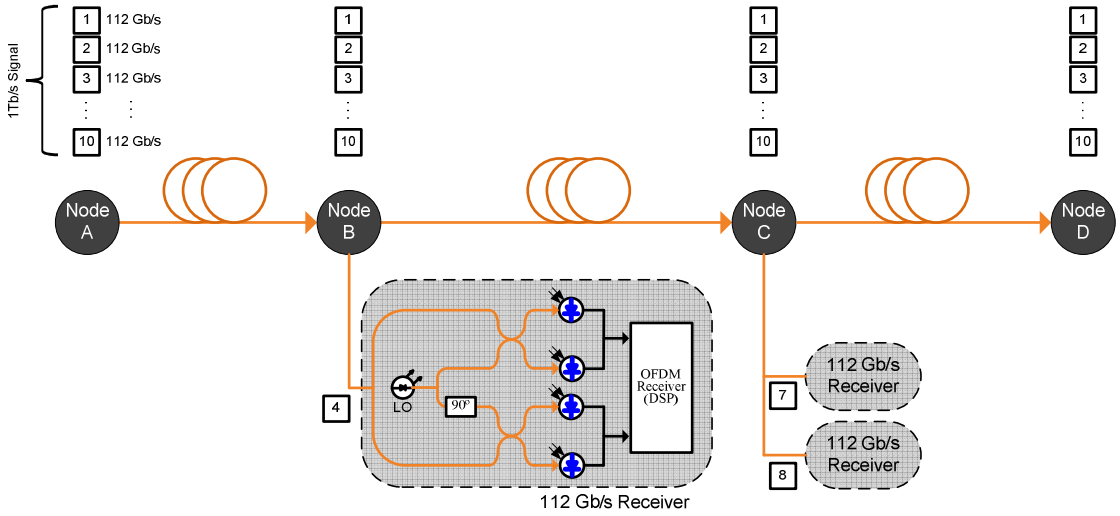

Figure 1-4: Illustration of sub-wavelength bandwidth access for a 1 Tb/s CO-OFDM signal, assuming receivers with 112 Gb/s receiver cards.

access the 1 Tb/s traffic at a lower rate. This is important in next generation, scalable, configurable networks, as some of the intermediate nodes may not need the entire 1 Tb/s bandwidth yet require access to portions of the traffic at 1 Tb/s. Band-multiplexed CO-OFDM provides a unique pathway to 1 Tb/s Ethernet from the current generation of 100 Gb/s solutions [26]. Figure 1.4 depicts an example of the 1 Tb/s link between two major nodes, labeled as nodes A and D, where the band-multiplexed CO-OFDM signal consists of 10 of 112 Gb/s sub-bands. In the intermediate nodes, nodes B and C, only portions of the traffic are accessed; for instance, node B has the right of use in fourth band. This can be done by simply tuning the receiver laser to the centre of the forth band and applying a low-pass RF filter to the down-converted RF signal. In such a configuration, since the entire receiver signal processing is performed at 100 Gb/s, the cost for the intermediate node is cheaper than that of the major node and a future bandwidth expansion of the intermediate node can be realized by adding more 100 Gb/s circuit cards as we see for node C that two sub-bands are accessed.

1.3.5. Adaptive Data Rate

Due to the immense diversity in user demands, constantly varying hourly traffic distributions, and network management constraints, it is preferable that the data rates of different links in the optical network be flexible. CO-OFDM supports digital signal processing at the transmitter and receiver. The optimum data rate can be attained via manipulation of the bit and power loading or the subcarrier level.

Bit loading is done by optimally allocating different modulation schemes across all of the subcarriers [31]. In particular, the signal-to-noise ratio (SNR) of each subcarrier can be monitored through receiver signal processing, and the subcarriers with high SNR values will be loaded with a higher number of bits per subcarrier, consequently maximizing the overall data rate. In power loading, different frequency tones are loaded with a different power [32]. In using this method, the system performance, such as bit-error-ratio (BER), can be improved.

This capability of CO-OFDM transceivers to support a variable data rate through bit loading is the most attractive and important feature for reconfigurable optical networks when compared to DSP-assisted single-carrier solutions. The benefits are four-fold: (i) it allows for one receiver capable of supporting multiple data rates [10,33], preferably through software as mentioned in subsection 1.2.3; (ii) the data rate of each established connection can be dynamically adjusted according to the quality of the channel; (iii) the electrical and optical bandwidth for the signal can be kept constant. This is desirable as no hardware adjustment is required, namely, neither adjustment of the optical filter bandwidth nor the electrical filter bandwidth is needed; (iv) the power of each wavelength channel can be kept constant even though the data rate is varied. Without this feature, the individual wavelength powers would have to be modified in line with dynamic data rate adjustments. This process would affect the gain and tilt of the other channels in a WDM system that share the same optical amplifiers and co-propagate in the same fibre link.

1.3.6. Challenges in CO-OFDM Transmission Systems

As with its RF counterpart, optical OFDM suffers from well-known problems including a high peak-to-average power ratio (PAPR), and sensitivity to phase/frequency noise [10]. In addition, the optical channel has its own unique set of issues. One of the prominent drawbacks is the existence of optical fibre nonlinearity and its effect on the OFDM signal with a high PAPR while interacting with the CD and PMD. Moreover, the tolerable overhead in optical transmission systems is considerably less than for the typical wireless standards, adding one more limitation to design and implementation strategies. There has been extensive research and effort in the optical community on PAPR reduction and the mitigation of fibre nonlinearities in CO-OFDM systems.

1.4. Motivation and Original Contributions

In this section, we explain the motivation and original contributions of the work accomplished in this thesis. There are two main original contributions. The first contribution is in regards to a novel channel estimation and equalization scheme that can reduce the required overhead in CO-OFDM systems, as will be discussed in subsection 1.4.1. In subsection 1.4.2, we explain the second original contribution, which deals with the mitigation of the effect of laser phase noise induced inter-carrier interference (ICI) in CO-OFDM systems.

1.4.1. Overhead Reduction in CO-OFDM Transport Systems

Excessive overhead is considered one of the major drawbacks in CO-OFDM transmission systems compared to its single-carrier counterpart. Overhead can be translated into either an OSNR penalty or a reduction in bandwidth efficiency [14,34]. In CO-OFDM systems, aside from the forward-error-correction (FEC) coding algorithm, the insertion of cyclic prefix (CP), pilot symbols (PSs) and pilot subcarriers (PSCs) results in overhead.

CP are employed to prevent inter-symbol-interference (ISI) in the presence of dispersion and hence, to preserve the orthogonality of the signal. The CP overhead values vary depending on the amount of accumulated CD and the signal baud rate. In typical conventional

CO-OFDM transmission systems, CP overheads of 5% to 10% have often been reported [10,11,34].

To combat dynamic changes in channel characteristics, i.e. CD and PMD, and to provide synchronization, PSs are periodically inserted into the OFDM data symbol sequence. PSs must be sent at a speed that is much faster than the speed of significant physical changes in the channel [11,14]. PS overheads of 2% to 5% have frequently been reported for CO-OFDM transmission systems [10,11,34].

The performance of CO-OFDM transmission links suffers from the laser phase noise, which requires tracking on a symbol-by-symbol basis. By using the PSCs that are inserted in every symbol, such a fast time variation in the optical channel can be compensated for. An overhead of 2% to 5% is expected due to the PSC insertion [10,11,34].

Considering the aforementioned discussion, it is clear that the cumulative overhead can strain the spectral and power efficiency of the transport system. In addition, by implementing higher baud rates and longer transmission reaches, such overhead, or equivalently OSNR penalty, would constrain the design margins of the network.

In chapter 4, we propose and both numerically and experimentally investigate the performance of an adaptive decision-directed channel equalizer (ADDCE) in reduced-guard-interval dual-polarization coherent-optical orthogonal-frequency-division-multiplexing (RGI-DP-CO-OFDM) transport systems. The ADDCE retrieves an estimation of the phase noise value after an initial decision making stage by extracting and averaging the phase drift of all OFDM sub-channels. Moreover, it updates the channel transfer matrix on a symbol-by-symbol basis. In our study, we compare the performance of the ADDCE and the conventional equalizer (CE) combined with maximum-likelihood (ML) phase noise compensation and intra-symbol frequency-domain averaging (ISFA) algorithms. The study is conducted at 28 GBaud for RGI-DP-CO-OFDM systems with quadrature-phase-shift-keying (QPSK) and 16 quadrature amplitude modulation (16-QAM) formats. Using the ADDCE, we accomplish laser phase noise compensation with zero-overhead, and the overhead due to the insertion of pilot symbols (PSs) is significantly reduced. In addition, the ADDCE offers superior performance over the CE in the presence of synchronization timing

error and residual chromatic dispersion (CD). We also achieve a longer transmission distance than when using the CE. At a forward-error-correction (FEC) threshold of 3.8×10^{-3}, using a cumulative overhead of less than 2.6%, transmission distances of 5500 km and 400 km were achieved for the cases of QPSK and 16-QAM RGI-DP-CO-OFDM, respectively [35]. We also provide a brief analysis of the computational complexity of this scheme in terms of the number of required complex multiplications.

1.4.2. Mitigating the Effect of ICI due to Laser Phase Noise

OFDM transmits high-speed serial information through multiple lower-speed subchannels. This reduction in baud-rate leads to a reduction in ISI and therefore a simplification of the equalization process at the receiver. However, the performance of coherent transmission systems are known to suffer from laser phase noise and in the CO-OFDM scenario the degradation is more pronounced as compared to single-carrier schemes due to the relatively longer symbol duration [36]. This ultimately limits the transmission reach and consequently forces engineers to use low linewidth laser sources.

In CO-OFDM, laser phase noise degrades the received signal quality in two ways— the common-phase-error (CPE), which is an identical phase rotation for all subcarriers, and the inter-carrier interference (ICI), which is due to the loss of orthogonality between subcarriers. Common laser phase noise compensation schemes may use RF-pilot enabled [37], pilot subcarriers (PSC) enabled [11], decision-directed, and maximum likelihood (ML) algorithms [38]. In all of these methods, except for the RF-pilot enabled algorithm, only the CPE is mitigated. However, for relatively larger laser linewidths and/or longer symbol durations, the degradation due to ICI becomes pronounced and needs to be compensated for as well. In wireless, the effect of ICI on the performance of OFDM systems due to the local oscillator (LO) phase noise has been extensively investigated and several iterative algorithms have been proposed to jointly estimate the data and the phase noise vector [39]. However, since ICI mitigation requires de-convolving the phase noise spectral components from unknown data subcarriers, such iterative schemes suffer from large latency and high

implementation complexity, which makes them unsuitable for long-haul ultra high-speed optical transmission applications.

In chapter 5, we propose and then investigate, both numerically and experimentally, the performance of a low-complexity non-iterative phase noise induced inter-carrier interference (ICI) compensation algorithm in RGI-DP-CO-OFDM transport systems. This interpolation-based ICI compensator estimates the time-domain phase noise samples using linear interpolation between the CPE estimates of consecutive OFDM symbols. We experimentally study the performance of this scheme for a 28 Gbaud QPSK RGI-DP-CO-OFDM employing a low cost distributed feedback (DFB) laser [40]. Experimental results using a DFB laser with linewidth of 2.6 MHz demonstrate 24% and 13% improvement in transmission reach with respect to the conventional equalizer (CE) in the presence of weak and strong dispersion-enhanced-phase-noise (DEPN), respectively. A brief analysis of the computational complexity of this scheme in terms of the number of required complex multiplications is provided. This practical approach does not suffer from error propagation and enjoys low computational complexity.

1.5. Thesis Outline

Chapter 1 was dedicated to the introduction and to briefly describing the motivation of the work presented in this thesis. The remainder of this thesis is laid out as follows.

Chapter 2: Fundamentals of CO-OFDM

In this chapter, we analytically discuss the concept of the OFDM signal and its efficient modulation and demodulation based on the fast Fourier transform (FFT). In addition, the major signal processing algorithms required for realizing an OFDM system are explained. Then, we elaborate on the architecture of coherent optical OFDM (CO-OFDM) systems, including common transmitter and receiver configurations.

Chapter 3: Implementation of Coherent Transmission System

In the third chapter, we discuss the implementation of the experimental setup, including the arbitrary waveform generator (AWG), the coherent transmitter, and the coherent receiver.

Moreover, the structure of the optical recirculating loop, to mimic the optical transmission link, is described.

Chapter 4: Adaptive Decision Directed Channel Equalization for CO-OFDM

This chapter elaborates on the principles of adaptive decision-directed channel equalization (ADDCE) for CO-OFDM transmission systems. We analytically explain the proposed channel estimation scheme and then study its performance in reducing PSC and PS overhead both numerically and experimentally. In addition, the performance in the presence of the synchronization timing error and the residual dispersion is investigated. A brief analysis of the computational complexity of this scheme in terms of the number of required complex multiplications is also provided.

Chapter 5: Mitigation of ICI due to the Laser Phase Noise

In the fifth chapter, we introduce and both numerically and experimentally investigate the performance of the interpolation-based ICI compensator. The computational complexity of the proposed scheme in terms of the number of required complex multiplications is also studied.

Chapter 6: Conclusion

This chapter summarizes the key developments explained in this thesis. In addition, future steps as directions for future research topics are discussed.

Chapter 2

Fundamentals of CO-OFDM

2.1. Overview

Orthogonal frequency division multiplexing (OFDM) is a form of frequency division multiplexing (FDM) used as a digital multi-carrier modulation technique in which a large number of orthogonal subcarriers are used to transmit the data. The serial data are divided into several parallel streams; one for every subcarrier. Each subcarrier is then independently modulated using a conventional modulation format at a relatively low symbol rate. During this modulation, it is necessary to maintain the total data rate at rates that are equivalent to the conventional single-carrier modulation scheme with a similar electrical bandwidth.

OFDM was originally developed for wideband digital communications, and to be used in applications such as digital television, audio broadcasting, and wireless networks [41]. The major advantage of OFDM over the single-carrier scheme is in its ability to deal with severe channel impairments, such as fading, without the need to employ complex equalization filters [41-43]. The OFDM signal can be perceived as several low baud-rate narrowband signals rather than one high baud-rate wideband signal, thus, it allows for the use of simplified channel equalization techniques. In addition, the low symbol rate makes the use of cyclic prefix (CP) between consecutive symbols affordable, enabling the OFDM signal to handle time-spreading, and its resulting inter-symbol-interference (ISI), in dispersive channels.

The history of orthogonal multi-carrier transmission can be traced back to 1966, when Chang proposed a synthesis of band-limited signals to tackle the problem of multipath fading for multi-carrier transmission [44]. He explained the concept of transmission over a band-limited channel without interference between neighbouring subcarriers in the frequency-domain and consecutive data symbols in the time-domain [44,45]. More recently, Weinstein and Ebert suggested the use of Fourier transforms at both the transmitter and the receiver to substitute for a bank of subcarrier oscillators [46], a significant step towards efficient modulation and demodulation. In the 1980s, OFDM started to be considered as a feasible technology in wireless communications. Cimini, in Bell Labs, published an experimental study on the performance of OFDM modems as the first proof-of-concept OFDM system [47]. In the mid-1990s, OFDM was proven to have better performance than conventional single-carrier systems in several field experiments, and, since 1999, OFDM has been accepted by the IEEE committee for several wireless standards, such as 802.11 and 802.16 [7].

Although OFDM has been intensively studied for a few decades in the RF and wireless domain, the research on OFDM in optical communication systems only commenced in the late 1990s [48]. However, it is only since the late 2000s that optical OFDM for long-haul transmission has been investigated. At the time, two main implementation scenarios came to the forefront: (i) direct-detection optical OFDM (DDO-OFDM), which is based on a

simple and low-cost implementation [49], and (ii) coherent optical OFDM (CO-OFDM), which aims to achieve higher spectral efficiency and receiver sensitivity [50]. In 2007, the world's first coherent optical OFDM experiment with a line rate of 8 Gb/s over 1000km of standard single-mode-fibre (SMF) was reported [51], and since then, the interest in optical OFDM has increased dramatically. In 2009, up to 1 Tb/s optical OFDM was successfully demonstrated in an experimental setup [52].

In this chapter, we review the principles of an OFDM signal and the required signal processing algorithms for cyclic prefix (CP) insertion, synchronization, frequency offset compensation, and channel estimation. Three commonly-reported channel estimation algorithms are explained: least square (LS), maximum likelihood (ML), and intra-symbol frequency-domain averaging (ISFA). Then, the concept of CO-OFDM systems, including different architectures for the transmitter and receiver, is discussed. In addition, multiple-input-multiple-output CO-OFDM (MIMO-CO-OFDM) systems and the required channel estimation procedure are explained. Finally, we briefly introduce different approaches in CO-OFDM implementation with regard to the excessive cyclic prefix overhead.

2.2. Basics of OFDM

In conventional single-carrier systems, the transmitted data is modulated into the frequency, phase, and/or amplitude of only one carrier. As the data rate increases, the duration of each bit gets smaller causing the system to become more susceptible to noise, signal reflections, and other impairments, impeding effective signal recovery [42]. In addition, as the bandwidth used by a single-carrier system increases, the possibility of interference from signals in neighbouring channels becomes greater. This type of interference is known as the frequency interference or cross-talk.

Frequency-division-multiplexing (FDM) extends the concept of single-carrier systems by using multiple subcarriers within the same channel. As shown in figure 2.1, the serial data stream is divided into multiple parallel sub-channels being carried by multiple subcarriers. Since different subcarriers share the same transmission media, an FDM system has to

use extra frequency guard spacing between subcarriers to minimize the effect of inter-carrier-interference (ICI) [41,42].

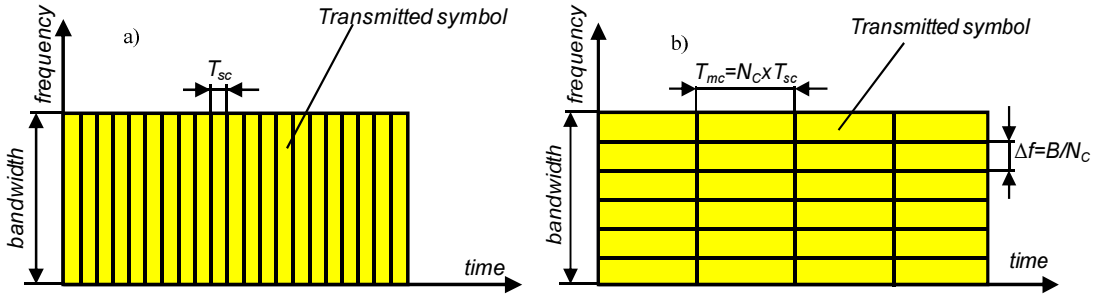

Figure 2-1: The serial data stream in single-carrier transmission (a) and the parallel data stream in multi-carrier transmission (b). T_{sc} and B are the symbol duration and the bandwidth of the single-carrier signal, respectively. T_{mc} and N_c are the symbol duration and the number of subcarriers of the multi-carrier signal, respectively.

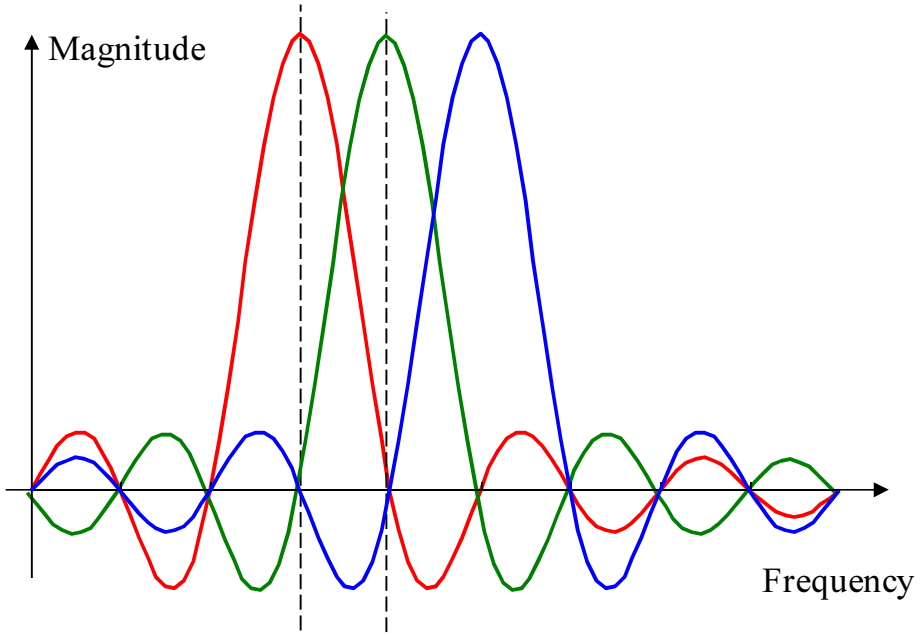

Figure 2-2: The concept of orthogonal overlapped adjacent subcarriers for OFDM signal. The power of the adjacent subcarriers is zero at the frequency of each subcarrier.

OFDM is a special form of FDM in which the subcarrier guard spacing can be omitted because the subcarriers are orthogonal to each other. The principle of orthogonal multiplexing, from Chang [44], allows for a significant improvement in the bandwidth efficiency of

OFDM implementation in comparison to ordinary FDM, as the neighbouring subcarriers are overlapped with each other. In this configuration, the power of an adjacent subcarrier is zero at the central frequency of each specific subcarrier, as illustrated in figure 2.2. Moreover, for OFDM systems, instead of applying a bank of analog oscillators for each subcarrier at discrete frequencies, OFDM signals can be conveniently implemented with the aid of a fast Fourier transform (FFT). This will be further discussed in subsection 2.2.1.

2.2.1. Mathematical Formulation of an OFDM Signal

OFDM is a special form of multi-carrier transmission; a generic illustration of its modulation and demodulation is depicted in figure 2.3. The multi-carrier transmitted signal in the time-domain, $A(t)$, can be represented as

$$A(t) = \sum_{i=-\infty}^{+\infty} \sum_{k=1}^{N_{SC}} c_{i,k} a_k (t - iT_s) \tag{2.1},$$

in which

$$a_k(t) = \prod(t) \exp(2j\pi f_k t) \tag{2.2},$$

$$\prod(t) = \begin{cases} 1 & 0 < t \le T_s \\ 0 & t \le 0, t > T_s \end{cases} \tag{2.3},$$

and where $c_{i,k}$ is the data of the i^{th} symbol (time index) at the k^{th} subcarrier (frequency index), a_k is the waveform for the k^{th} subcarrier, N_{sc} is the number of subcarriers, f_k is the centre frequency of the k^{th} subcarrier, and T_{s} is the symbol duration. The optimum detector for each subcarrier could use a filter that matches the subcarrier waveform. Consequently, the detected subcarrier-specific data symbol via matched filter, $c'_{i,k}$, can be expressed as

$$c'_{i,k} = \int_0^{T_s} B(t - iT_s) \times a_k^* \; dt = \int_0^{T_s} B(t - iT_s) \times \exp(-j2\pi f_k t) \; dt \tag{2.4},$$

where $B(t)$ is the received signal in the time-domain.

A conventional FDM signal employs non-overlapped, band-limited signals and can be realized using a bank of oscillators and filters at both the transmitter and the receiver. How-

ever, such a configuration requires excessive bandwidth due to frequency guard spacing [42]. In addition, it is not cost effective because of the need for multiple oscillators. OFDM provides an alternative methodology using overlapped and orthogonal signals that addresses these known issues of FDM. The concept of orthogonality originates from the straightforward correlation between any two subcarriers, which can be mathematically described as

$$\begin{aligned}\delta_{kv} &= \frac{1}{T_s}\int_0^{T_s} a_k a_v^* \; dt = \frac{1}{T_s}\int_0^{T_s} \exp\left(j2\pi\left(f_k - f_v\right)t\right) \; dt \\ &= \exp\left(j\pi\left(f_k - f_v\right)T_s\right)\frac{\sin\left(\pi\left(f_k - f_v\right)T_s\right)}{\pi\left(f_k - f_v\right)T_s}\end{aligned} \tag{2.5}.$$

One can see that if the following condition,

$$f_k - f_v = \frac{m}{T_s} \tag{2.6},$$

in which m represents an integer number, is fulfilled, then the two subcarriers are orthogonal to each other. This suggests that if their frequencies are spaced at an integer multiple that is inverse of the symbol rate, the orthogonal subcarrier sets can be recovered, with the matched filters of equation 2.4, without suffering from ICI, despite signal spectral overlapping [41,42]. In practice, this integer is set to 1, m=1, to attain the highest possible spectral efficiency.

We temporarily omit the time index, i, to focus our attention on one OFDM symbol. Assume that we sample $A(t)$ at every interval of T_s/N_{SC}. The l^{th} sample of $A(t)$ from equation 2.1 can be expressed as

$$A_l(t) = \sum_{k=1}^{N_{sc}} c_k \exp\left(j2\pi f_k \frac{(l-1)T_s}{N_{sc}} \right) \tag{2.7}.$$

Using the orthogonality condition of equation 2.6, we have

$$f_k = \frac{k-1}{T_s} \tag{2.8},$$

and, by substituting equation 2.8 into equation 2.7, we can rewrite equation 2.7 as

$$A_l(t) = \sum_{k=1}^{N_{sc}} c_k \exp\left(j2\pi \frac{(k-1)(l-1)}{N_{sc}} \right) \quad (2.9).$$

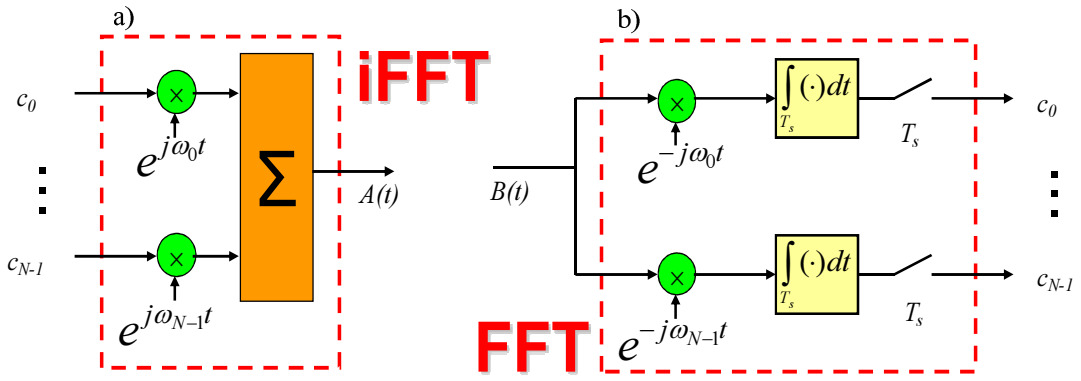

Figure 2-3: A generic form of OFDM signal modulation (a) and demodulation (b) in the context of multi-carrier transmission system. The FFT operation can be employed to efficiently replace the bank of electrical mixers and filters.

This is exactly the expression for the inverse discrete Fourier transform (IDFT). This indicates that the OFDM baseband signal can be implemented by the IDFT while the modulated signals are in the frequency-domain and the output of the IDFT is in the time-domain. Following a similar method for the receiver, the data is recovered by applying the discrete Fourier transform (DFT). The major advantage of using DFT/IDFT algorithms for OFDM modulation and demodulation is the fact that it can replace the block of RF oscillators, mixers, and filters at the receiver and transmitter, reducing the implementation complexity and cost. In addition, a large number of orthogonal subcarriers can be modulated and demodulated without being limited to the count, cost, and complexity of the RF components [7]. This leads to a relatively simple architecture for OFDM implementation when large numbers of subcarriers are required.

In practice, the DFT and IDFT are realized with the fast Fourier transform (FFT) algorithm and its inverse, the IFFT [12,46]. Both the FFT and IFFT exhibit an effective realization for the computation of complex values in digital domain when the numbers of sampling points in the time-domain, as well as the number of grid points in the frequency-

domain, are a power of 2. The number of complex multiplications required to perform an IFFT or FFT of size N is $N/2\log_2 N$ [12].

It is worth mentioning that there are two critical devices that must be included for implementation of the FFT/IFFT in the modulation and demodulation processes. A digital-to-analog converter (DAC) is needed to convert the discrete digital values to the continuous analog signal. In addition, an analog-to-digital converter (ADC) is required to convert the analog received signal to discrete samples.

2.2.2. Peak to Average Power Ratio

High PAPR has often been reported as one of the major drawbacks in OFDM system implementation [53]. In RF systems, the key problem resides with the power amplifiers at the transmitter, where the amplifier gain can get saturated due to high input power. In optical transmission systems, the lumped optical power amplifiers, mostly erbium-doped amplifiers (EDFAs), are ideally linear, due to their slow response time on the order of milliseconds, regardless of their input signal power [4]. Nevertheless, the PAPR still presents a challenge for optical fibre communications due to the optical fibre nonlinearity and the limited dynamic range and resolution of the DAC [54]. The PAPR of the OFDM signal is mathematically expressed as

$$PAPR = \frac{\max\left\langle \left| A(t) \right|^2 \right\rangle}{E\left\langle \left| A(t) \right|^2 \right\rangle}, \quad t \in [0, T_s] \tag{2.10}.$$

The origin of the high PAPR of the OFDM signal can be understood from its multi-carrier nature. The problem results from the nature of the modulation itself, where multiple subcarriers, equivalently sinusoids, are added together to form the OFDM signal. The worst-case scenario happens when, in the time-domain, all N_{SC} subcarriers add constructively and produce a peak power that is N_{SC} times greater than the average power of the signal. As one realizes, the PAPR of an OFDM signal can be excessively high for either RF or optical systems. This maximum PAPR increases whenever the number of subcarriers

increases. Without knowledge of the data pattern, the peaks occur with random amplitudes and at random times.

PAPR reduction has been an intensely pursued subject [7]. The PAPR reduction algorithms allow for trade-offs among PAPR, bandwidth efficiency, and computational complexity. The following are the most popular PAPR reduction categories.

PAPR reduction with signal distortion: This is performed by hard clipping the OFDM signal. The consequence of clipping is a penalty in signal quality, i.e. increased bit-error-ratio (BER) and out-of-band distortion. The out-of-band distortion can be mitigated through filtering [54-56].

PAPR reduction without signal distortion: The idea behind this approach is to map the original waveform to a new set of waveforms that have a PAPR lower than the desirable threshold. Distortion-less PAPR reduction algorithms include selection mapping, optimization approaches, such as partial transmit sequence, and modified signal constellation or active constellation extension [54,57,58].

2.2.3. Cyclic Prefix

State-of-the-art transmission systems suffer from inter-symbol-interference (ISI) due to the effects of dispersive channels, leading to interference between adjacent OFDM symbols in the time-domain. Furthermore, as a result of the ISI, the inter-carrier-interference (ICI) degrades the performance of the OFDM signal. In this respect, one of the enabling techniques for OFDM is the insertion of cyclic prefix and postfix as a type of time-domain guard spacing [59].

Assume three consecutive OFDM symbols experience a dispersive channel as depicted in figure 2.4. Each OFDM symbol consists of several subcarriers. At the transmitter, all subcarriers are aligned. However, at the receiver, the slow subcarriers are delayed with respect to the fast ones. We select a DFT window containing a complete OFDM symbol for the middle subcarrier. One can see that due to the channel dispersion, the slower and faster subcarriers have crossed the window boundaries. This leads to interference between neighbouring OFDM symbols. This is the so-called ISI phenomenon. Moreover, since the

OFDM waveform in the DFT window for both slow and fast subcarriers is incomplete, the critical orthogonality condition for the OFDM subcarriers is lost, resulting in an inter-carrier-interference (ICI).

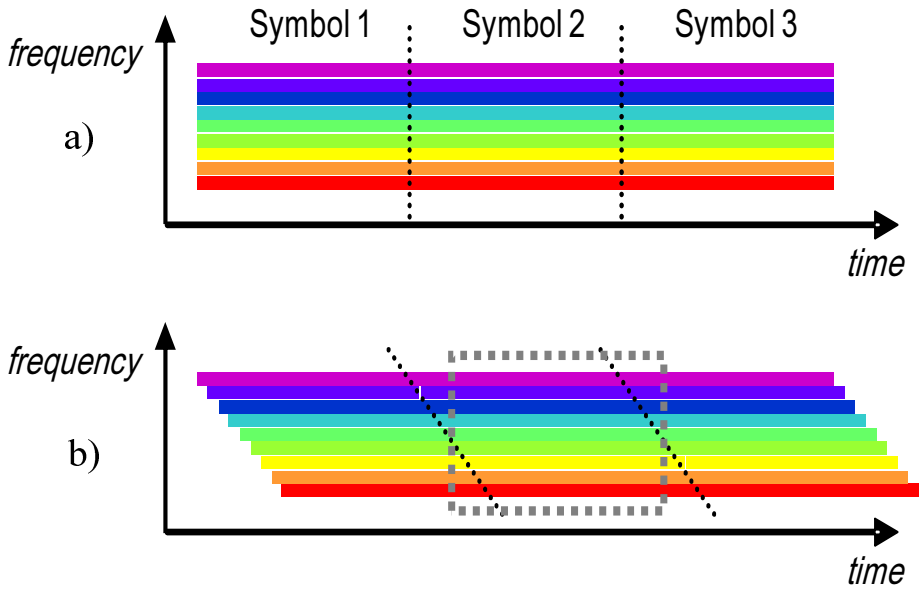

Figure 2-4: Consecutive OFDM symbols before (a) and after (b) propagation through a dispersive medium.

Cyclic prefix and postfix were proposed to prevent ISI and ICI induced by the channel dispersion. Figure 2.5 shows the insertion of the cyclic prefix and postfix, by extension of the OFDM waveform, as a form of guard interval. As seen in figure 2.5, the waveform in the guard interval is essentially an identical copy of that in the DFT window, with the only difference being a shifted time reference. Figure 2.5 (c) shows the OFDM signal with the guard interval at the receiver. We assume that the signal has experienced the same dispersive channel. The same DFT window is selected containing a complete OFDM symbol for the fast subcarrier waveform. As we can see, a complete OFDM symbol for the slow subcarriers is also maintained in the DFT window because a proportion of the cyclic prefix and/or postfix has moved into the DFT window, restoring the identical part that has shifted out. Hence, the OFDM symbol for slow subcarriers is an identical copy of the transmitted waveform with an additional phase shift. This phase shift can be compensated for through

the use of channel estimation, and will be subsequently removed before the decision making stage.

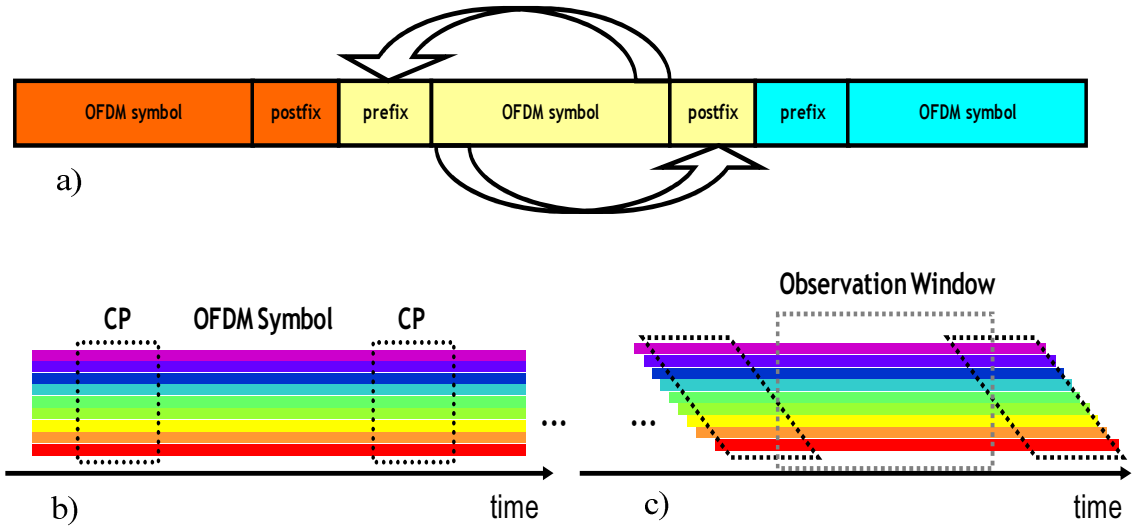

Figure 2-5: Insertion of cyclic prefix and postfix (a) and consecutive OFDM symbols guarded with CP before (b) and after (c) propagation through a dispersive medium.

It has been shown that insertion of either of cyclic prefix or postfix would guarantee ISI-free OFDM transmission as long as the duration of the cyclic prefix or postfix is longer than the delay spread of the channel, as

$$t_d < \Delta_G \tag{2.11},$$

where Δ_G and t_d are the length of the guard interval, i.e. CP, and the length of the channel delay spread, respectively [41,42].

In optical fibre communications, chromatic dispersion (CD) generates ISI due to a time shift of subcarriers. To avoid signal distortion, the cyclic extension has to be chosen sufficiently large such that it corresponds to the maximum length of the expected delay spread [7]. In practice, a limited length sequence from the beginning of the OFDM symbol is copied to its end, or equivalently from the end to the beginning for the case of the postfix, leading to an extension of the overall OFDM symbol period. This extension is inserted at the transmitter after the IFFT, and is removed at the receiver before the FFT operation. In addi-

tion, the symbol itself can be assumed as a cyclic symbol, in turn simplifying the mathematical algorithms in the receiver [42].

At the receiver, both the data processing and the decision are performed based on the inner observation period where no ISI is present. However, two other critical procedures must be carried out to recover the OFDM data symbol properly: (i) the selection of an appropriate DFT window, called the DFT window synchronization, and (ii) the estimation of the phase shift for each subcarrier, called the channel estimation or subcarrier recovery. We discuss these two procedures in the next subsections.

2.2.4. Channel Synchronization

Synchronization is one of the most critical tasks in every receiver. As we have seen in subsection 2.2.3, each OFDM symbol in the time-domain is comprised of a guard interval and an observation period. An improper DFT window will result in ISI and ICI; hence, it is imperative that the start of the DFT window should be determined precisely [60].

A popular method of window synchronization was proposed by Schmidl and Cox [61]. In this method, a reference symbol or preamble consisting of two identical segments is transmitted. These two identical segments can be mathematically expressed as

$$A_l = A_{l-N/2} \qquad l \in \left[N/2+1, N\right] \tag{2.12},$$

where A_l is the l^{th} digital signal in the time-domain with a random value, when $l \in \left[1, N/2\right]$ and N is the number of samples of one OFDM symbol. We denote this reference symbol as [X X] to indicate the two identical sections. Such a symbol can be generated by setting the amplitude of every second subcarrier to zero. At the receiver, the delineation can be studied by investigating the following time-domain correlation function,

$$R_d = \sum_{l=1}^{N/2} B_{l+d}^{*} B_{l+d+N/2} \tag{2.13}.$$

where B_l is the l^{th} received digital signal in the time-domain. The idea is that, in the reference symbol, the second half of B_l is identical to the first half except for a phase shift, and,

assuming that the frequency offset is small to start with, we anticipate that when d=0, the correlation function, R_d, reaches its maximum value. In practice, when R_d reaches the maximum value, one observes a peak. Upon finding the exact position of the reference symbol by using this peak, the position of subsequent data symbols can be determined.

The Schmidl and Cox method has a major problem in that the correlation function of R_d, instead of a sharp peak, exhibits a plateau that causes timing uncertainty. To solve this problem, different OFDM frame synchronization algorithms in the wireless domain are tested with optical channels in the hope of finding a suitable alternative for real-time CO-OFDM implementation. This algorithm should be (i) able to provide a sharp and clear timing metric, and (ii) resilient to chromatic dispersion and carrier frequency offset. Minn proposed a method that most fits these requirements [62]. In this scheme, a time-domain preamble that is partitioned into four equal length segments as [X X X –X] is used, where X is generated by the IFFT from a Pseudo-random noise sequence. The timing metric in this case can be expressed as

$$M_d = \left(\frac{4|P_d|}{3R_d} \right)^2 \tag{2.14},$$

where

$$P_d = \sum_{l=1}^{N/4-1} \left[B^*_{d+l} B^*_{d+l+\frac{N}{4}} + B^*_{d+l+\frac{N}{4}} B_{d+l+\frac{N}{2}} - B^*_{d+l+\frac{N}{2}} B_{d+l+\frac{3N}{4}} \right] \tag{2.15},$$

and

$$R_d = \sum_{m=0}^{3} \sum_{l=1}^{N/4-1} \left| B_{d+l+m\frac{N}{4}} \right|^2 \tag{2.16}.$$

The OFDM frame timing is estimated by finding d which maximizes the timing metric in equation 2.14. The timing metric at the peak will be considered as the start of the DFT window. It is shown in [37] that it can also be exploited as an indication for frequency offset estimation.

2.2.5. Carrier Frequency Offset Compensation

The frequency offset in an OFDM system breaks the orthogonality criterion between the subcarriers, causing degradation in performance due to the effect of ICI [42,60]. In coherent transmission systems, lasers are usually locked to an international telecommunication union (ITU) frequency standard through a wavelength locker, but only at accuracy within a few gigahertz. An excessive frequency offset, f_{off}, can cause two major problems:

Excessive RF bandwidth requirement: The highest RF frequency of the RF signal, after the down-conversion, is increased by the amount of frequency offset, f_{off}. This results in RF bandwidth expansion and, consequently, an increase in the receiver cost.

DC leakage on subcarriers: Those data subcarriers which happen to overlap with the receiver local oscillator (LO) will have degraded performance because of the DC leakage of the down-conversion process. Moreover, in a WDM system, the wavelengths (frequencies) of LOs for various WDM channels will be different if they are not frequency tracked to the laser of the transmitter. Therefore, there are no common subcarriers that can be left unfilled to accommodate the DC leakage problem [37].

In this sense, the purpose of the frequency acquisition is first to coarsely estimate the frequency offset, and then to bring the receiver laser to within several times the subcarrier frequency, typically in the range of -100 MHz to 100 MHz, from that of the transmitter laser. There are several frequency acquisition algorithms that have been proposed in the wireless domain, such as the pilot-tone [63] and the shortened repeated DFT approach [64]. In CO-OFDM systems, since the initial frequency offset could be as large as several gigahertz, the initial acquisition is normally obtained by sending a long-stream continuous wave (CW) signal and subsequently measuring the frequency of the offset tone. The error signal is used to control the local laser to bring its frequency (wavelength) close to that of the transmitter laser.

On the other hand, the center frequencies (wavelengths) of both transmitter and receiver lasers drift constantly and randomly in time at a rate ranging from kilohertz to megahertz. To perform a precise carrier frequency offset tracking and compensation, the Schmidl and Cox approach is often used [61]. In this approach, to estimate the frequency shift of the

OFDM signal at the receiver, the two halves of the reference symbol are transferred separately into the frequency-domain via a DFT operation. By calculating the mean phase shift of the second set of subcarriers with respect to the first set, the frequency offset of the OFDM signal can be derived. Following the same trend as subsection 2.2.4, and by using equation 2.16, we arrive at

$$R_{\hat{d}} = \sum_{l=1}^{N/2} \left| B_{l+\hat{d}} \right|^2 e^{j\left(\pi f_{off}/\Delta f\right)} + w(n) \tag{2.17},$$

where f_{off}, Δf, and $w(n)$ represent the frequency offset, the subcarrier spacing and the noise component, respectively. It follows from equation 2.17 that the offset frequency can be estimated as

$$\hat{f}_{off} = \frac{\Delta f}{\pi} \angle\left(R_{\hat{d}}\right) \tag{2.18},$$

where $\hat{d}$ and $\angle\left(R_{\hat{d}}\right)$ are the estimated DFT window timing and the angle of the complex value of the correlation function, $R_{\hat{d}}$, respectively. The accuracy of this estimation can be improved by sending multiple reference symbols [7].

Next, the mandatory frequency down-conversion is performed in the time-domain by generating and multiplying a carrier by the received OFDM signal, as

$$B_c(t) = B(t)\exp\left(-2j\pi\hat{f}_{off}t\right) \tag{2.19}.$$

The frequency offset compensated signal, $B_c(t)$, can be used to obtain the received data symbol in the frequency-domain, $r_{i,k}$, via the DFT. The subsequent subcarrier recovery for symbol decision is discussed in next subsection.

2.2.6. Channel Estimation Algorithms

Channel estimation has significant importance to the overall system performance; a wide variety of algorithms for channel estimation have been developed [24]. In this section, we discuss the most relevant and widely-reported algorithms in the field of optical fibre transmission. In CO-OFDM, there are two factors that lead to the rotations of the received data

symbol constellation, $r_{i,k}$: (i) the channel dispersion that gives frequency-selective dependence across the OFDM spectrum, and (ii) the phase noise coming from the lasers at the transmitter and the receiver.

The timescale on which changes for the two above-mentioned factors affect the system are different. The dispersion is known to change on a time scale of milliseconds as a result of mechanical movements. In particular, the chromatic dispersion (CD) varies in response to the temperature fluctuation. The polarization-mode dispersion (PMD) varies due to mechanical stress and temperature fluctuations on a time scale of a millisecond [65,66]. However, there are reports on microsecond PMD changes under severe mechanical stress in metropolitans [67]. The laser phase noise, with a linewidth ranging from 100 kHz to several megahertz, causes faster variations in the phase of the channel response, and needs to be tracked on a symbol-by-symbol basis.

2.2.5.1. Least Square (LS) Channel Estimation

In OFDM systems, signal processing is typically performed in blocks containing a large number of OFDM symbols [42]. Within each block, the channel is assumed to be invariant, whereas the phase noise varies on an OFDM symbol basis. Subsequently, the subcarrier recovery consists of two steps: namely, channel and phase estimation. There are various methods of channel estimation, such as the time-domain and the frequency-domain approaches [24,68,69]. We focus on the carrier recovery based on frequency-domain pilot symbols (PSs), also known as training sequence, and pilot subcarriers (PSCs). Figure 2.6 shows the two-dimensional time-frequency structure for one OFDM block that includes N_{sc} subcarriers in frequency-domain. The reference symbol is added at the beginning to allow for the implementation of the DFT window synchronization and the carrier frequency offset compensation, as discussed in subsections 2.2.3 and 2.2.4. In block-type pilot-based channel estimation, OFDM pilot symbols (training sequence) are transmitted periodically, and all subcarriers are used as pilots. Their task is to estimate the channel frequency response with or without using any knowledge of the channel statistics. The receiver uses the estimated channel conditions to decode the received data inside the block until the next PS arrives. The LS estimator minimizes the following parameter

$$(r - ch)^{*}(r - ch) \tag{2.20},$$

where r, c, and h are the frequency-domain representation of the received symbol, transmitted symbol, and the channel transfer factor, respectively. It is shown that the LS estimator of h is given by [42]

$$h_k = c_{1,k}{}^{-1} r_{1,k} = \left[\frac{c_{1,k}}{r_{1,k}} \right]^{T} \qquad (k = 0,1,...,N_{SC} - 1) \tag{2.21},$$

where k is the index for subcarriers. The subscript index number 1 denotes that this is the first symbol of the block, since the PS is usually inserted at the beginning of each data block.

Without using any knowledge of the statistics of the channels, the LS estimators are calculated with relatively low complexity; however, they are known to suffer from a high mean-square error [70]. To increase the accuracy of channel estimation, a time-domain averaging method is commonly used in which multiple PSs are sent to extract the channel transfer function factors [12,34]. The improvement can also be obtained by averaging in the frequency-domain over multiple subcarriers as presented in [65], this technique is known as intra-symbol frequency-domain averaging (ISFA), and will be further discussed in subsection 2.2.5.2.

The phase noise estimation is needed in order to estimate the common-phase-error (CPE). We assume that the N_{PSC} pilot subcarriers (PSCs) are used for phase estimation; thus, the CPE for the i^{th} OFDM symbol can be estimated as

$$CPE_i = \frac{1}{N_{PSC}} \sum_{q=1}^{N_{PSC}} \left(\arg\left(\frac{r_{i,q}}{h_q} \right) \right) \tag{2.22}.$$

After channel and phase estimations, the subcarrier recovery can be completed as

$$\hat{S}_{i,k} = r_{i,k} h_k^{-1} \exp(-jCPE_i) \tag{2.23},$$

where $\hat{S}_{i,k}$ is the subcarrier-specific equalized symbol which is ready for detection.

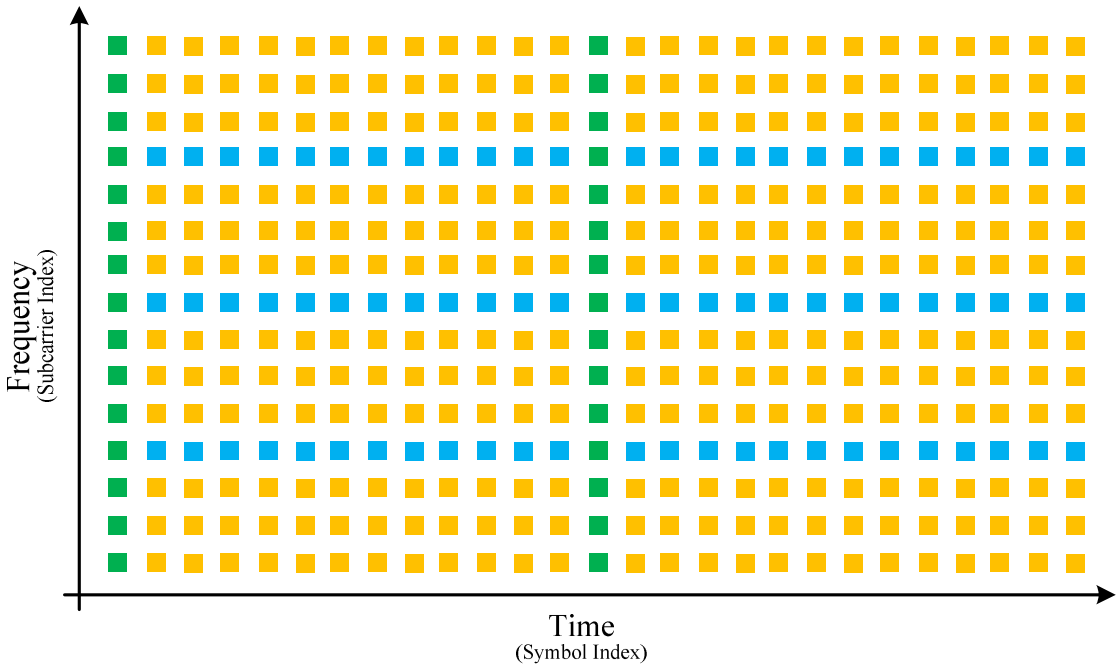

Figure 2-6: The two-dimensional time-frequency structure for channel estimation in OFDM block of data using training symbols and pilot subcarriers. Green, blue and yellow spots depict pilot symbols, pilot subcarriers, and data symbols.

It is worth noting that the DFT sampling timing offset may generate a phase term which is linear with the subcarrier frequency. This effect is caused by the sampling clock rate offset and may require that the DFT sampling be reset approximately every tens of microseconds [7,24]. Therefore, sending reference and pilot symbols (PSs) periodically is compulsory and can help alleviate the aforementioned problem.

2.2.5.2. Intra-Symbol Frequency-Domain Averaging (ISFA)

In OFDM, a large number of subcarriers are usually used so that the frequency-domain transfer function of a given sub-channel for each subcarrier can be considered as constant or flat [42]. As we mentioned earlier, to increase the channel estimation accuracy, a time-domain averaging method that averages the channel matrices, estimated by multiple PSs for each frequency subcarrier, is commonly used.

Recently, an intra-symbol frequency-domain averaging (ISFA) algorithm was proposed [65], where the averaging is performed over the estimated channel transfer factor for multiple adjacent subcarriers in the same PS. To improve the accuracy of channel estimation in the presence of noise, the ISFA process is applied such that for each modulated subcarrier the channel transfer factor is an average of the channel transfer factor estimated for itself and its multiple neighbouring subcarriers. In opposition to the time-domain averaging methods, ISFA is performed in the frequency-domain [65] and is founded on the fact that the channel behaviour is usually highly related to the neighbouring subcarriers.

Typically, for subcarrier k, the averaging can be performed over subcarrier k and its m left and m right neighbours, or in total up to $2m+1$ subcarriers. The improved channel matrix for subcarrier k after the ISFA process can be expressed as

$$h_k^{ISFA} = \frac{1}{\min(k_{\max}, k+m) - \max(k_{\max}, k-m) + 1} \sum_{q=k-m}^{k+m} h_q \quad (2.24),$$

where $k_{\max}$ and $k_{\min}$ are the maximum and minimum modulated subcarrier indexes, respectively. In equation 2.24, the elements of the estimated channel transfer factor for outside the range [$k_{\min}$, $k_{\max}$] are set to zero in the averaging process. Once the improved channel transfer factors for all modulated subcarriers are obtained, they can be inverted and applied to the corresponding received subcarriers in the payload symbols to obtain the transmitted information.

Two subcarrier regions need to be processed specially: (i) the edge subcarriers when the selected window size exceeds the bandwidth, as the window size has to be narrowed to keep only the used subcarriers, and (ii) the subcarriers close to the local oscillator (LO); these are usually highly affected by a strong direct current (DC) leakage caused by the LO. In order to obtain the accurate channel transfer factor in subcarriers close to the affected subcarriers, the affected subcarriers need to be excluded during averaging.

2.2.5.3. Maximum Likelihood (ML) Channel Estimation

For simplicity, we omit the procedure of phase noise estimation and the index of OFDM symbol sequence, *i*. The subcarrier-specific received symbol can be expressed in the concise form of

$$r_k = h_k c_k + w_k \tag{2.25},$$

where w_k represents the noise term. We assume that equation 2.25 represents an additive white Gaussian noise (AWGN) channel, and each subcarrier is independent. The joint probability density function (PDF) of the received signal with a deterministic but unknown function h_k can be expressed as

$$p\left(r_1, r_2, ..., r_{N_{SC}} \middle| h_1, h_2, ..., h_{N_{SC}}\right) \propto \exp\left(\sum_{k=1}^{N_{SC}} \frac{\left(r_k - h_k c_k\right)^* \left(r_k - h_k c_k\right)}{2\sigma^2} \right) \tag{2.26},$$

where σ is the standard deviation of the noise for each subcarrier. The asterisk represents the complex conjugation operator. To derive equation 2.26, we assumed that the standard deviation values have the same magnitude across all subcarriers. The purpose of channel estimation is to find the matrix h_k that maximizes the joint PDF function of $p\left(r_1, r_2, ..., r_{N_{SC}} \middle| h_1, h_2, ..., h_{N_{SC}}\right)$. From equation 2.26, we can equivalently try to find the h_k that minimizes the likelihood function of

$$\Lambda\left(h_1, h_2, ..., h_{N_{SC}}\right) = \sum_{k=1}^{N_{SC}} \left(r_k - h_k c_k\right)^* \left(r_k - h_k c_k\right) \tag{2.27}.$$

Since h_k is a complex variable, we treat h_k and its conjugate, h_k^*, as independent variables and differentiate equation 2.27 with respect to h_k^*, such that

$$\frac{\partial \Lambda\left(h_1, h_2, ..., h_{N_{SC}}\right)}{\partial h_k} = \left(r_k - h_k c_k\right) c_k^* \tag{2.28}.$$

By setting equation 2.28 equal to zero, we arrive at h_k^{ML}, the ML channel transfer factor of h_k, and we have

$$h_k^{ML} = \frac{r_k}{c_k} = h_k + \frac{w_k}{c_k} \quad (2.29),$$

where h_k^{ML} is the ML estimation for the k^{th} subcarrier. h_k^{ML} can be used for updating the channel transfer factor or to estimate the phase noise. The ML estimation can be implemented with or without using PSs and PSCs. In addition, it can be easily combined with other algorithms such as LS or ISFA [38,69].

2.3. The Architecture of CO-OFDM Systems

There is a mutually advantageous relation between coherent optical communications and OFDM. OFDM brings coherent systems computational efficiency and the ease of channel and phase estimation [7], whereas coherent systems bring OFDM linearity in electrical to optical (E/O) up-conversion and optical to electrical (O/E) down-conversion [8,71]. Consequently, a linear transformation is the key goal for OFDM implementation. In previous sections, we explained the required signal processing engine for the electrical OFDM transmitter and receiver. Figure 2.7 shows a diagram of the electrical OFDM transmitter and receiver. In this section, we first describe the structure of the optical transmitter and receiver in a CO-OFDM system. Next, the concept of multiple-input-multiple-output (MIMO) fibre-optic transmission is explained. Lastly, different implementations of a CO-OFDM system with respect to cyclic prefix (CP) overhead management are briefly reviewed.

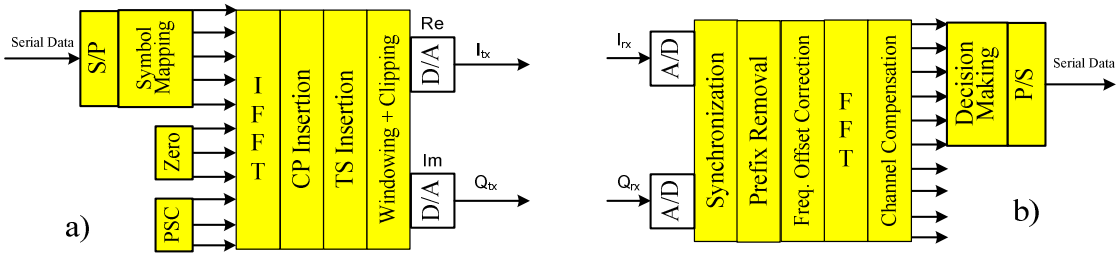

Figure 2-7: Stages of an electrical OFDM signal transmitter (a) and receiver (b).

2.3.1. Transmitter and Receiver Design

The primary design goal for CO-OFDM is to construct a linear transformation system. In general, an electrical OFDM signal is a complex valued signal. To convert a complex valued baseband signal into the optical domain, the signal can be electrically up-converted using an electrical intermediate frequency (IF) carrier to modulate the signal upon applying a complex electrical in-phase/quadrature (I/Q) mixer [12,24]. The resulting up-converted electrical OFDM signal can be electro-optically converted using a state-of-the-art amplitude modulator i.e. a Mach-Zehnder modulator (MZM). Alternatively, a complex electro-optic I/Q modulator can be driven directly by the complex electrical OFDM baseband signal to convert it into the optical domain [12,24]. The transmitter setups are summarized in figure 2.8.

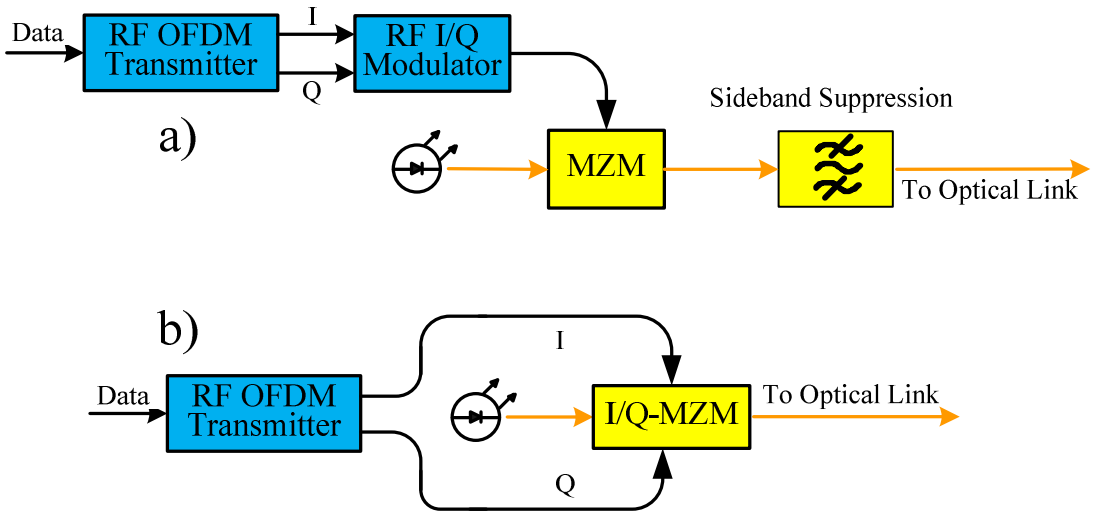

Figure 2-8: The transmitter setup in CO-OFDM systems based on electrical IF up-conversion (a) and direct E/O up-conversion

The characteristics of MZM have been studied by Auracher [72]. It is shown that for conventional direct detection systems, the optimal bias point is at the quadrature, and a signal with relatively large swing experiences nonlinearity due to the MZM nonlinear transfer function. Although, the quadrature bias point has been broadly adopted for both analog and digital direct detection systems, the null bias point for CO-OFDM up-conversion signifies a

fundamental distinction between optical intensity modulation and optical field modulation. In conventional direct detection systems, the transformation between the electrical drive voltage and the optical power is important since the transfer function is the optical intensity versus the drive voltage. However, in coherent detection systems, it is the transformation between the electrical drive voltage and the optical field that is of concern, as the transfer function is the I and Q components of the optical field versus the drive voltage. It is worth mentioning that this optimal modulator null bias point for the E/O up-conversion is independent of the modulated waveform and it can be any arbitrary waveform, not necessarily limited to that of CO-OFDM.

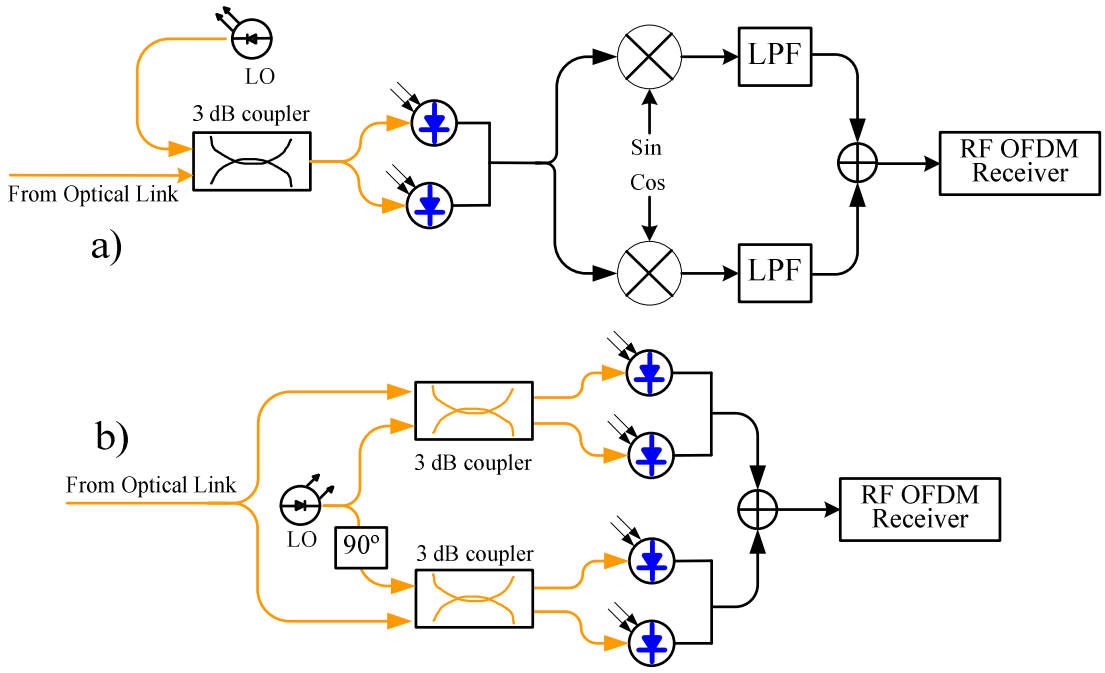

Figure 2-9: Coherent optical receiver based on heterodyne (a) and intradyne (b) approaches.

At optical receivers, simple photodiodes are typically employed which operate based on the square law detection scheme. However, it is impossible to transfer the optical OFDM signal directly into the electrical domain, and an optical carrier needs to be provided either by the transmitter, direct detection scheme, by an LO at the receiver, coherent optical scheme, or via a heterodyne or intradyne approach (shown in figure 2.9 (a) and figure 2.9 (b), respectively) [12,24]. In a heterodyne scenario, the optical OFDM signal is converted

into a real valued electrical OFDM signal at an intermediate frequency (IF). By using a subsequent electrical I/Q demodulator, the real and imaginary components are recovered in the baseband. In an intradyne approach, the OFDM signal beats with the LO signal in an optical 90° hybrid to directly down-convert the optical signal to the baseband to obtain the I and Q components of the signal.

CO-OFDM systems are mainly based on direct E/O up-conversion transmitters (figure 2.8 (b)), and direct O/E down-conversion receivers (figure 2.9 (b)). They are usually known as the intradyne systems [12]. In this architecture, the electrical OFDM signal is generated and distributed in the baseband, both in the transmitter and in the receiver, leading to the lowest electrical bandwidth requirements. The mixing of the optical OFDM signal with the LO signal results in the desired electrical OFDM signal if both signals, received signal and LO, are aligned in polarization.

2.3.2. Multiple Input Multiple Output Systems

In the wireless systems literature, the term MIMO is used to describe a family of systems with multiple transmit antennas and/or multiple receive antennas. MIMO can be used to either increase the overall capacity of the system or to reduce the probability of outage, depending on the relationship between the transmitted signals at different antennas [73]. Considering that signals in wireless channels experience major multipath fading, MIMO is regularly combined with OFDM [42,73].

Optical fibre can support two polarization modes in which each polarization mode travels with a slightly different speed due to the PMD effect and experiences different loss caused by polarization-dependent loss (PDL) [4]. Therefore, optical fibre in essence exhibits the characteristics of a MIMO channel. MIMO, both with and without OFDM, has been employed in single-mode fibre (SMF) applications by transmitting and receiving signals on both polarizations. In this context, in optical fibre transmission systems, MIMO is also known as polarization multiplexing [74]. Nevertheless, MIMO in SMF has one significant difference from its wireless counterpart. In a polarization multiplexed transmission, all of the received signal power is divided between the two received polarizations; whereas in

wireless applications, the signals at different receive antennas are at best uncorrelated and there is always a probability of outage when no antenna is receiving a good signal [74].

It has been shown experimentally that by using polarization multiplexing very high data rate transmission can be realized both in single-carrier and OFDM transmission systems [7,74]. Recently, the great potential of the MIMO scheme in multi-mode fibre applications and space-division multiplexing using multi-core fibres has been demonstrated [75-77].

2.3.2.1. MIMO-CO-OFDM Signal Model

The complete CO-OFDM model requires mathematical description of the two-polarization coupling, including the polarization effects as well as the CD. Following the OFDM signal model in section 2.2 and using Jones vector expression, the transmitted OFDM time-domain signal, $\vec{S}(t)$, can be described as

$$\vec{A}(t) = \sum_{i=-\infty}^{+\infty} \sum_{k=1}^{N_{SC}} \vec{c}_{i,k} \prod (t - iT_s) \exp\left(2j\pi f_k (t - iT_s)\right) \tag{2.30},$$

with

$$\vec{A}(t) = \begin{pmatrix} A^X \\ A^Y \end{pmatrix} \tag{2.31}$$

$$\vec{c}_{i,k} = \begin{pmatrix} c_{i,k}^X \\ c_{i,k}^Y \end{pmatrix} \tag{2.32}$$

$$\prod(t) = \begin{cases} 1 & -\Delta_G < t \le t_s \\ 0 & t \le -\Delta_G, t > t_s \end{cases} \tag{2.33},$$

where N_{SC} is the number of OFDM subcarriers, $\vec{c}_{i,k}$ is the transmitted OFDM data vector in the form of the Jones vector for the k^{th} subcarrier in the i^{th} OFDM frame, f_k is the frequency for the k^{th} subcarrier, A^X and A^Y are the two polarization components of $\vec{A}(t)$. T_s, Δ_G, and t_s are the OFDM frame period, guard interval length, and observation period, respectively. The Jones vector is used to describe generic OFDM data vector regardless of the state of polarization at the OFDM transmitter.

In a conventional CO-OFDM system, a long-enough CP is required to handle fibre dispersions, including PMD and CD [7,24]. This condition is given by

$$\frac{c_0}{{f_0}^2}\left|D_t\right|N_{SC}\,\Delta f + DGD_{\max} \le \Delta_G \tag{2.34},$$

where f_0 is the frequency of the optical carrier, c_0 is the speed of light constant, D_t is the accumulated CD in the fibre link, N_{SC} is the number of subcarriers, Δf is the subcarrier channel spacing, and $DGD_{\max}$ is the maximum budget of the differential-group-delay (DGD). To take into account enough margin, $DGD_{\max}$ is empirically set to 3.5 times the mean PMD [7,24].

If we assume the use of a sufficiently long symbol period, by following the same procedure as that of Shieh and Athaudage in [50], and using the frequency-domain channel transfer factor for the polarization effects suggested in [78], we obtain the received symbol given by

$$\vec{r}_{i,k} = H\left(f_k\right)\times \vec{c}_{i,k} \times \exp\left(j\phi_i\right) + \vec{w}_{i,k} \tag{2.35},$$

with

$$H_k = H\left(f_k\right) = \exp\left(j\phi_D\left(f_k\right)\right)\times J_k \tag{2.36}$$

$$J_k = \prod_{q=1}^{N_{PMD}} \exp\left\{-\left(\frac{j\vec{\beta}_q f_k + \vec{\alpha}_q}{2}\right)\vec{\sigma}\right\} \tag{2.37}$$

$$\phi_D\left(f_k\right) = \pi.c_0.D_t.\frac{f_k^2}{f_0^2} \tag{2.38},$$

where $\vec{r}_{i,k}$ is the received data vector in the form of the Jones vector for the k^{th} subcarrier in the i^{th} OFDM frame; ϕ_i is the OFDM frame phase noise from the lasers at the transmitter and the receiver; $H\left(f_k\right)$ is a 2×2 channel response matrix including CD and DGD; $\vec{w}_{i,k}$ is the noise representation of the two polarization components; $\phi_D\left(f_k\right)$ is the phase dispersion due to the fibre CD; J_k is the Jones matrix for the fibre link; N_{PMD} is the number of

PMD/PDL cascading elements in the entire fibre link with each element represented by its PDL vector, $\vec{\alpha}$, and birefringence vector, $\vec{\beta}$ [78]; and, $\vec{\sigma}$ is the Pauli matrix vector.

2.3.2.2. MIMO-CO-OFDM Configurations

Considering the use of different numbers of polarization dimensions at the transmitter and the receiver, the architecture of MIMO-CO-OFDM systems can be grouped into four categories: (i) single-input single-output (SISO); (ii) single-input two-output (SITO): (iii) two-input single-output (TISO); and (iv) two-input two-output (TITO) [7]. Table 2.1 summarizes the characteristics of these configurations. Among these, SISO and TITO are the most commonly investigated ones due to the cost effective implementation and higher capacity, respectively.

Type of MIMO	Polarization Rotation Resilience	PMD Resilience	Relative Capacity	Relative Sensitivity (dB)
1x1 MIMO (SISO)	No	No	1	0
1x2 MIMO (SITO)	Yes	Yes	1	0
2x1 MIMO (TISO)	Yes	Yes	1	3
2x2 MIMO (TITO)	Yes	Yes	2	0

Table 2-1: Comparison of the characteristics of different MIMO-CO-OFDM architectures versus the single polarization implementation.

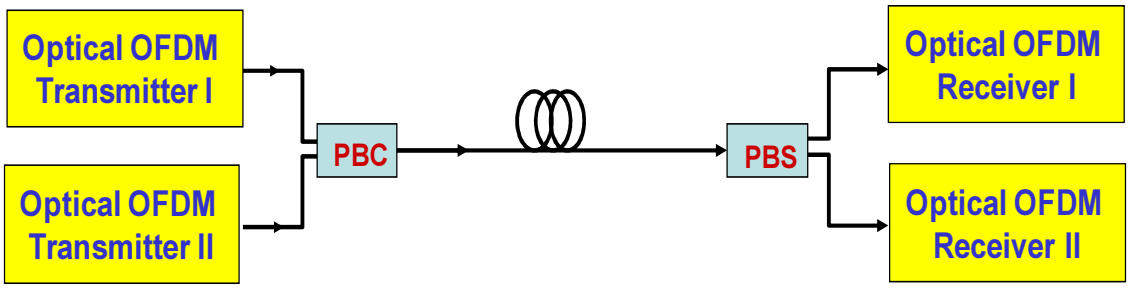

Figure 2-10: Diagram of the 2×2 MIMO-CO-OFDM system (also known as TITO).

The SISO configuration is an equivalent of single polarization transmission, which is susceptible to the polarization mode coupling effects in the optical fibre. A polarization

controller is required before the receiver to align the polarizations of the input signal and the local laser. More importantly, in the presence of large PMD, due to the polarization rotation between subcarriers, there is no uniform subcarrier polarization that the local receiver laser can be aligned to, and therefore, the polarization controller cannot function properly.

In a TITO or 2×2 MIMO-CO-OFDM scheme, both a polarization diversity transmitter and a polarization diversity receiver are employed, as shown in figure 2.10. There are three major advantages attributed to using the TITO configuration: (i) the capacity is doubled compared to the SISO scheme because the transmitted OFDM data vector can be considered to be polarization multiplexed. This can also be translated so as to achieve a fixed rate by using polarization multiplexing; the effective symbol rate is reduced to half that of single-polarization transmission, which enables the use of relatively lower-speed electronics; (ii) the impact of PMD can be treated with channel and phase estimation, and therefore, the doubling of the channel capacity is not affected by PMD; and (iii) due to the polarization diversity receiver employed at the receiver, the TITO scheme does not need dynamic polarization tracking at the receiver.

2.3.2.3. MIMO-CO-OFDM Channel Estimation

In this subsection, we study the associated channel estimation method for a 2×2 MIMO-CO-OFDM system. For notational simplicity, we drop the subcarrier index *k*. The associated channel model after removing the phase noise contribution in equation 2.35 can be expressed as

$$\vec{r}_i = H\vec{c}_i + w_i \tag{2.39},$$

where $\vec{r}_i = [r_i^X \quad r_i^Y]^T$ and $\vec{c}_i = [c_i^X \quad c_i^Y]^T$ are the received and transmitted OFDM vectors, respectively. H represents the channel transfer matrix describing the polarization effects and CD. H is assumed to have the form

$$H = \begin{bmatrix} H^{XX} & H^{XY} \\ H^{YX} & H^{YY} \end{bmatrix} \tag{2.40}.$$

To obtain the channel matrix, different structures of training sequence for channel estimation have been proposed. In the transmit-diversity scheme, two consecutive OFDM symbols are sent with orthogonal polarizations. These two consecutive OFDM pilot symbols (PSs) are usually the first and second of every data block, in the form of a Jones vector. The most computationally efficient scheme was proposed in [79], based on a pair of time-interleaved single-polarization PSs in which

$$\vec{c}_1 = [c_1^X \quad 0]^T, \quad \vec{c}_2 = [0 \quad c_2^Y]^T \tag{2.41}$$

Then, the channel matrix can be obtained simply by

$$H = \begin{bmatrix} H^{XX} & H^{XY} \\ H^{YX} & H^{YY} \end{bmatrix} = \begin{bmatrix} r_1^X / c_1^X & r_2^X / c_2^Y \\ r_1^Y / c_1^X & r_2^Y / c_2^Y \end{bmatrix} \tag{2.42}$$

However, the power of each PS frame is half that of the payload frame and this causes long-lasting power non-uniformity in the signal waveform, and results in large signal quality penalties to other OFDM channels due to the cross-phase-modulation (XPM) [50].

To solve this problem, Liu in [80], proposed the use of a pair of correlated symbols in dual-polarization PS frames expressed by

$$\vec{c}_1 = [c_1^X \quad c_1^Y]^T, \vec{c}_2 = [-c_1^Y \quad c_1^X]^T \tag{2.43}$$

This eliminates the power difference between the PS and the payload frames and consequently improves the signal tolerance to the XPM. Then, the channel matrix can be obtained by

$$H = \begin{bmatrix} H^{XX} & H^{XY} \\ H^{YX} & H^{YY} \end{bmatrix} = \frac{1}{2}\begin{bmatrix} \left(r_1^X + r_2^X\right)/c_1^X & \left(r_1^X - r_2^X\right)/c_1^Y \\ \left(r_1^Y + r_2^Y\right)/c_1^X & \left(r_1^Y - r_2^Y\right)/c_1^Y \end{bmatrix} \tag{2.44}$$

To increase the accuracy of the channel estimation in the presence of noise and nonlinearity, a time-domain averaging algorithm can be applied to average over multiple PSs. Alternatively, as been discussed in subsection 2.2.6.2, one can use the ISFA method in the frequency-domain.

2.3.3. Cyclic Prefix in CO-OFDM Systems

As we discussed in subsection 2.2.3, the cyclic prefix, as a form of guard spacing in the time-domain, is inserted between neighbouring OFDM symbols to prevent ISI due to the fibre dispersion. However, the insertion of CP reduces the spectral efficiency and the net system data rate. Moreover, the associated overhead increases for longer transmission distances and higher baud rates [7,24]. Therefore, different approaches have been investigated to mitigate the CP overhead and to improve the spectral efficiency. Yamada, in [52], proposed no-guard-interval CO-OFDM (NGI-CO-OFDM) where the OFDM signal is constructed with no CP and recently, Liu proposed the reduced-guard-interval CO-OFDM (RGI-CO-OFDM) scheme [25]. In this subsection, we briefly review these approaches.

2.3.3.1. Conventional CO-OFDM

At the transmitter side of a conventional CO-OFDM system, the data is mapped to the constellation points and then is modulated onto parallel subcarriers using an IFFT operation. Two DACs are used to transfer the I and Q signals to the analog domain. In an intradyne system, the electrical OFDM signal is then up-converted to the optical domain using a carrier-suppressed optical I/Q modulator.

At the receiver side, the optical signal beats with the LO and is next converted back to the electrical domain with balanced photo detectors. The I and Q signals are sampled by two ADCs and demodulated using the FFT operation. DSP algorithms for synchronization, frequency offset correction, and channel estimation are applied to recover the transmitted signal, as have been discussed earlier in this chapter.

2.3.3.2. No-Guard Interval CO-OFDM

Yamada in [52] proposed the NGI-CO-OFDM scheme to entirely eliminate the CP overhead. NGI-CO-OFDM is constructed similarly to a conventional CO-OFDM but without CP. In this approach, the linear distortion caused by CD and PMD is equalized by fixed-tap linear equalizers and adaptive finite impulse response (FIR) filters with blind channel estimation at the receiver [52,81]. Since blind adaptive equalization with a transversal filter is used to compensate the ISI, the NGI-CO-OFDM schemes do not require cyclic prefix and

training sequences. However, in using this method, ISI caused by the transmitter bandwidth limitations is not accommodated for, and also a more complex blind equalization is required to compensate for the effect of PMD.

2.3.3.3. Reduced Guard Interval CO-OFDM

In RGI-CO-OFDM systems, reduced CP between adjacent OFDM sequences are inserted to accommodate for the ISI induced by transmitter bandwidth limitations and fibre PMD, while the CD-induced ISI is compensated for at the receiver as with single-carrier frequency-domain equalization (SC-FDE) systems [25]. In the RGI-CO-OFDM, the CP only needs to be longer than the memory length associated with the PMD. Therefore, the overhead and OSNR penalty due to the CP insertion are dramatically reduced. In essence, the RGI-CO-OFDM is a hybrid version of the conventional CO-OFDM and the SC-FDE [83]. The RGI-CO-OFDM uses the same signal processing modules as the CO-OFDM. The only new processing module in RGI-CO-OFDM is the electronic dispersion compensation (EDC), based on FFT, IFFT, and overlap-add operations.

There are several benefits attributed to short CP and OFDM frame sizes: (i) shorter training sequences and therefore, a lower overhead, (ii) shorter OFDM frames, which leads to a higher channel tracking speed and consequently a higher tolerance to sampling frequency offset at the DAC and the ADC, and (iii) higher tolerance to the laser linewidth and the phase noise induced ICI.

The only expense that has been added in RGI-CO-OFDM systems is the signal processing required for performing the EDC. Nevertheless, considering the efficiency of conventional CO-OFDM signal processing [28] to start with, the overall complexity of RGI-CO-OFDM is believed to be slightly lower or similar to that of SC-FDE [83].

2.4. Conclusion

In this chapter, we reviewed the basics of orthogonal frequency division multiplexing (OFDM), including efficient signal modulation and demodulation using the FFT operation, the cyclic prefix insertion to tackle ISI and ICI in dispersive mediums, and the concept of

peak-to-average-power ratio (PAPR). Moreover, the required digital signal processing algorithms for synchronization and frequency offset correction were discussed. We also explained three commonly used channel estimation schemes, namely, the least square (LS), intra-symbol frequency-domain averaging (ISFA), and the maximum likelihood (ML). We then described different architectures used to realize the coherent optical OFDM (CO-OFDM) transmitter and receiver. An analytical model of multiple-input multiple-output (MIMO) CO-OFDM and the common methodology for channel estimation were presented. Lastly, we briefly reviewed different configurations for implementing CO-OFDM with CP overhead reduction. We believe the content of this chapter provides the necessary theoretical background regarding OFDM signal modulation/demodulation and signal processing in the context of CO-OFDM systems.

Chapter 3

Implementation of the Coherent Optical Transmission System

3.1. Overview

Coherent optical communication first came into the spotlight in the early 1990s; however, the intensity modulation enabled optical communication systems have remained a mainstay in research and industry since the invention of the erbium-doped-fibre amplifier (EDFA). Recently, advances in integrated circuit fabrication and digital-signal-processing (DSP) technologies have brought coherent optical communication to the forefront of this

research field [7]. The latest developments in DSP-enabled coherent optical communications follow the footsteps of wireless communications but at a much faster pace; techniques developed in the wireless community over the last few decades have been applied to the coherent optical transmission systems in the last few years.

In this chapter, we describe the implementation of our experimental coherent transmission system. In general, an optical coherent transmission system consists of a coherent transmitter, a fibre-optic transmission link and a coherent receiver. There are a variety of configurations described in the literature, some of which have been discussed in subsection 2.3.1, which can be used to implement the coherent transmitter and receiver. However, in this chapter, we focus on the intradyne coherent systems based on direct electro-optic (E/O) up-conversions and direct opto-electronic (O/E) down-conversions. In addition, we explain the concept of an optical recirculating loop as a common experimental instrument in optical communication laboratories to mimic the behaviour of a point-to-point optical transmission link.

3.2. Coherent Transmitter

Figure 3.1 provides a schematic diagram of the coherent transmitter setup. Continuous wave (CW) optical light is first generated by an Emcore external-cavity laser (ECL) with a nominal linewidth of less than 100 kHz. Then, by passing through an optical I/Q modulator, the CW light gets modulated via a complex RF signal that has been previously generated by an arbitrary waveform generator (AWG). In the absence of a second parallel transmitter to establish the polarization-multiplexed signals, the modulated optical signal is sent to a polarization multiplexing emulator. At the final stage of the transmitter side of the link, a booster EDFA, typically featuring high input power, high output power and medium optical gain, is used to amplify aggregated optical input power for reach extension. An OptiLab booster was used in our experiment. Finally, the resulting polarization-multiplexed optical signal is sent over the transmission link. In this section, we describe the key components of the coherent transmitter, namely, the AWG, the E/O up-converter, and the polarization-multiplexing emulator.

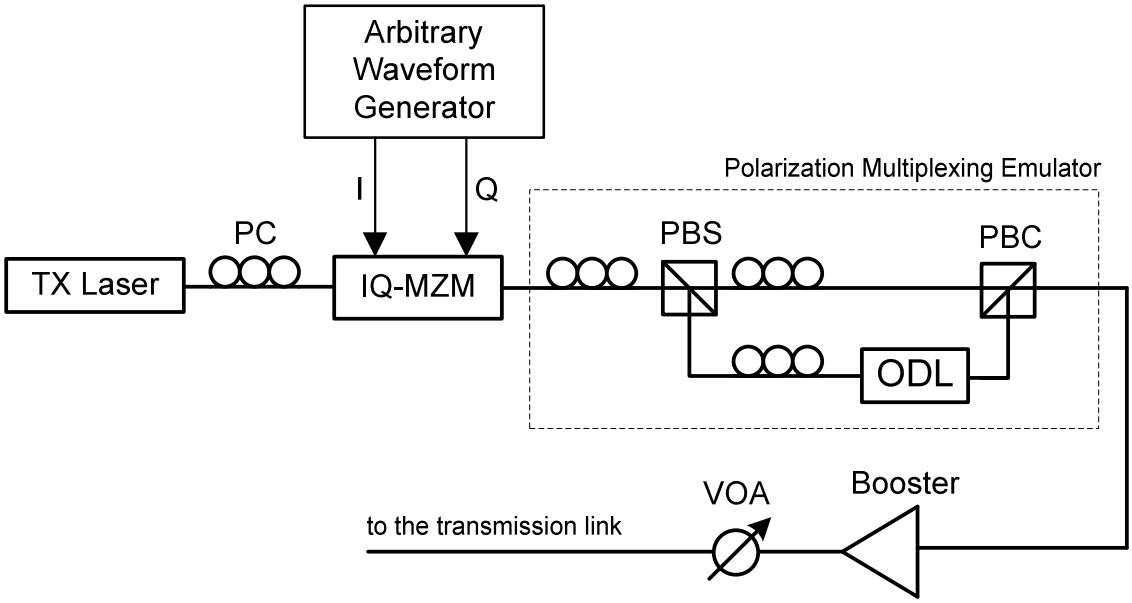

Figure 3.1: The diagram of a coherent optical transmitter. ODL refers to a tunable optical delay line (ODL).

3.2.1. Arbitrary Waveform Generator

An arbitrary waveform generator (AWG) is a testing and measurement device used to generate electrical waveforms. These waveforms can be either repetitive or single-shot. For single-shot waveforms either an internal or external triggering source is needed. Unlike function generators, an AWG can generate any arbitrarily defined waveform as its output. This waveform is usually defined as a series of points, i.e. specific voltage values occurring at specific times, and the AWG can either jump to those voltage levels or use interpolation techniques between the consecutive voltage values.

In our experimental setup, we used the MICRAM solution as an AWG with two outputs set as in-phase (I) and quadrature (Q), supporting a sample rate of up to 34 GS/s. As depicted in figure 3.2, the MICRAM solution consists of two VEGA digital-to-analog converters (DACs), two supporting VIRTEX-5 field-programmable gate arrays (FPGAs), and an external clock distributer. In the next two subsections, we briefly review the DAC and the FPGA concepts.

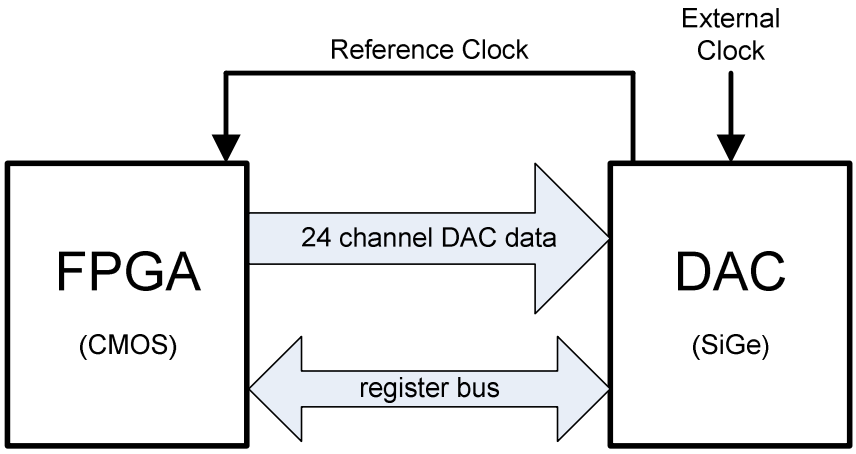

Figure 3.2: The diagram of MICRAM AWG.

3.2.1.1. Digital to Analog Converter

The most important unit in an AWG is the DAC. A DAC converts an abstract finite-precision digital number, usually a fixed-point binary number, into a physical quantity, in our case the signal voltage values. In particular, DACs are commonly used to convert a stream of data with a discrete time vector to a continually varying physical signal. A typical DAC converts the abstract numbers into a concrete sequence of impulses that are then processed by a reconstruction filter that uses interpolation to fill in the data between the impulses. There are three important parameters that quantify the performance of a DAC, as listed below.

Sampling rate: As per the Nyquist-Shannon sampling theorem, a DAC can reconstruct the original signal from the sampled data provided that the baseband signal has a bandwidth less than the Nyquist frequency.

Analog bandwidth: The analog bandwidth of a DAC describes the frequency range in which the output analog signal can pass through the circuit with minimal amplitude loss. It is specified as the frequency at which a sinusoidal input signal is attenuated by -3 dB. In real-time applications, the -3 dB bandwidth of a DAC is a critical standard for device selection. It should be guaranteed that the -3 dB bandwidth is wider than the bandwidth of the signal of interest to be generated [8].

Resolution: The resolution of a DAC is the reciprocal of the number of discrete steps in the output. This, of course, is dependent on the number of input bits, which is the base two logarithm of the number of levels. For instance, a 1-bit DAC is designed to reproduce 2 (= 2^1) levels while a 6-bit DAC is designed for 64 (= 2^6) levels. The digital sampling introduces quantization error that manifests itself as low-level noise that is added to the reconstructed signal [8,84]. In literature, the quantization error is also known as the quantization noise. Higher resolution results in lower quantization error; thus, better signal generation quality can be achieved. However, all real signals contain a certain amount of noise due to the circuits of the AWG. If the converter is able to represent signal levels below the system noise floor, the lower bits of the digitized signal will represent only the system noise, and do not contain useful information. Effective number of bits (ENoB) specifies the number of bits in the digitized signal that are above the noise floor, considering both the system noise and bandwidth.

In case of the MICRAM AWG in our experiment, the VEGA DACs have analog differential outputs that can also be used single-endedly. They provide up to 800 mV of voltage amplitude swing and support an analog bandwidth of 20 GHz at the maximum amplitude. An external clock is required to drive the DACs at half-rate, i.e. at 17 GHz for 34 GS/s. To adjust the sampling points or to synchronize the two VEGA DACs, equivalently to skew the I signal versus the Q signal, the sampling phase can be adjusted within a 100 ps range. In addition, having a nominal resolution of 6 bits, a measured ENoB of greater than 4 bits at 30 GS/s for sinusoidal differential signals up to 5 GHz is reported.

3.2.1.2. Field-Programmable Gate Array

An FPGA is a semiconductor device that can be configured by the user in the field. FPGAs are designed using either a logic circuit schematic or source code in a hardware description language (HDL), to specify how the chip should work. They can be used to implement any logical function that an ASIC could perform, with the additional characteristic that the user can reconfigure the functionality of the device. This obviously offers advantages for many applications, including laboratory tests and investigations. An FPGA consists of both programmable logic components called configurable logic blocks (CLBs) and

a chain of reconfigurable interconnects that allow the blocks to be wired together. CLBs can be configured to perform both complex combinational functions and basic logic gates [85].

To define the behaviour of the FPGA, hardware description languages, such as VHSIC hardware description language (VHDL), were developed to investigate and verify the circuit operation. Using the electronic design automation (EDA) tool for FPGA design, a technology-mapped netlist is generated from the VHDL code. The netlist can then be fitted to the actual FPGA architecture using a process called place-and-route. The designer will first verify the functionality of the design based on programmed VHDL files. After the place-and-route process, the design is further validated based on the generated netlist file for timing analysis. Once the design and validation processes have been completed, the generated configuration file is used to configure the FPGA in order to achieve the desired functionality.

Modern FPGAs support more functionality fixed in the silicon, including different DSP blocks, high-speed I/O transceivers, embedded processors, and embedded memory blocks. By embedding these general functions into the silicon, one can reduce the required footprint and increase the processing speed [85].

For the case of the MICRAM AWG solution, due to the massive signal and data processing in the digital domain, the FPGA architecture offers a parallel interface. The data transfer from the FPGA is carried via 24 serial lines running at $f_{sample}/4$, i.e. at 8.5 Gb/s for 34 GS/s. In addition, the FPGAs are equipped with an evaluation board, a microcontroller, and a software application to control operation modes and to check the synchronization of the 24 FPGA channels.

3.2.2. Electro-Optic Up-Conversion

Direct E/O up-conversion is possible using an optical I/Q modulator. An optical I/Q modulator comprises two parallel inner Mach-Zehnder modulators and one outer phase modulator. The two parallel MZ modulators convert the two electrical data streams (I and Q) into one optical data stream. Before superposition of the two optical signals, the outer

phase modulator shifts the phase of the Q stream by $\pi/2$ in order to construct a complex signal [4]. In our experiment, we use the SHF 46213D as the QAM electro-optic transmitter unit. It is a field replaceable plug-in module that needs to be installed in a mainframe, type SHF10000A, where all three internal modulators are based on a chirp-free Lithium Niobate structure and are thermally stable. The SHF 46213D transmitter also includes two non-limiting wideband RF amplifiers acting as the drivers of the I and Q modulator ports. The SHF 46213D is specified for a combined analog E/O bandwidth of 25 GHz.

3.2.3. Polarization Division Multiplexing

In a real polarization multiplexed optical transmission system the two optical signals with different polarizations are generated using different transmitters. In the case when access to only one optical transmitter is possible, a common experimental practice is to take advantage of an optical polarization division multiplexing emulator setup. This cost-effective method is adopted to emulate the two transmitters, as shown in figure 3.1. The single-polarization optical signal at the output of the I/Q modulator is first evenly split into two polarization branches via a polarization beam splitter (PBS), with one branch delayed to de-correlate the two streams. In the case of OFDM, this delay is often equal to one or two OFDM symbol periods [25,79]. The two de-correlated polarization branches are subsequently combined, thereby emulating two independent transmitters, one for each polarization. This method results in a composite data rate that is twice that of the single polarization scenario. The two polarization components are completely independent due to the de-correlating delay.

3.3. Transmission Link

The optical transmission link mainly consists of a recirculating loop to emulate long distance transmission. In this section, we review the structure of a recirculating loop. In addition, we provide a brief overview of the noise loading setup as a technique to emulate the effect of accumulated noise in long-haul transmission systems.

3.3.1. Optical Recirculating Loop

A fibre-optic recirculating loop is a setup in which the optical signal can undergo a desired number of consecutive round trips in a loop made of optical fibre and EDFA. Its main application is for studying long-haul transmission in optical fibre communication systems. Even with a limited length of fibre, the propagation of signals over very long distances can be studied by using multiple passes. This setup allows for an investigation of the adverse effects of optical fibre transmission impairments, such as accumulated spontaneous emission (ASE) noise, chromatic dispersion (CD), polarization mode dispersion (PMD), and nonlinearities, on the signal quality. In laser technology, recirculating loops are also used for the measurement of the linewidth of a laser, particularly in cases where the linewidth is very small, for instance below 1 kHz. This approach is an extension of the self-heterodyne linewidth measurement; the use of an extra reference laser can be avoided by deriving the reference signal from the laser output itself by using the long delay provided by a long single-mode fibre (SMF).

A typical optical recirculating loop consists of two acousto-optic switches (AOSs), a pulse generator, fibre amplifiers, and optical fibre. A diagram of a recirculating loop, based on EDFA lumped amplification, is shown in figure 3.3. The loop switch controller, which injects and circulates the bit stream, is an active component in a recirculating loop. The signal is coupled into the loop by means of a four-port optical 3-dB coupler. The AOSs are essential elements in the loop switching mechanism and work in counter-phase; when AOS #1 is in the ON state, AOS #2 is in the OFF state with no light propagating through it, and vice versa. When AOS #1 is open (in the ON state), the optical signal passes through to the 3-dB coupler, at which point half of the signal goes to the receiver and the other half goes into the loop. By the time the signal reaches the end of the loop, AOS #1 closes (enters the OFF state), and AOS #2 opens (enters the ON state). Thus, as long as AOS #2 is open the signal circulates in the loop.

Variable optical attenuators (VOAs) can be used to balance gain and loss after each round trip so that the total signal power after each round-trip remains constant. This balance operation eliminates the transient response of the EDFAs, which may damage the optical

components in the loop. EDFAs with the capability of adjustable gain control do not need this VOA as the proper gain can easily be assigned to match the corresponding span loss. The pulse generators are used to trigger the AOSs. The length of the burst generated for AOS #1 is adjusted in such a way to have the signal fit entirely within the loop. The duty cycle of the pulse is adjusted in such a way as to allow for the burst to recirculate in the loop as many times as necessary for the investigation. A 5% tap is often used in the loop switch to monitor the signal spectrum on an optical spectrum analyzer (OSA) at any given circulation. In addition, it is worth mentioning that even though the AOSs are designed to be polarization-insensitive, they may exhibit some polarization-dependent loss (PDL).

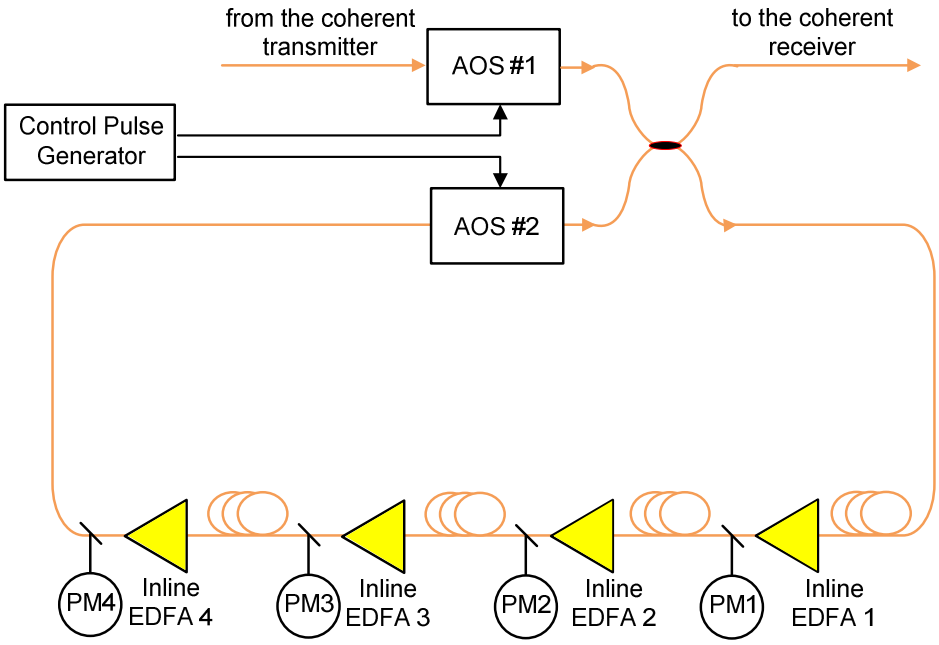

Figure 3.3: The diagram of the optical recirculating loop.

An optical recirculating loop can be equipped with polarization scrambler to emulate and study the effect of the speed of PMD changes and the polarization dependent loss (PDL). In addition, adjustable low pass filtering can be applied in the loop to emulate those transmission systems with wavelength selective switches (WSSs).

3.3.2. Noise Loading

In optical fibre communications, the practice of adding broadband noise from an amplified spontaneous emission source is often used to determine the system tolerance, particularly at the receiver, to the optical signal-to-noise ratio (OSNR). This practice is referred to as noise loading. It has been assumed that the outcome of noise loading is equivalent to the effect of noise built up in a real amplified transmission system using erbium-doped-fibre-amplifiers (EDFAs). Although the interaction between the noise and CD, as well as fibre nonlinearities, makes the above-mentioned assumption less accurate, noise-loading is a popular experimental exercise to investigate either the sensitivity of a receiver or the performance of an equalizer. The output of a high power EDFA when no input has been fed into it provides a broadband noise source that can be added to the optical signal using an optical coupler. A variable optical attenuator (VOA) can be used at the output of the EDFA to adjust the noise power without altering the noise spectrum.

3.4. Coherent Receiver

Figure 3.4 shows a diagram of the coherent receiver. The optical signal first beats with the CW light of the local oscillator (LO), generated by an Emcore ECL with a nominal linewidth of less than 100 kHz, in an optical polarization-multiplexed hybrid. The resulting optical signals then illuminate four balanced photodetectors for opto-electronic (O/E) down-conversion. Next, the electrical signals are fed into the electrical sampling unit to provide the data for off-line processing. In this section, we describe the key components in the coherent receiver, namely, the out-of-band noise mitigation, O/E down-conversion, and the electrical sampling unit.

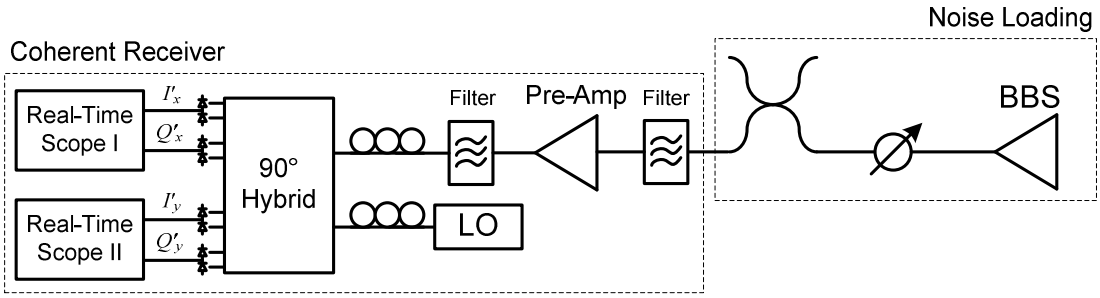

Figure 3.4: The diagram of the optical coherent receiver and the noise loading setup.

3.4.1. Out-of-Band Noise Mitigation

The received optical signal typically has a relatively low optical power that requires amplification. Pre-amplifiers are designed for optical amplification in order to compensate for losses at the receiver from components such as de-multiplexers, optical hybrids, and optical filters. A pre-amplifier EDFA, featuring medium to low input power, medium output power and medium gain, is commonly included at the receiving end of an optical link. As we see in figure 3.4, at the receiver, an optical filter is required before the pre-amplifier in order to remove the out-of-band accumulated spontaneous emission (ASE) noise. The importance of this filter is in preventing the pre-amplifier from getting damaged due to excessive input noise power accumulated after long distance transmission, and from gain saturation, which could potentially increase its noise figure and consequently compromise its noise performance. A second optical filter is used after the pre-amplifier to filter out the out-of-band noise generated by the pre-amplifier.

Employing these optical filters would be going against the concept of colorless network deployment, unless an expansive active tracking system is used to tune the filter wavelengths. Therefore, researchers generally try to eliminate the need for the pre-amplifier and, consequently, the optical filters by using integrable non-limiting wideband transimpedance amplifiers (TIAs) in the electrical domain after the signal has passed through the photodetectors [86,87].

3.4.2. Opto-Electronic Down-Conversion

The opto-electronic (O/E) down-conversion in a polarization diversity configuration can be achieved using a dual-polarization optical hybrid and four pairs of balanced photodetectors. A hybrid is a six-port device that has been used for wireless detection systems for several decades and is a key component in coherent receivers. In principle, this six-port device consists of linear dividers and combiners interconnected in such a way that four different vectorial additions of a reference signal, LO, and the signal to be detected are obtained. Balanced receivers detect the levels of the four output signals. For optical coherent detection, the six-port 90° optical hybrid would mix the transmitted signal with the four quadratural states associated with the reference signal, the LO laser, in the complex-field space. The optical hybrid would then deliver the four optical signals to two pairs of balanced detectors, as shown in figure 3.4. Based on two single-polarization optical hybrids, a dual-polarization optical hybrid achieves the same functionality for both polarizations. In our experiment, we used the Kylia COH28 as the dual-polarization 90° optical hybrid.

Four u2t BPDV2020, all with a nominal bandwidth of 43 GHz, were employed as the balanced photodetectors. Each photodetector consists of two waveguide-integrated photodiodes on a single chip connected together to form a balanced detector. The waveguide approach guarantees a linear frequency response in amplitude, as well as in phase, even at relatively high optical powers. The integrated 50 Ohm termination provides the matching for the electrical signal, used to increase the power efficiency.

3.4.3. Electrical Sampling Unit

Having mapped the signal from the optical domain into the electrical domain, the next step is to convert the received analog signals into a set of digital signals. In our setup, two real-time oscilloscopes, Agilent Infiniium 90000 X-series, with a combined analog bandwidth of 33 GHz, a combined sampling rate of 80 GS/s, and a resolution of 8 bits were employed as the sampling front-end.

The principle component of a real-time oscilloscope is the analog-to-digital converter (ADC) that is required to transform the analog signal into a vector of digital samples. We briefly review the concept of an ADC in the following subsection.

3.4.3.1. Analog to Digital Converter

From a systematic point of view, an ADC is made up of two subsystems: a sampler and a quantizer. The sampler subsystem samples the signal in time and converts the continuous-time analog signal into a discrete-time analog signal. The quantizer is necessary to convert this discrete-time analog signal into a finite set of values determined by the bits of resolution of the ADC. There are three important parameters in characterizing the ADC performance; they are listed below.

Sampling rate: For a digital communication system transmitting symbols at a rate of S symbols per second, the minimum sampling rate is S Hz. For asynchronous sampling, however, a sampling rate of $2S$ Hz is generally required; thus, two samples per symbol are required to enable digital timing recovery [8]. In practice, there is normally a slight difference between clocks of the transmitter and the receiver. To resolve this issue, the analog signal may be re-sampled by interpolating the digital signal since the digital receiver does not require a clock frequency equal to the symbol rate, as does its analog counterpart. In addition, the Nyquist theorem states that a signal must be sampled at a rate greater than twice its highest frequency to accurately reconstruct the waveform; otherwise, the high frequency content will alias to a frequency inside of the spectrum of interest. In real-time CO-OFDM reception, the ADC should be carefully selected so that its sampling rate is at least two times the upper limit of subcarrier frequencies.

Analog bandwidth: The analog bandwidth of an ADC describes the frequency range in which the analog input signal can pass through the circuit with minimal amplitude loss. In real-time applications the -3 dB bandwidth of the ADC is a critical parameter, and it should be guaranteed that the -3 dB bandwidth is wider than the bandwidth of the received OFDM signal [8].

Resolution: The resolution of the ADC indicates the number of discrete values it can produce over the range of the analog input. The values are usually stored in a binary format so

the resolution is usually expressed in bits. Consequently, similar to the DAC, the number of discrete values is usually a power of two. For instance, an ADC with a resolution of 8 bits can encode an analog input to one of 256 different levels. Similar to the DAC, the difference between the ideal transfer function and the actual transfer function of the ADC with finite resolution is defined as the quantization error.

There are several techniques for implementing a high-speed ADC: (i) the flash approach, where performance is limited by the accuracy of the clock and the comparator characteristics; (ii) the flash with track and hold approach, which reduces the demand on the comparator, but instead has performance limited by the track and hold process; (iii) the time-interleaved approach, which uses lower speed ADCs but requires offset, delay, and gain correction [8,84]. Of the aforementioned techniques, it is the time-interleaved structure that supports CMOS implementation and therefore, integration with the DSP in a single application-specific integrated circuit (ASIC). However, to avoid spurious tones at the clock rate of lower speed ADCs, the time-interleaved configuration requires precise compensation of the offset, delay, and gain of the lower speed ADCs [8,84,88].

3.5. Conclusion

In this chapter, we briefly reviewed the implementation of our experimental coherent transmission system based on the intradyne scenario. First, the structure of the coherent transmitter, including DAC operation, FPGA structure, E/O up-conversion, and polarization division multiplexing emulator, was explained. Then, the setup for the optical recirculating loop, acting as the point-to-point optical transmission link, was described. Lastly, the coherent receiver, consisting of the setup for out-of-band noise mitigation, O/E down-conversion, and the ADC, was explained.

We believe that the content of this chapter provides the concise experimental review required for introducing and investigating the DSP algorithms of interest for CO-OFDM systems in next two chapters.

Chapter 4

Adaptive Decision-Directed Channel Equalization for CO-OFDM

4.1. Overview

Following the recent surge of interest in digital signal processing (DSP) for optical fibre communications, coherent-optical orthogonal-frequency-division-multiplexing (CO-OFDM) has been intensively investigated as a possible modulation format for future un-compensated fibre optic transmission links. However, it is widely recognized that the ex-

cessive overhead to be one of the major drawbacks in the implementation of CO-OFDM transmission systems [7,89].

In this chapter, we study the overhead of a typical CO-OFDM system and characterize its associated optical signal-to-noise-ratio (OSNR) penalty. We introduce our work on overhead reduction in CO-OFDM systems based on a combination of decision-directed and data-aided channel estimation algorithms; this includes earlier work on single-polarization CO-OFDM, namely, the adaptive weighted channel equalizer (AWCE) [34] and decision-directed phase equalizer (DDPE) [38]. We then expand this idea to polarization-multiplexed CO-OFDM systems by proposing the adaptive decision-directed channel equalizer (ADDCE) [35]. We experimentally study the performance of ADDCE at 28 GBaud for reduced-guard-interval dual-polarization CO-OFDM (RGI-DP-CO-OFDM) transport systems with both quadrature-phase-shift-keying (QPSK) and 16-quadrature-amplitude-modulation (16-QAM) formats. In addition, we provide a brief analysis of the complexity of ADDCE, in terms of the number of required complex multiplications, and compare it with the complexity of a conventional equalizer (CE).

4.2. Motivation

Channel estimation is one of the subcarrier signal recovery processes required for completing the signal equalization. Its critical importance to the overall system performance and its close relation to other issues, such as tracking speed and error correction, make it one of the most extensively researched topics in the field of OFDM [7]. A variety of channel estimation techniques can be generally categorized into the subgroups of blind, decision-directed, and data-aided estimations [42,90,91]. In CO-OFDM systems, the data-aided estimation technique is preferred as it offers the least computational complexity; however, the required cumulative overhead can be excessive for typical long-haul optical transmission systems, thus reducing the flexibility of the network design [7,10,24].

In this section, we first review the concept of blind, decision-directed, and data-aided estimations. Then, we elaborate on the required overhead for CO-OFDM signal processing and the associated OSNR penalty.

4.2.1. Blind vs. Decision-Directed vs. Data-Aided Estimations

In optical transport systems, considerable distance separates the transmitter and receiver; therefore, the estimator at the receiver does not have practical access to the transmitted signal that entered the channel. When a receiver does not have any knowledge of the transmitted signal, it must employ blind channel estimation [91-93]. The constant-module-algorithm (CMA) is a well-known example of a blind estimation scheme that is often used in single-carrier transmission systems [94,95].

If the receiver uses the detected symbols to reconstruct the transmitted signal, and then uses this signal in place of the original signal, it is using a subclass of blind estimation referred to as decision-directed estimation. An obvious downfall of these methods is that a wrong decision at the receiver may result in the reconstruction of an incorrect transmitted signal. In the case of channel estimation, this decision error can introduce a bias in the channel estimation, compromising the performance of the equalizer [42,90].

Data-aided equalization techniques rely on a known training sequence that is used to estimate the channel. The receiver can use this training sequence to reconstruct the transmitted waveform. While this method produces more accurate estimates of the channel during the training interval, these estimates become out-of-date between intervals, unlike the continually updated estimates of the blind techniques. Therefore, training sequences should be transmitted periodically in order to allow the receiver to continuously estimate the dynamic channel. The drawback of data-aided estimation is that the training sequence occupies valuable bandwidth, reducing both the overall throughput and the spectral efficiency of the transmission system. In the literature, this is often referred to as overhead [42,90]. The overhead can be perceived either as a data rate overhead or a power overhead.

Blind estimation schemes are known to be very complex to implement in real-time OFDM systems. On the other hand, the decision-directed channel estimation is not a reliable solution as the equalization parameters are not from training sequences, and thus the estimator's performance may suffer from error propagation. For these reasons the data-aided estimation schemes, based on pilot symbols (PSs) and pilot subcarriers (PSCs), are

usually employed in OFDM systems (as discussed in subsection 2.2.6). To overcome the shortcomings of decision-directed and pilot-aided channel estimators, one can combine the two methods, as suggested in [96-98]. This combination allows the estimator to utilize both receiver decisions and pilots, thus, it can produce a more accurate estimation, and consequently better equalization, when the receiver decisions are correct.

4.2.2. CO-OFDM and Overhead

Excluding the forward-error-correction (FEC), the overhead of CO-OFDM transport systems with data-aided estimation has three different origins, namely pilot symbols (PSs), pilot subcarriers (PSCs), and cyclic prefix (CP). In this subsection, we review the contribution of each and quantify their associated OSNR penalties.

Pilot Symbols (PSs): One of the key features of digital signal processing (DSP) in optical fibre transmission systems is the capability of sending pilot symbols (PSs), or training sequence (TS), that are known to the receiver in order to provide channel estimation. In CO-OFDM, least square (LS) estimation and zero-forcing (ZF) detection methods have been frequently used to extract the channel information and to calculate the equalization parameters [24,99]. By comparing the received PS with the transmitted PS, whose subcarriers are known, the channel transfer function for each subcarrier can be extracted using a single complex division. The accuracy of this estimation is often limited by the presence of noise and pattern dependent nonlinearities. To increase the accuracy of channel estimation a time-domain averaging method, in which multiple PSs are used to extract the channel transfer function matrices [65], is commonly employed. The improvement can also be obtained by averaging in the frequency-domain over multiple subcarriers, as presented in subsection 2.2.6.2. To combat the dynamic changes in channel characteristics, the PSs are periodically inserted into the OFDM data symbol sequence so that the channel estimation can be performed periodically, thus tracking the dynamic behaviour of the channel. This presumes a stationary (non-varying) channel for the block of data symbols between each two consecutive sets of PSs; therefore, PSs should be sent at a rate that is much higher than the rate of significant physical changes of the channel. In fibre-optic communications, these physical

changes mainly originate from the polarization mode dispersion (PMD) and the laser phase noise. The PMD varies due to the mechanical and temperature fluctuations on a millisecond time scale [66], however, there are reports on microsecond PMD changes under severe mechanical stress [67]. In [37], Jansen reported 25.8 Gb/s CO-OFDM by employing 2 pilot symbols for each 25 data symbols, resulting in a 4% overhead due to the TS insertion. Buchali, in [12], reported a PS overhead of 5%. The PS overhead can be alternatively expressed as an increase in the required optical signal-to-noise ratio (OSNR), defined as $\Delta\text{OSNR}_{\text{PS}}$

$$\Delta OSNR_{PS}(dB) = 10 \times \log\left[\left(m_{SYM} + m_{PS}\right)/ m_{SYM}\right] \tag{4.1},$$

where m_{SYM} and m_{PS} are the number of the data symbols and pilot symbols per block, respectively.

Pilot Subcarriers (PSCs): The output of a single-frequency laser exhibits phase noise which results in the finite linewidth, normally ranging from 100 kHz to several megahertz [7], of the laser output. Therefore, laser phase noise needs to be tracked on a symbol-by-symbol basis. By using the PSCs that are inserted in every OFDM symbol the fast time variation of the channel can be compensated for. The PSCs are equally distributed over the OFDM spectrum and their state of modulation is known at the receiver. Yi, in [69], studied the number of required pilot subcarriers for CO-OFDM systems. An overhead of 2% to 5% is expected because of the PSC insertion [7,10,24]. Due to the insertion of pilot subcarriers a fraction of the transmitted and received optical power is not used for data transmission, leading to an increase in the required OSNR, defined as

$$\Delta OSNR_{PSC}(dB) = 10 \times \log\left[\left(N_{SC} + N_{PSC}\right)/ N_{SC}\right] \tag{4.2}.$$

where N_{SC} and N_{PSC} are the number of OFDM subcarriers and pilot subcarriers (PSCs), respectively. In [37,100], authors proposed an RF-pilot enabled phase noise compensation method for CO-OFDM systems in which ideally no extra optical bandwidth needs to be allocated. With this technique, phase noise compensation is realized by placing an RF-pilot tone in the middle of the OFDM band at the transmitter. This RF-pilot is subsequently used at the receiver to remove phase noise impairments. However, there is a trade-off for varying

levels of RF-pilot power: for low-power RF-pilots, the accumulated spontaneous emission (ASE) noise reduces the degree for which the phase noise can be compensated for, whereas for high-power RF-pilots, the OSNR of the OFDM signal becomes too low and the received signal quality degrades [37,100].

Cyclic Prefix (CP): The orthogonality of subcarriers in OFDM can be compromised in the presence of inter-symbol-interference (ISI). In practice, since the spectra of the OFDM signal is not band limited, linear distortion, such as multipath in wireless or chromatic dispersion (CD) in optical fibre, would cause each subcarrier to spread its energy into adjacent channels and consequently result in ISI. As discussed in chapter 2, to prevent ISI, CP is inserted as a guard interval where each OFDM symbol is preceded by a periodic extension of its rear portion. The reported CP overhead values in conventional CO-OFDM systems vary from 10% to 20%, depending on the amount of accumulated CD and the transmission baud rate [7,12]. Reduced-guard-interval CO-OFDM systems have been recently proposed to reduce the required CP overhead. Liu, in [25], reported a CP overhead of less than 3%. The CP overhead can also be translated into an increase in the required OSNR as

$$\Delta OSNR_{CP}(dB) = 10 \times \log\left[\left(T_S + T_{CP}\right)/T_S\right] \qquad (4.3),$$

where T_S and T_{CP} are the duration of the OFDM symbol and the length of the CP, respectively.

Considering the aforementioned discussion, and by examining equations 4.1, 4.2, and 4.3, one can realize that the cumulative overhead and its resulting OSNR penalty can strain the spectral and power efficiency of the optical transport system. In addition, by increasing the transmission baud rate and/or the transmission reach, the required overhead, or equivalently the OSNR penalty, would constrict the design margin requirements of the network.

4.3. Our Earlier Work on Single-Polarization Systems

As discussed earlier, some preliminary work on single-polarization conventional CO-OFDM systems has been accomplished based on a combination of decision-directed and data-aided channel estimation algorithms. Two different equalizers have been proposed:

adaptive weighted channel equalizer (AWCE) [34], and decision-directed phase equalizer (DDPE) [38,101].

AWCE updates the equalization parameters on a symbol-by-symbol basis after an initial decision making stage and retrieves an estimation of both the channel response and the phase noise value by extracting the decision information of all OFDM sub-channels. By using this information the channel transfer factor for the equalization of the next received OFDM symbols gets updated. This is suitable for avoiding PMD degradation while increasing the periodicity of the PSs, translating into a significant overhead reduction. A second equalization is performed using the estimated phase noise value, followed by a final decision making stage. As a result, AWCE can increase the precision of the data-aided phase noise estimation by further applying the decision-directed phase estimation. Simulation results corroborate the capability of AWCE in both overhead reduction and improving the quality of the phase noise compensation.

DDPE operates similar to AWCE with the only difference being that the phase noise compensation is purely decision-directed. We report and investigate the feasibility of zero-overhead laser phase noise compensation for long-haul CO-OFDM transmission systems. Furthermore, we numerically compare the performance of DDPE and the conventional equalizer (CE) for different laser linewidth values.

In this section, we first review the operational concept of these channel estimation and equalization algorithms and then present our numerical investigation on their performance in long-haul conventional CO-OFDM transmission systems.

4.3.1. The Concept of AWCE and DDPE

Assume i denotes the index for the received symbol (time index) and k is the index for the OFDM subcarrier (frequency index). The subcarrier-specific received complex value symbol, $r_{i,k}$, is equalized by applying LS estimation and zero-forcing (ZF) detection based on the previously estimated transfer factor, $\widetilde{h}_{i-1,k}$, that is taken as a prediction of the current channel transfer factor. Therefore,

$$\hat{S}_{i,k} = \frac{r_{i,k}}{\widetilde{h}_{i-1,k} e^{j\Delta\varphi_{pilot,i}}} \tag{4.4}$$

where $\hat{S}_{i,k}$ is the subcarrier-specific equalized complex value symbol and the term $\Delta\varphi_{pilot,i}$ is used to compensate for the laser phase noise which can be extracted by using RF-pilot [100] or pilot subcarriers [24]. $\widetilde{h}_{0,k}$ is normally derived from the PSs that are inserted at the beginning of each block of OFDM data symbols. $\hat{S}_{i,k}$ is then detected by the demodulator to make a decision as

$$\overline{S}_{i,k} = Decision\left\langle \hat{S}_{i,k} \right\rangle \tag{4.5}$$

where $\overline{S}_{i,k}$ is the detected symbol. Presuming that the decision was correct, the received symbol, $r_{i,k}$, can be further divided by the detected symbol in order to calculate a new channel transfer factor, $\hat{h}_{i,k}$, given by

$$\hat{h}_{i,k} = \frac{r_{i,k}}{\overline{S}_{i,k}} \tag{4.6}$$

We name this new channel transfer factor as the ideal channel transfer factor; if this transfer factor is known prior to demodulation it can be applied as the denominator in equation 4.4, and, thus, perfect equalization and decision making would be achieved. $\hat{h}_{i,k}$ is the updated version of $\widetilde{h}_{i-1,k}$ and includes information on the optical channel drifts in the time interval of the symbol number *i*. A low-pass filter (LPF) can be applied to $\hat{h}_{i,k}$ to suppress the high-frequency detected noise without applying time averaging over several channel transfer functions in each block as presented in [102].

At this point, a more accurate estimation of laser phase noise can be provided that can subsequently lead to better phase noise compensation. To achieve this improvement, we average the difference between the phase term of the ideal channel transfer factor and the phase term of the previously estimated transfer factor over all subcarriers as

$$\Delta\varphi_{AWCE,i} = \left(\sum_{q=1}^{N_{SC}} \left(\arg\left\{ \hat{h}_{i,q} \right\} - \arg\left\{ \widetilde{h}_{i-1,q} \right\} \right) \right) \Big/ N_{SC} \tag{4.7}$$

where N_{SC} is the total number of OFDM subcarriers, including all data subcarriers. Equation 4.7 tries to extract the phase drift of the optical channel in the time interval equal to the duration of one OFDM symbol and assumes that the drift due to PMD is negligible. This is a good assumption since PMD variations occur slowly (in the range of kHz) in comparison with the typical CO-OFDM symbol rate. Now, $\Delta\varphi_{pilot,i}$ in equation 4.4 can be replaced by $\Delta\varphi_{AWCE,i}$, as a more accurate estimation, and the new resulting $\hat{S}_{i,k}$ is again sent to the demodulator for better decision making. As we see in equation 4.7, since $\Delta\varphi_{AWCE,i}$ is calculated by averaging over all OFDM sub-channels, it is capable of suppressing the effect of ASE noise, providing more accurate phase noise estimation. However, because the calculation of equation 4.7 is done after the first demodulation, fairly reliable data-aided phase noise estimation is indispensable in preventing error propagation.

To update the equalization parameters for the next received symbol, we apply a simple recursive filtering procedure using both the previously estimated channel transfer factor, $\tilde{h}_{i-1,k}$, and the ideal channel transfer factor, $\hat{h}_{i,k}$. The recursion is performed independently for each subcarrier and a time-domain correlation is implicitly utilized. No channel statistics, such as correlation function or signal-to-noise ratio (SNR), are needed. The estimated channel transfer factor for the i^{th} received symbol can be updated using

$$\tilde{h}_{i,k} = (1-\gamma_i)\hat{h}_{i,k} + \gamma_i \tilde{h}_{i-1,k} e^{j\Delta\varphi_{AWCE,i}} \quad (4.8),$$

where γ is the adaptive weighting parameter and can take any value between 0 and 1. A large value of γ boosts the role of previously estimated channel transfer function, $\tilde{h}_{i-1,k}$, in equation 4.8 and, conversely, a smaller value of γ increases the effect of the ideal channel transfer function, $\hat{h}_{i,k}$. γ can control the recursion and prevents error propagation. If the previous equalization is fairly accurate and a good decision is made it implies that $\tilde{h}_{i-1,k}$ was precise and, subsequently, we would like to boost its role in equation 4.8, thus, a large value of γ is desired. However, if the previous equalization is not accurate then we are interested in increasing the role of $\hat{h}_{i,k}$ in order to update the equalization parameters; there-

fore, a smaller value for γ is preferred. As we see, γ should be defined in a way that can assess the quality of the previous equalization. Due to noise, nonlinearities, inaccurate phase noise estimation, and small PMD drifts in the optical channel, the equalized received constellation points do not exactly lay on the ideal constellation points, defining error vectors. We use these error vectors to assess the precision of the previous equalization. Focussing on one symbol and keeping the above-mentioned requirements in mind, we define γ as

$$\gamma = 1 - \left| avg\left\{ \vec{e} / d \right\} \right| \tag{4.9},$$

where $\vec{e}$ and d denote the error vector of one received constellation point and the distance between the ideal constellation point and the closest decision line, respectively, as shown in figure 4.1.a for the case of a quadrature phase-shift keying (QPSK) constellation. The avg implies an averaging over all equalized constellation points in each received symbol. Figure 4.1.b and figure 4.1.c show two different scenarios. When the previously estimated channel transfer function is accurate, we expect a random distribution of the equalized received constellation points around the ideal constellation points due to the noise, as depicted in figure 4.1.b. In this case, the term $\left| avg\left\{ \vec{e} / d \right\} \right|$ tends to zero and a large value of γ is obtained, increasing the role of $\tilde{h}_{i-1,k}$. In figure 4.1.c, the scenario in which the previous estimation is not accurate enough is shown. In this case, the term $\left| avg\left\{ \vec{e} / d \right\} \right|$ increases which makes the value of γ decrease. This consequently boosts the role of $\hat{h}_{i,k}$ in equation 4.8 in order to track the drifts.

The adaptive weighting parameter, γ, can also be used in a different way: it can be first transformed by a function $f(.)$ and then applied to equation 4.8. $f(.)$ can be any non-decreasing function, such as a sigmoid nonlinear function, which has been used for reliability factors of weighted decision feedback equalizers (DFE) in [103]. Since our main focus in this work is the concept of the decision-directed equalizer, and for the sake of simplicity, we use the identity function as $f(.)$.

As mentioned earlier, DDPE operates similar to AWCE, with the only difference being that the phase noise estimation is solely based on the decision-directed estimation. For that reason, to derive the subcarrier-specific equalized complex value symbol, $\hat{S}_{i,k}$, no data-aided phase noise estimation is used. For the case of DDPE, equation 4.4 can be rewritten as

$$\hat{S}_{i,k} = \frac{r_{i,k}}{\tilde{h}_{i-1,k}} \tag{4.10}.$$

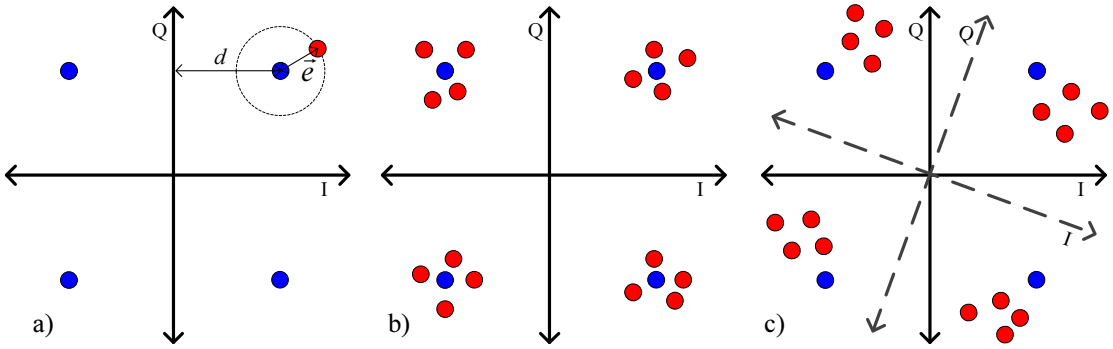

Figure 4-1: Error-vector of one equalized received constellation point (a). The scenarios of accurate (b) and inaccurate (c) equalization due to the drift. Blue points represent the ideal constellation points. Red points illustrate the constellation points of one received OFDM symbol after equalization.

The remaining processes of DDPE are the same as AWCE. Presuming that the decision for $\hat{S}_{i,k}$ is correct, by applying equation 4.6, the resulting $\hat{h}_{i,k}$ is the updated version of $\tilde{h}_{i-1,k}$ and includes information on the optical channel drifts, particularly the laser phase noise in the time interval of the i^{th} received OFDM symbol. In this case, the estimation of laser phase noise, provided by equation 4.10, is purely decision-directed since no pilot subcarrier or RF-pilot was employed.

4.3.2. Simulation of the Performance of AWCE

Figure 4.2 depicts the setup of the simulated transmission link for a conventional CO-OFDM system based on electrical intermediate frequency (IF) up-/down-conversion and RF-pilot enabled phase noise estimation. The simulations are performed in MATLAB. The

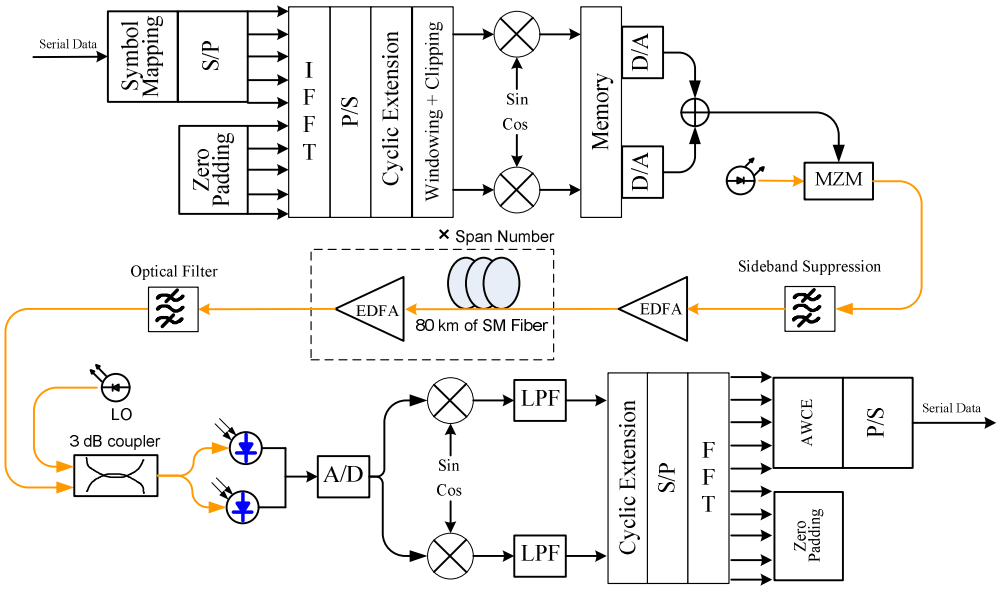

Figure 4-2: Simulation setup.

principle of operation of CO-OFDM systems was explained in chapter 2. The original data at 40 Gb/s are first divided and mapped onto 1024 frequency subcarriers with QPSK modulation and subsequently transferred to the time domain using an IFFT of size 2048 with zeros occupying the unused portion. A cyclic prefix of length 350 is used to accommodate the fibre dispersion. Following this procedure, an electrical up-conversion stage shifts the OFDM signal to the 10-30 GHz band. The OFDM signal is electrically up-converted using an electrical IF carrier to up-convert the signal upon applying a complex electrical I/Q mixer. To insert the RF-pilot in the middle of the OFDM signal for phase noise estimation, we set the first OFDM channel to 0 and apply a small DC offset in the I and Q tributaries of the I/Q-mixer [37,100]. The DC offset will be up-converted with the OFDM signal and, as a result, a small RF-pilot will be present at the IF frequency. In figure 4.3, the electrical spectrum after up-conversion is shown; additionally, the presence of the RF-pilot can be clearly distinguished. The ratio between RF-pilot power and the power of all subcarriers is referred to as the pilot-to-signal-ratio (PSR). The resulting up-converted electrical OFDM signal is then electro-optically converted using a chirp-less Mach-Zehnder modulator (MZM). The transmitted signal is then optically filtered to suppress one of the sidebands

for supporting single-sideband (SSB) modulation. The transmission link consists of 25 un-compensated single mode fibre (SMF) spans with a dispersion parameter of 17 ps/nm.km, a nonlinear coefficient of 1.5 $W^{-1}.km^{-1}$, and a loss parameter of 0.2 dB/km. Spans are 80 km long and separated by erbium-doped-fibre-amplifiers (EDFAs) with a noise figure of 6 dB. The optical launch power to each fibre span is set at -4 dBm. The Split-step Fourier method is used to simulate the optical fibre medium. At the optical receiver, an optical filter with a bandwidth of 0.4 nm is applied to reject out-of-band ASE noise. The receiver is based on the heterodyne CO-OFDM scenario, in which the optical OFDM signal is converted into a real valued electrical OFDM signal at an IF. Using a subsequent electrical I/Q demodulator, the real and imaginary components are available in the baseband.

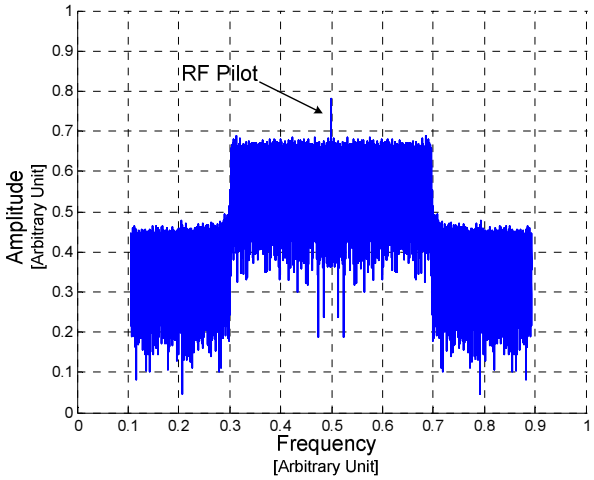

Figure 4-3: A typical OFDM spectrum with RF-pilot enabled phase noise compensation. PSR is the ratio between RF-pilot power and the power of all subcarriers.

To mimic the continuous time characteristics of the optical channel, 50 different random sets of time-domain realizations of laser phase noise and PMD have been simulated. The laser phase noise is modeled using the well-established model described in [104]. This model assumes that the laser phase undergoes a random walk where the steps are individual spontaneous emission events which both instantaneously and randomly change the phase by a small amount. We considered a laser linewidth of 100 kHz for both transmitter and receiver sides. The dynamic response of the PMD is simulated using the dynamic wave

plate model proposed in [105]. This model generates a continuous PMD variation and correlation between adjacent time samples. The PMD coefficient of the fibre medium was set to 0.5 ps/√km and 1600 wave plates were taken into account. The simulation parameters were adjusted as guided in [105] to emulate a fast PMD speed in the range of microseconds to milliseconds.

As discussed in subsection 4.3.1, AWCE is capable of improving the performance of phase noise compensation. Figure 4.4 compares the bit-error-rate (BER) performance of AWCE versus PSR, with and without decision-directed phase noise compensation for two different received OSNR values of 13 dB and 16 dB. In this simulation, each OFDM block consists of 2 training symbols and 62 data symbols (an overhead of 3% due to PS insertion). In both received OSNR cases, for lower values of PSR, decision-directed phase noise compensation slightly improves the performance; however, as PSR increases, it significantly increases the precision of phase noise estimation and better BER results are obtained. This is due to the fact that decision-directed phase noise compensation relies on both correct decision making and a fairly good RF-pilot enabled phase noise estimation to achieve a pronounced improvement. As one can see in figure 4.4, to achieve the forward-error-correction (FEC) threshold, the commonly-reported BER value of 10^{-3}, AWCE with decision-directed phase noise compensation requires 1 and 2.2 dB less RF-pilot power when compared to AWCE without decision-directed phase noise compensation for received OSNR values of 16 and 13 dB, respectively, showing greater improvement for the noisier scenario.

In figure 4.5, we investigate the capability of AWCE on PS overhead reduction. For this test, we fixed the PSR at -10 dB for all simulations. As one can see for the case of CE, when we reduce the PS overhead from 3% (blue curve) to 0.3% (red curve), the signal quality degrades. This degradation introduces an OSNR penalty of 1.2 dB at the FEC threshold. However, when we apply AWCE without decision-directed phase noise compensation to the signal with PS overhead of 0.3%, almost the same performance as CE with PS overhead of 3% can be achieved (see the black curve in figure 4.5). This demonstrates that AWCE can significantly reduce the PS overhead, here by a factor of 10, while providing the same

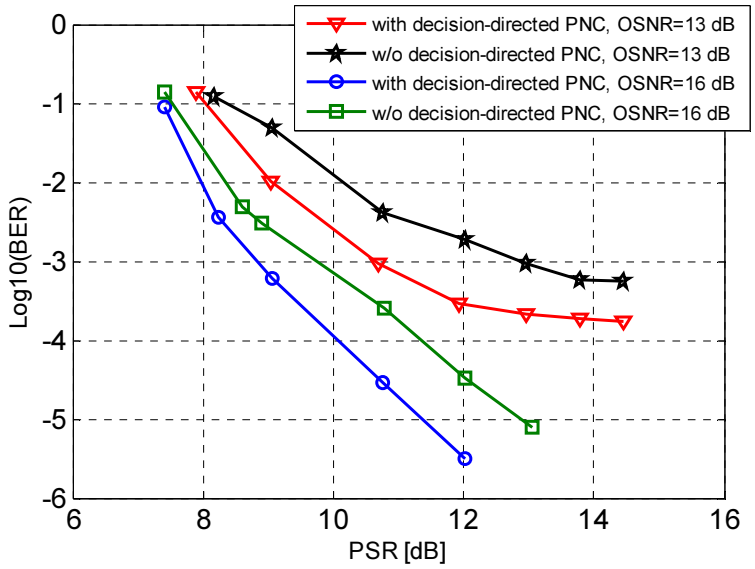

Figure 4-4: Simulation results of the BER performance of the decision-directed phase noise compensation (PNC) for two different received OSNR values of 13 and 16 dB.

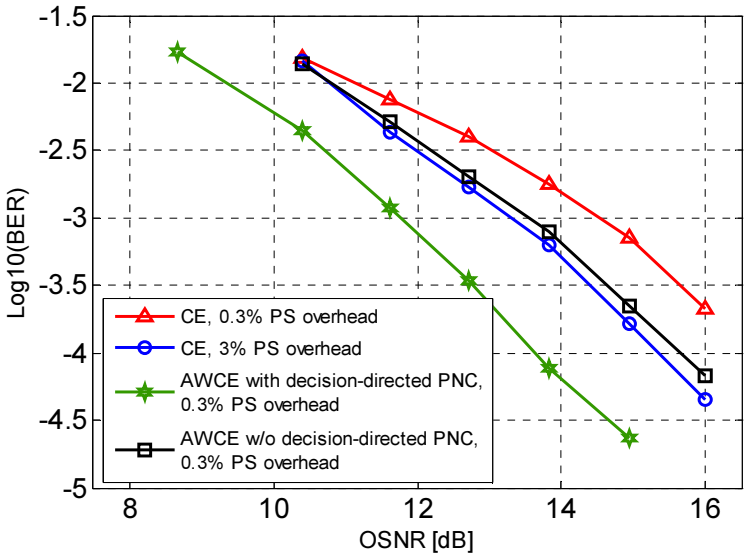

Figure 4-5: The comparison between the BER performance of CE with the PS overhead of 3% and 0.3% and AWCE with the PS overhead of 0.3%.

signal quality. This improvement is due to the fact that AWCE updates the equalization parameters on a symbol-by-symbol basis and can track slight drifts in the optical channel. Moreover, AWCE with decision-directed phase noise compensation can further improve

the signal quality. As seen with the green curve in figure 4.5, to achieve the BER of 10^{-3}, AWCE with data-aided PNC and PS overhead of 0.3% requires 2.9 and 1.8 dB less OSNR than CE with PS overhead of 0.3% and 3%, respectively. This is due to the fact that AWCE not only tracks the drifts, but also provides enhanced phase noise estimation and, consequently, more accurate compensation.

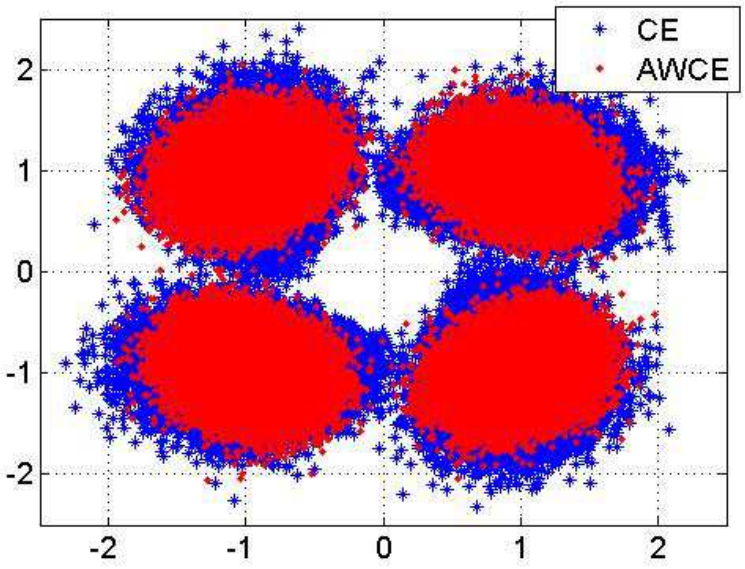

Figure 4-6: The comparison between the received constellations after 2000 km transmission, equalized by CE and AWCE. The PS overhead is 0.3% for both cases.

Figure 4.6 compares the received constellation of QPSK signal after equalization by CE and AWCE with decision-directed phase noise compensation. The overhead of PS insertion, the received OSNR, and the PSR for both cases are set to 0.3%, 16 dB, and -10 dB, respectively. It can be clearly observed that AWCE provides better equalization and, subsequently, separated constellation points.

4.3.3. Simulation of the Performance of DDPE

Figure 4.7 depicts the setup of the simulated transmission link for the conventional CO-OFDM system and direct optical up-/down-conversion. Simulations are performed in MATLAB. The principle of operation of CO-OFDM systems was explained in chapter 2.

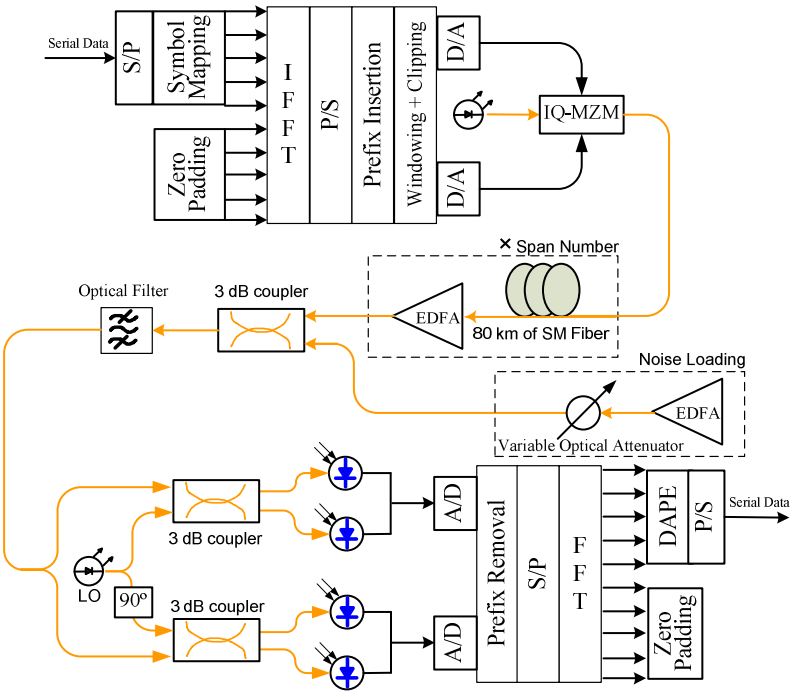

Figure 4-7: Simulation setup.

The original data at 40 Gb/s are first divided and mapped onto 1024 frequency subcarriers with QPSK modulation format and subsequently transferred to the time domain using an IFFT of size 2048 with zeros occupying the unused portion. A cyclic prefix of length 350 is used to accommodate dispersion. The resulting electrical OFDM data signal is then electro-optically converted using an I/Q Mach-Zehnder modulator (I/Q-MZM). The optical transmission link consists of 25 uncompensated SMF spans with a dispersion parameter of 17 ps/nm.km, a nonlinear coefficient of 1.5 $W^{-1}.km^{-1}$, a PMD coefficient of 0.5 ps/√km, and a loss parameter of 0.2 dB/km. Spans are 80 km long and separated by erbium doped fibre amplifiers (EDFAs) with a noise figure of 6 dB. The Split-step Fourier method is used to simulate the optical fibre medium. The laser phase noise is modeled as described in subsection 4.3.1. For each simulation point, 100 different random sets of time-domain realizations of laser phase noise have been simulated to mimic the continuous time characteristics of the optical channel. At the optical receiver, an optical filter with a bandwidth of 0.4 nm is applied to reject the out-of-band ASE noise. The receiver is based on the intradyne CO-OFDM scenario, in which the LO wavelength is close to the transmitter wavelength. The

OFDM signal then beats with the LO signal in an optical 90° hybrid to obtain the I and Q components of the signal. In this study, each OFDM block consists of 2 pilot and 62 data symbols, resulting in 3% of PS overhead.

In figure 4.8, an example of the received constellation points for the cases of (a) no phase noise compensation, and (b) phase noise compensation using DDPE, are shown. Lasers with a linewidth of 30 kHz are employed at both the transmitter and receiver sides and the launch power to each fibre span is set at -4 dBm. As one can see, when no phase noise compensation is applied the rotation of constellation points due to phase noise results in a poor separation of the constellation points; however, by using DDPE, all constellation points can be perfectly separated. This illustrates that DDPE is capable of compensating for the effect of laser phase noise.

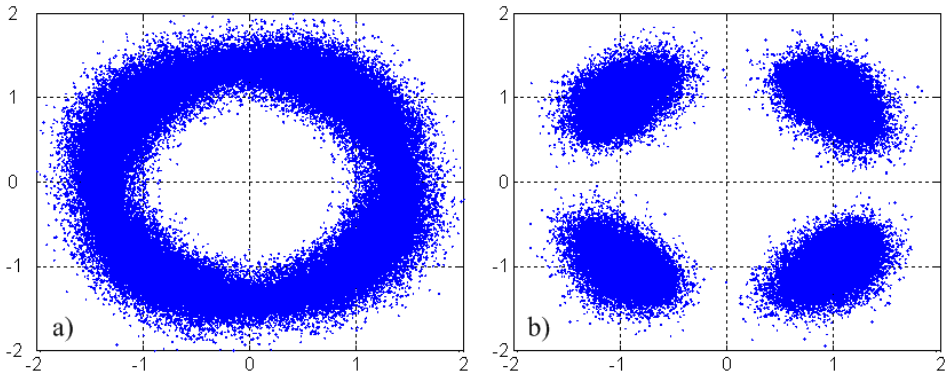

Figure 4-8: An example of received constellation points at 40 Gb/s after 2000 km transmission using laser linewidth of 30 kHz (a) without any phase noise compensation (b) with zero-overhead phase noise compensation based on DDPE.

To characterize the DDPE performance, we investigate the BER of the received signal versus the received OSNR for different laser linewidth values and compare it to the performance of CE, including a PSC overhead of 5%, at the same raw bit rate. For this study, we set the fibre launch power to -4 dBm and consider an identical linewidth for both lasers at the transmitter and receiver sides. As seen in figure 4.9, DDPE provides better performance than CE does for laser linewidths of 20 kHz, 40 kHz, and 60 kHz when the received OSNR is higher than 12 dB. This improvement in the signal quality is due to the fact that

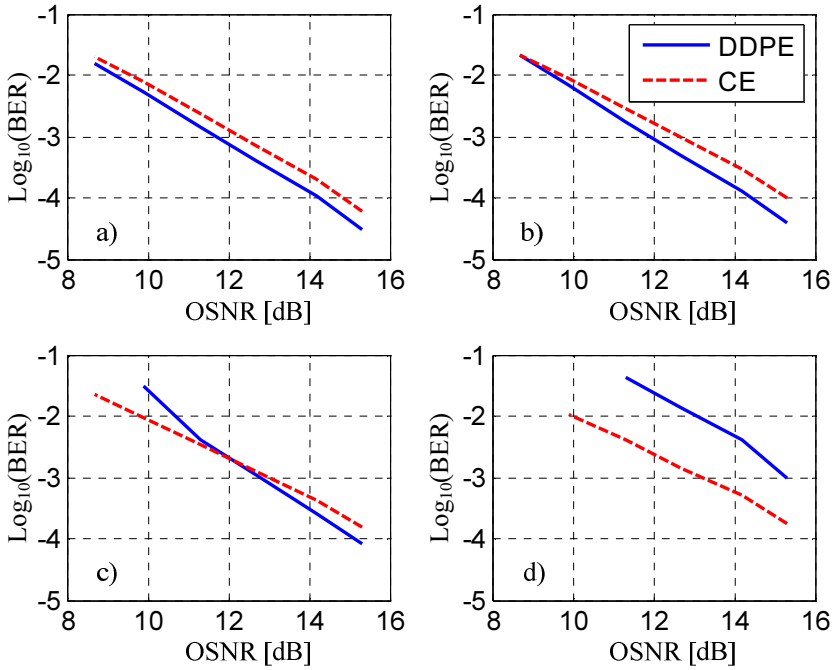

Figure 4-9: Simulation results of the BER performance of DDPE, blue solid curves, and CE with 5% PSC overhead, red dashed curves, for laser linewidths of (a) 20 kHz, (b) 40 kHz, (c) 60 kHz and (d) 80 kHz.

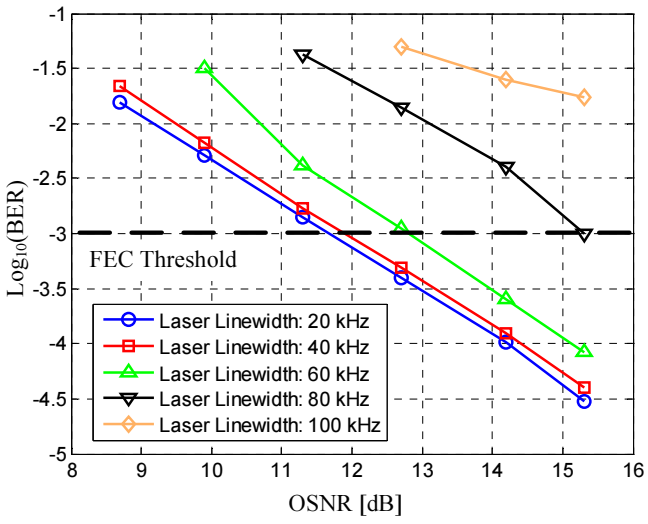

Figure 4-10: Simulation results of the BER Performance of DDPE for different laser linewidth values.

the recursive filtering of equation 4.8 suppresses the effect of ASE noise on the estimated channel transfer factor, resulting in more accurate equalization. For the case of laser

linewidth of 80 kHz, as seen in figure 4.9(d), the DDPE performance is severely compromised; an OSNR penalty of 2 dB is required to achieve the BER of 10^{-3}. This is due to the pronounced effect of error propagation in comparison to a pure decision-directed equalizer, i.e., DDPE does not perform as reliably as a data-aided method such as CE. Figure 4.10 compares the BER performance of DDPE for different laser linewidth values. As we expected, DDPE cannot provide adequate phase noise compensation due to the error propagation in relatively higher phase noise scenarios, specifically, for laser linewidths of 80 kHz and 100 kHz. However, for relatively low phase noise scenarios, it provides a good equalization and the FEC threshold of 10^{-3} is achieved at OSNR values of 11.6 dB, 11.9 dB, and 12.7 dB for laser linewidth values of 20 kHz, 40 kHz, and 60 kHz, respectively. The slight OSNR penalty between the performance of 20 kHz, 40 kHz, and 60 kHz scenarios is attributed to the inter-carrier interference (ICI) originating from the cross-leakage between subcarriers due to the phase noise, as described in detail in [7,69]. Similarly, due to the cross-leakage between subcarriers, an OFDM symbol with relatively shorter duration shows better performance against phase noise. Therefore, by increasing the number of filled subcarriers or equivalently increasing the oversampling ratio, slightly improved performance is expected.

Since fibre nonlinearities are one of the main impairments in CO-OFDM transmission systems, we investigate the DDPE performance versus fibre launch power to assess the behaviour of our proposed compensation technique in the presence of strong nonlinearity of the fibre. Figure 4.11 compares the BER performance of DDPE and CE versus fibre launch power at received OSNR values of 13 dB and 15.3 dB. In this study, the laser linewidth is set at 60 kHz for all scenarios. As seen in figure 4.11, although both equalizers suffer from strong nonlinearity, and the signal quality significantly degrades as the launch power increases, DDPE shows slightly higher sensitivity to nonlinearity, as can be observed for a launch power greater than -4 dBm. However, its performance is similar, or even better, than CE when the launch power is less than -4 dBm. To characterize the behaviour of both DDPE and CE in conjunction with the nonlinearity compensation schemes, we simulate the same scenario in the presence of the digital back-propagation (BP) algorithm [106]. In our study, the BP algorithm employs two steps per fibre span. As we see in figure 4.11, in the

presence of the BP compensation scheme, DDPE performs slightly better than CE and can support the error-free threshold of 10^{-3} for launch powers up to 0 dBm, for both received OSNR values of 13 dB and 15.3 dB.

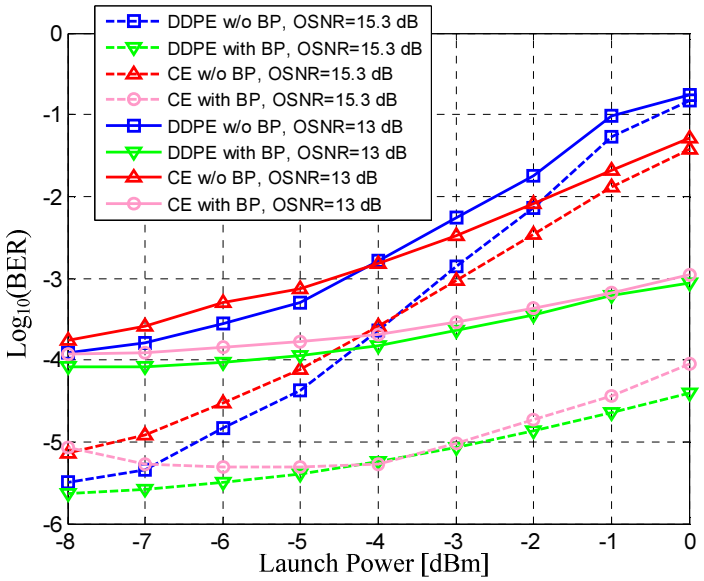

Figure 4-11: Simulation results of the BER performance of DDPE and CE versus launch power with and without the BP nonlinearity compensation scheme at received OSNR values of 13 dB and 15.3 dB. The linewidth of the lasers at both transmitter and receiver sides is set to 60 kHz.

4.4. Adaptive Decision-Directed Channel Equalizer in Polarization-Multiplexed CO-OFDM Systems

In this section, we adopt and extend the same approach of AWCE and DDPE for polarization-multiplexed CO-OFDM systems. We name this equalizer as an adaptive decision-directed channel equalizer (ADDCE). Similar to AWCE and DDPE, after an initial decision making stage, the ADDCE retrieves an estimation of the common-phase-error (CPE) value for the time interval of one OFDM symbol by extracting and averaging the phase drift of all OFDM sub-channels, demonstrating zero-overhead phase noise compensation. It also updates the channel transfer matrix, initially acquired using PSs, on a symbol-by-symbol basis

and enables the equalizer to increase the periodicity of the PSs, consequently reducing the PS overhead [35].

We study the performance of the ADDCE with both numerical simulations and experimental data. The experimental results at 28 GBaud using both quadrature-phase-shift-keying (QPSK) and 16-quadrature-amplitude-modulation (16-QAM) formats confirm not only the feasibility of the zero-overhead phase noise compensation but, due to a more accurate channel estimation, the superior bit-error-rate (BER) performance of the ADDCE versus a conventional equalizer (CE). At a FEC threshold of 3.8×10^{-3}, transmission distances of 5500 km and 400 km are achieved for the case of QPSK and 16-QAM RGI-DP-CO-OFDM, respectively, using zero-overhead phase compensation and a cumulative overhead of less than 2.6%. We also study the effect of both the synchronization timing error and the residual dispersion on the ADDCE and the CE, and demonstrate the superior performance of the ADDCE.

It is notable that since the ADDCE operates on a symbol-by-symbol basis, and considering the fact that OFDM symbol rates can be much lower than the actual transmitted bit-rate, implementing the ADDCE does not necessarily require both high-speed and high power consuming electronics. A brief analysis of the computational complexity of this scheme in terms of the number of required complex multiplications is provided, showing a complexity of only 28%.

4.4.1. The Concept of ADDCE

Assume that *i* and *k* denote the indexes for the received symbol (time index) and the OFDM subcarrier (frequency index), respectively. Additionally, assume that *X* and *Y* represent the two optical polarizations. In RGI-DP-CO-OFDM systems, the subcarrier-specific received complex value symbol, vector $\vec{r}_{i,k}$, is first sent to a static overlapped frequency-domain equalizer (OFDE) to compensate for the effect of CD. The resulting vector, $\vec{\tilde{r}}_{i,k}$, is then equalized by applying the zero-forcing technique based on the previously estimated transfer matrix, $\widetilde{H}_{i-1,k}$, that is taken as a prediction of the current channel transfer matrix:

$$\begin{bmatrix} \hat{S}_{i,k}^{X} \\ \hat{S}_{i,k}^{Y} \end{bmatrix} = \begin{bmatrix} \widetilde{H}_{i-1,k}^{XX} & \widetilde{H}_{i-1,k}^{XY} \\ \widetilde{H}_{i-1,k}^{YX} & \widetilde{H}_{i-1,k}^{YY} \end{bmatrix}^{-1} \times \begin{bmatrix} \hat{r}_{i,k}^{X} \\ \hat{r}_{i,k}^{Y} \end{bmatrix} \tag{4.11},$$

where vector $\vec{\hat{S}}_{i,k}$ is the subcarrier-specific equalized complex value symbol. Matrix $\widetilde{H}_{0,k}$ is initially derived using the PSs that are inserted at the beginning of each block of OFDM data symbols as described in [80]. To partially mitigate the effect of noise, a low-pass filter (LPF) is applied to $\widetilde{H}_{0,k}$. Vector $\vec{\hat{S}}_{i,k}$ is then detected by the demodulator of the first decision making stage as

$$\vec{\bar{S}}_{i,k} = Decision\left\langle \vec{\hat{S}}_{i,k} \right\rangle \tag{4.12}.$$

Presuming that the decision vector $\vec{\bar{S}}_{i,k}$ was correct, and with previous knowledge of the received symbol, vector $\vec{\hat{r}}_{i,k}$, we can estimate the average phase drift due to the laser phase noise in the time interval of the i^{th} received OFDM symbol as

$$\Delta\varphi_i = \frac{\left(\Delta\varphi_i^X + \Delta\varphi_i^Y\right)}{2} = \frac{\left(\sum_{q=1}^{N_{SC}} \left(\arg\left\{\hat{r}_{i,q}^X\right\} - \arg\left\{\bar{S}_{i,q}^X\right\}\right)\right) + \left(\sum_{q=1}^{N_{SC}} \left(\arg\left\{\hat{r}_{i,q}^Y\right\} - \arg\left\{\bar{S}_{i,q}^Y\right\}\right)\right)}{2 \times N_{SC}} \tag{4.13},$$

where N_{SC} is the total number of OFDM subcarriers. Equation 4.13 tries to extract the phase drift of the OFDM sub-channels in the time interval of the i^{th} received symbol assuming that the optical channel drift due to other impairments, such as CD and PMD, is negligible. This is a valid assumption since both CD and PMD variations are believed to be low-speed in comparison to the typical CO-OFDM symbol rate. Since the calculation of equation 4.13 is done after the decision making in equation 4.12, a fairly reliable initial equalization is necessary to prevent error propagation. Implementing this technique to retrieve and compensate for the phase noise requires that the amount of rotation does not result in incorrect initial decision making for the majority of the constellation points in every received symbol. As one can expect, the ADDCE performance for dense constellation formats is more sensitive to optical channel impairments. Therefore, for scenarios with relatively high laser phase noise and/or long symbol duration, this technique is not capable of proper phase noise compensation and might require the assistance of the PSCs or the RF-

pilot to avoid error propagation, as presented in [69,100]. Afterward, the equalized symbol is sent to the final decision making stage:

$$\vec{c}'_{i,k} = Decision\left\langle \vec{\hat{S}}_{i,k} \times e^{-j\Delta\varphi_i} \right\rangle \qquad (4.14),$$

where vector $\vec{c}'_{i,k}$ is the subcarrier-specific detected complex value vector.

In addition, by using equation 4.11 and knowing both the detected vector, $\vec{\tilde{S}}_{i,k}$, and the received vector after OFDE, $\vec{\hat{r}}_{i,k}$, the ideal channel transfer matrix can also be estimated. Despite the fact that the channel transfer matrix has four unknown arrays while equation 4.11 offers only two linear equations, it is possible to find the unknown arrays using the current and the previous symbol decisions to derive four sets of linear equations. However, to reduce the complexity, we propose a new way to alternately update just two unknown arrays per received vector. For instance, for received data vectors with even indexes ($\mathrm{mod}(i,2)=0$), we update both $\hat{H}_{i,k}^{XY}$ and $\hat{H}_{i,k}^{YX}$, only, by the common-phase-noise (CPE) value of the corresponding time interval as

$$\hat{H}_{i,k}^{XY} = \tilde{H}_{i-1,k}^{XY} \times e^{j\Delta\varphi_i} \qquad if\ \mathrm{mod}(i,2)=0 \qquad (4.15.a)$$

$$\hat{H}_{i,k}^{YX} = \tilde{H}_{i-1,k}^{YX} \times e^{j\Delta\varphi_i} \qquad if\ \mathrm{mod}(i,2)=0 \qquad (4.15.b).$$

Using equation 4.15.a and equation 4.15.b, we derive both $\hat{H}_{i,k}^{XX}$ and $\hat{H}_{i,k}^{YY}$ via equation 4.11 as follows:

$$\hat{H}_{i,k}^{XX} = \frac{\hat{r}_{i,k}^{X} - \tilde{H}_{i,k}^{XY} \times S_{i,k}^{Y}}{S_{i,k}^{X}} \qquad if\ \mathrm{mod}(i,2)=0 \qquad (4.15.c)$$

$$\hat{H}_{i,k}^{YY} = \frac{\hat{r}_{i,k}^{Y} - \tilde{H}_{i,k}^{YX} \times S_{i,k}^{X}}{S_{i,k}^{Y}} \qquad if\ \mathrm{mod}(i,2)=0 \qquad (4.15.d).$$

For data symbols with odd indexes ($\mathrm{mod}(i,2)=1$), we update both $\hat{H}_{i,k}^{XX}$ and $\hat{H}_{i,k}^{YY}$, only, by the common phase noise value of the corresponding time interval as

$$\hat{H}_{i,k}^{XX} = \tilde{H}_{i-1,k}^{XX} \times e^{j\Delta\varphi_i} \qquad if\ \mathrm{mod}(i,2)=1 \qquad (4.16.a)$$

$$\hat{H}_{i,k}^{YY} = \tilde{H}_{i-1,k}^{YY} \times e^{j\Delta\varphi_i} \qquad if\ \mathrm{mod}(i,2)=1 \qquad (4.16.b).$$

Using equation 4.16.a and 4.16.b, we derive the $\hat{H}_{i,k}^{XY}$ and $\hat{H}_{i,k}^{YX}$ via 4.11 as follows:

$$\hat{H}_{i,k}^{XY} = \frac{\hat{r}_{i,k}^{X} - \widetilde{H}_{i,k}^{XX} \times S_{i,k}^{X}}{S_{i,k}^{Y}} \qquad if \bmod(i,2) = 1 \tag{4.16.c}$$

$$\hat{H}_{i,k}^{YX} = \frac{\hat{r}_{i,k}^{Y} - \widetilde{H}_{i,k}^{YY} \times S_{i,k}^{Y}}{S_{i,k}^{X}} \qquad if \bmod(i,2) = 1 \tag{4.16.d).}$$

We refer to the resulting channel transfer matrix, $\hat{H}_{i,k}$, as a decision-directed channel transfer matrix. $\hat{H}_{i,k}$ corresponds to the time interval of the i^{th} received OFDM symbol and includes not only the common-phase-error (CPE) information of the laser phase noise process but also any drift in channel response. A low-pass filter (LPF) is applied to $\hat{H}_{i,k}$ to suppress the high-frequency noise. To update the channel transfer matrix for the next received symbol, we apply a simple recursive filtering procedure using both the previously estimated channel transfer factor, $\widetilde{H}_{i-1,k}$, and the ideal channel transfer factor, $\hat{H}_{i,k}$. The recursion is performed independently for each subcarrier and a time-domain correlation is implicitly utilized. No channel statistics, such as the correlation function or signal-to-noise ratio (SNR), are needed. The subcarrier-specific channel transfer factor for the i^{th} received symbol can then be updated as

$$\widetilde{H}_{i,k}^{XX} = (1-\gamma_i) \times \widetilde{H}_{i-1,k}^{XY} \times e^{j\Delta\varphi_i} + \gamma_i \times \hat{H}_{i,k}^{XX} \tag{4.17.a}$$

$$\widetilde{H}_{i,k}^{YY} = (1-\gamma_i) \times \widetilde{H}_{i-1,k}^{YY} \times e^{j\Delta\varphi_i} + \gamma_i \times \hat{H}_{i,k}^{YY} \tag{4.17.b}$$

$$\widetilde{H}_{i,k}^{XY} = (1-\gamma_i) \times \widetilde{H}_{i-1,k}^{XY} \times e^{j\Delta\varphi_i} + \gamma_i \times \hat{H}_{i,k}^{XY} \tag{4.17.c}$$

$$\widetilde{H}_{i,k}^{YX} = (1-\gamma_i) \times \widetilde{H}_{i-1,k}^{YX} \times e^{j\Delta\varphi_i} + \gamma_i \times \hat{H}_{i,k}^{YX} \tag{4.17.d),}$$

where γ is the weighting parameter and can take any value between 0 and 1. A small value of γ boosts the role of the previously estimated channel transfer matrix, $\widetilde{H}_{i-1,k}$. Conversely, a large value of γ increases the effect of the decision-directed channel transfer matrix, $\hat{H}_{i,k}$. γ controls the recursion and can either be a fixed or an adaptive value [34]. In this study, we choose a fixed γ value of 0.1.

4.4.2. Experimental Study of the Performance of ADDCE

In this subsection, we study the experimental performance of the ADDCE for both QPSK and 16-QAM RGI-DP-CO-OFDM transport systems. The experimental setup is shown in figure 4.12, and it is based on the setup and equipment introduced in chapter 3. In our investigation, we use off-line signal processing on the experimental data to further characterize the capabilities of the ADDCE and compare its performance with the CE. The CE is combined with two other commonly-reported compensation schemes: the maximum-likelihood (ML) phase noise compensation [24] and intra-symbol frequency-domain averaging (ISFA) [65], as reviewed in chapter 2.

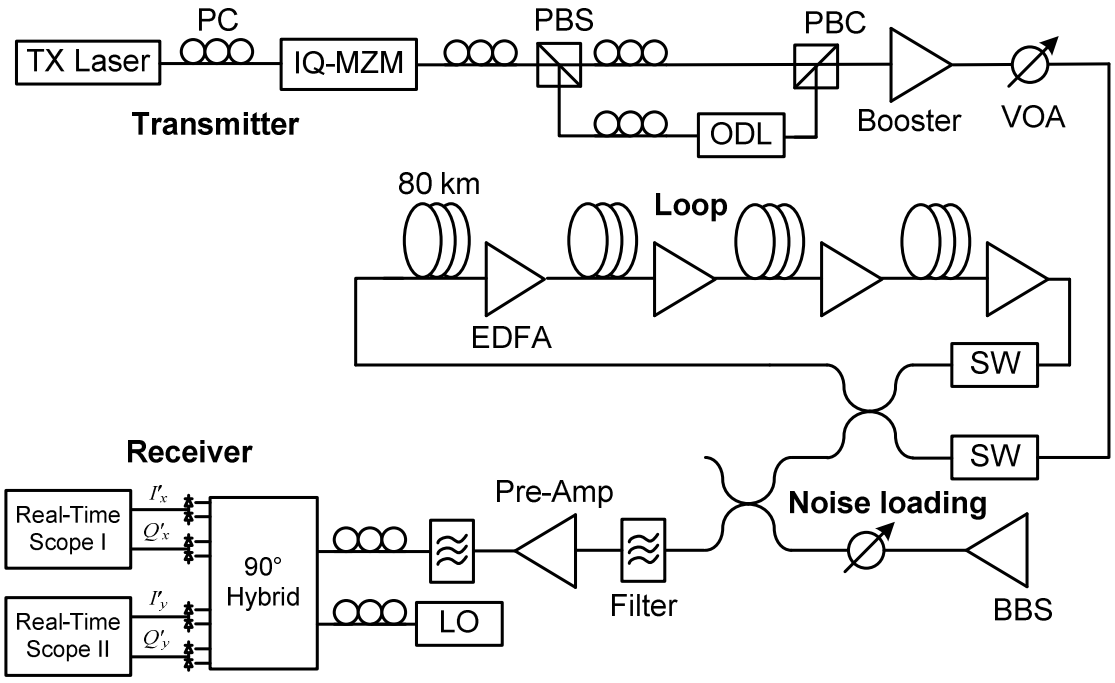

Figure 4-12: RGI-DP-CO-OFDM experimental setup.

The original binary pseudo-random bit sequence (PRBS) data, with a length of 2^{17}-1, is first divided and mapped onto 112 frequency subcarriers with QPSK (16-QAM) modulation format, and is subsequently transferred to the time-domain using an IFFT of size 128 with zeros occupying the unused remainder of the array, fixing an oversampling ratio of 1.14. In this RGI-DP-CO-OFDM system, a cyclic prefix of length 3 is employed, resulting

in 2.34% of CP overhead. The CE employs 4 pilot subcarriers which can be translated to 3.57% of PSC overhead; however, the ADDCE has no pilot subcarrier featuring the zero-overhead phase noise compensation. The CE and the ADDCE use 2 pilot symbols (PSs) as the training sequence for every 100 and 1000 data symbols, equivalently 2% and 0.2% of TS overhead, respectively. This results in a cumulative overhead of about 8% (2.34% + 3.57% + 2%) and approximately 2.6% (2.34% + 0% + 0.2%) for the CE and the ADDCE, respectively. The in-phase (I) and quadrature (Q) parts of the resulting digital OFDM signal are then loaded separately on two field-programmable gate arrays (FPGAs) to electrically generate the electrical I and Q via two digital to analog convertors (DACs), operating at 32 GS/s. Using the oversampling ratio of 1.14, the analog electrical I and Q signals at 28 Gbaud OFDM are generated and then fed into an I/Q Mach-Zehnder modulator (I/Q-MZM). After the I/Q-MZM, a dual polarization emulator is used to imitate a dual-polarization multiplexed transmitter which results in 112-Gb/s and 224-Gb/s for QPSK and 16-QAM RGI-DP-CO-OFDM signals, respectively. The optical transmission link consists of a 4-span of optical recirculating loops with uncompensated SMF with a dispersion parameter of 17 ps/nm.km, a nonlinear coefficient of 1.2 $W^{-1}.km^{-1}$, and a loss parameter of 0.18 dB/km. Spans are 80 km long and separated by erbium-doped-fibre-amplifiers (EDFAs) with a noise figure of 5-6 dB. At the optical receiver, two optical filters with bandwidths of 0.4 nm and 0.8 nm are applied before and after the preamplifier, respectively, to reject the out-of-band ASE noise. The receiver is based on the intradyne scenario in which the received signal beats with the optical LO signal in an optical polarization-diversity 90° hybrid to obtain the signal I and Q components. The LO is tuned to operate within the range of approximately tens of MHz of the received signal's center frequency. The four pairs of balanced outputs from the hybrid are then detected by four balanced photodetectors and then electrically sampled and asynchronously digitized at 80 GS/s using two commercial 4-channel real-time oscilloscopes equipped with analog-to-digital converters (ADCs) characterized by 33 GHz of analog bandwidth, a nominal resolution of 8-bits, and a frequency-dependent effective number of bits (ENoB) between 4 and 5. The four recorded signals are then transferred to the PC for off-line processing. In our experiments for this study, both the

transmitter laser and the LO are commercial external-cavity-lasers (ECLs) with a nominal linewidth of 100 kHz.

After transferring the samples from the real-time oscilloscopes to a processing machine, a computer for example, off-line processing would be applied to recover the signal. However, in a laboratory prototype it is not uncommon to observe timing mismatches between the optical and RF paths, such that the resulting sampled signals are not time-aligned. Digital signal de-skewing compensates for the path length mismatches between the sampled signals, synchronizing them with respect to one another. The timing mismatch between the sampled signal paths may be measured by cross correlating the sampled signals in the time-domain allowing the de-skew algorithm to compensate for these delays. Since, generally, the timing delays do not correspond to an integer number of samples, we may presume that the delays consist of a base point delay followed by a fractional delay. The base point delay is relatively straight forward to compensate, as it is simply a delayed version of the signal. In order to delay by a fraction of a sample period, interpolation is required.

To further characterize the capabilities of the ADDCE, we compare the performance of the ADDCE with the CE combined with the maximum-likelihood (ML) phase noise compensation and the intra-symbol frequency-domain averaging (ISFA). Throughout this study, optimal ISFA parameters of 9 and 5 are adopted for the case of QPSK and 16-QAM formats, respectively.

4.4.2.1. Study of the Transmission Reach

In figure 4.13 and figure 4.14, we compare the BER performance as a function of the transmission distance between the ADDCE and the CE combined with and without ML and ISFA algorithms for QPSK and 16-QAM RGI-DP-CO-OFDM, respectively. The optical launch power for the QPSK and 16-QAM cases were -2 dBm and -3 dBm, respectively. As described earlier, the cumulative overhead for the CE is approximately 8%. The ADDCE has a cumulative overhead of 2.6%, and features zero-overhead phase noise compensation. Based on the data presented in figures 4.13 and 4.14, the ADDCE performs better than any of the combined CEs. As expected, the CE combined with both the ML and ISFA algorithms has the closest performance to the ADDCE. At the forward-error-correction (FEC)

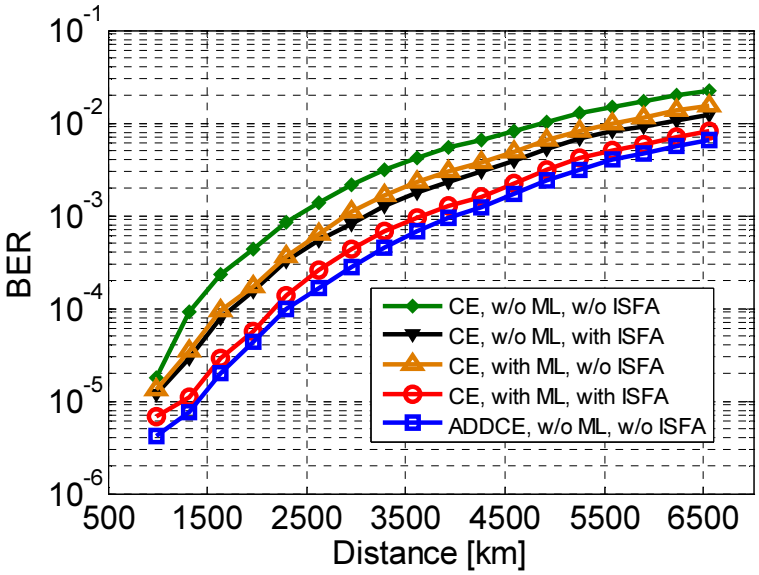

Figure 4-13: Experimental results of BER vs. distance for 28 GBaud QPSK RGI-DP-CO-OFDM.

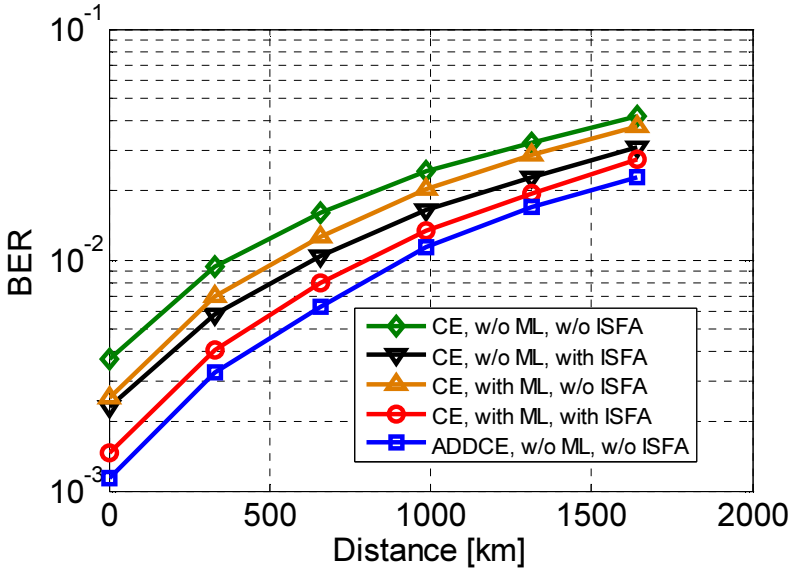

Figure 4-14: Experimental results of BER vs. distance for 28 GBaud 16-QAM RGI-DP-CO-OFDM.

threshold of 3.8×10^{-3}, the ADDCE achieves transmission distances of 5500 km and 400 km for QPSK and 16-QAM RGI-DP-CO-OFDM, respectively. This marks an 8% and 20% improvement in the transmission reach versus the CE with both the ML and ISFA algorithm for QPSK and 16-QAM RGI-DP-CO-OFDM, respectively. The significance of these experimental results is that the ADDCE demonstrates not only a significant overhead

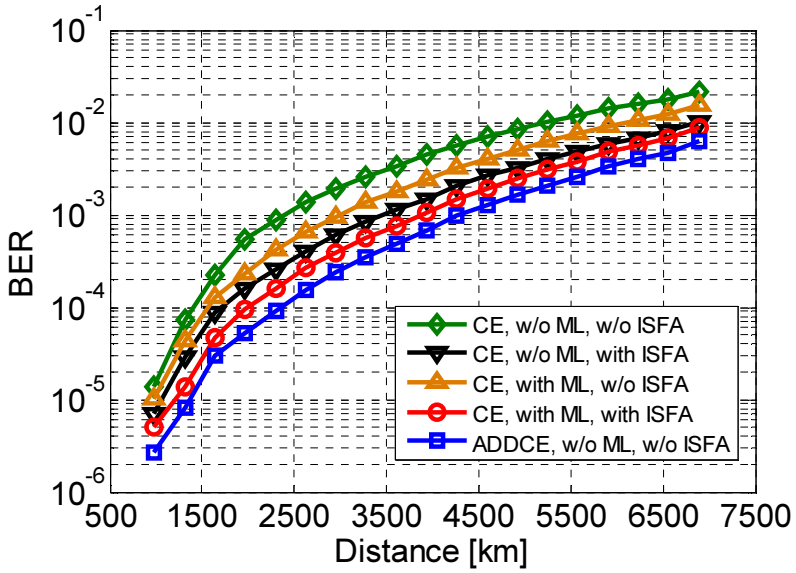

Figure 4-15: Simulation results of the BER vs. distance for 28 GBaud QPSK RGI-DP-CO-OFDM.

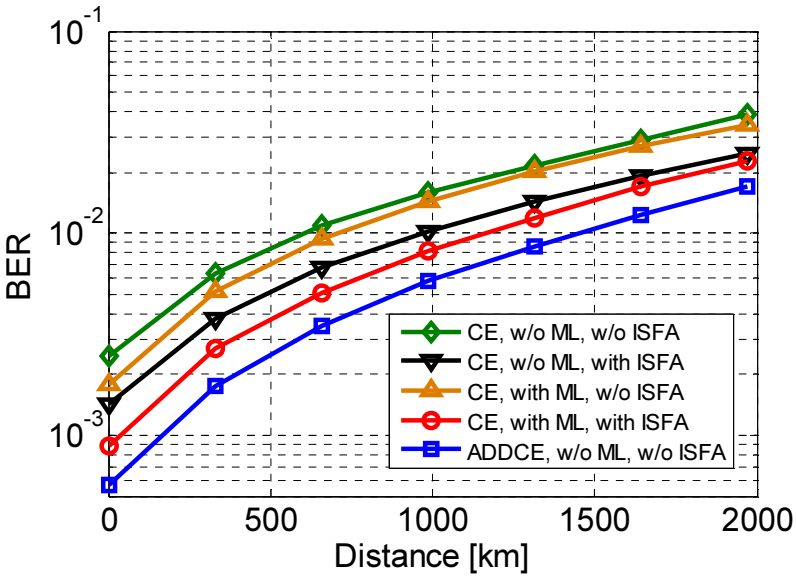

Figure 4-16: Simulation results of the BER vs. distance for 28 GBaud 16-QAM RGI-DP-CO-OFDM.

reduction from 8% to 2.6% but also an improvement in the transmission reach. As discussed in subsection 4.2.2, an overhead reduction can be translated to an increase in spectral efficiency or reduction of required OSNR of the optical link.

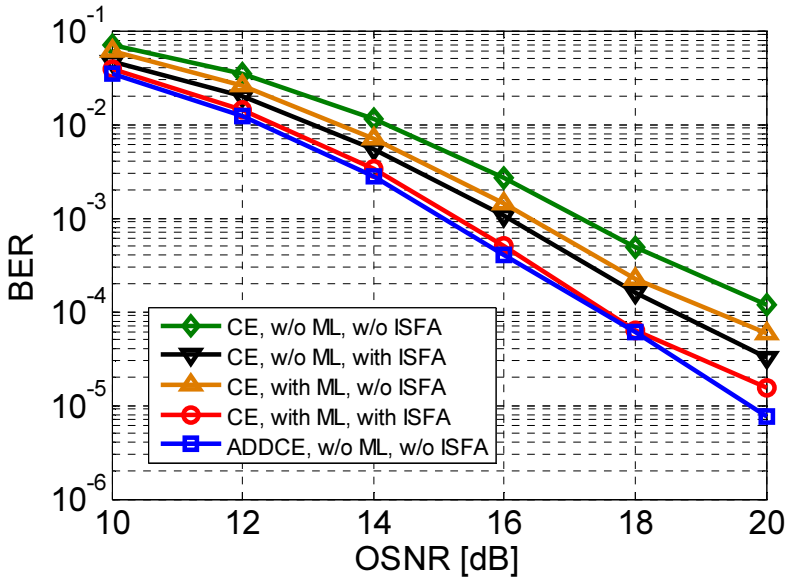

Figure 4-17: Experimental results of the BER vs. OSNR for 28 GBaud QPSK RGI-DP-CO-OFDM at optical B2B.

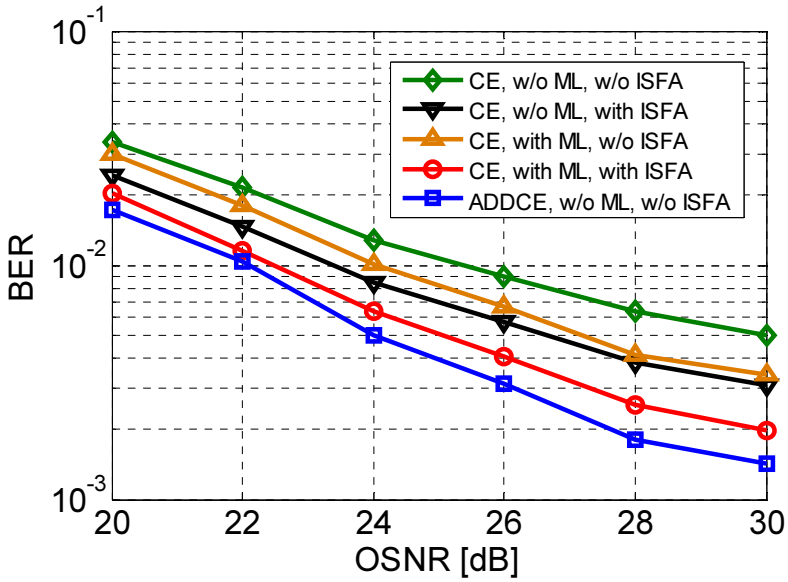

Figure 4-18: Experimental results of the BER vs. OSNR for 28 GBaud 16-QAM RGI-DP-CO-OFDM at optical B2B.

In order to observe the theoretical behaviour of the aforementioned algorithms, we conduct a numerical study, using the OptiSystem and MATLAB co-simulators, that models the experimental structure and parameters discussed in Section 4.4.2. Figure 4.15 and figure

4.16 show the simulation results for QPSK and 16-QAM RGI-DP-CO-OFDM, respectively. Despite differences in the simulated and experimental transmission reach, the overall trend of the performance of the various equalizers is similar for both experimental and simulation results. The differences between simulation and experiment can be attributed to several reasons including the noise of the real-time oscilloscope, the simplified transmitter and receiver models in OptiSystem simulator and the non-ideal DAC and ADC models considering the mismatch between the physical resolution in simulation and the ENoB in practice. The numerical simulations also suggest a longer transmission reach for the ADDCE and corroborate the feasibility of zero-overhead phase noise compensation for both QPSK and 16-QAM RGI-DP-CO-OFDM systems.

4.4.2.2. Study of the Effect of Different OSNR and Launch Power Values

In figure 4.17 and figure 4.18, we plot the BER versus OSNR for QPSK and 16-QAM RGI-DP-CO-OFDM, respectively. This measurement is performed in optical back-to-back (B2B) via a noise loading setup. We compare the performance of the ADDCE versus the CE combined with and without the ML and ISFA algorithms. As one can see, although the ADDCE has zero-overhead phase noise compensation, it outperforms the CE throughout the OSNR range of study for both QPSK and 16-QAM RGI-DP-CO-OFDM. The CE combined with both the ML and ISFA algorithms has the closest performance to the ADDCE. In figure 4.19 and figure 4.20, we characterize the performance of the equalizers for varying launch powers. The experiments are performed at a transmission distance of 3280 km and 328 km for QPSK and 16-QAM RGI-DP-CO-OFDM, respectively. The ADDCE provides superior performance and exhibits similar behaviour as the CE in noise- and nonlinear-limited regions.

4.4.2.3. Study of the Effect of the Synchronization Timing Error

In CO-OFDM, synchronization in both time and frequency are essential for DSP processes [107]. Synchronization timing errors can degrade the performance of the equalization algorithms and CO-OFDM systems are known to be sensitive to it [7,108]. In figure 4.21 and figure 4.22, we demonstrate the behaviour of the ADDCE and the CE, with and without

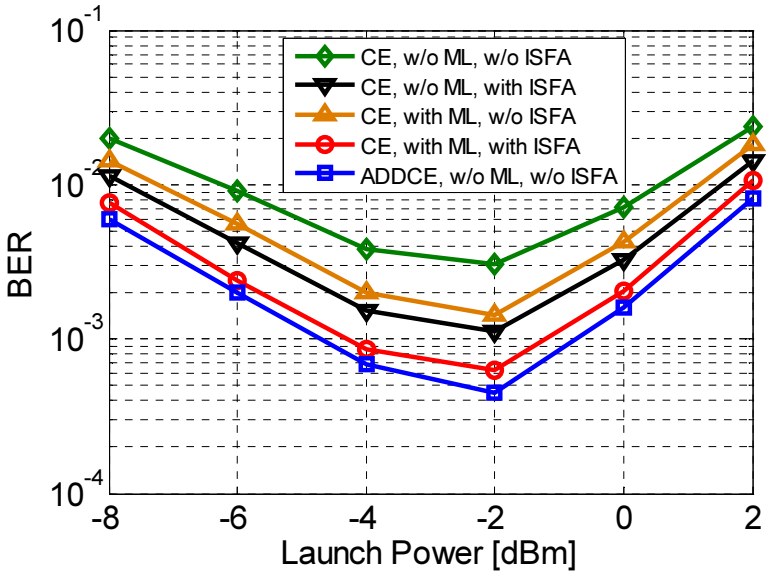

Figure 4-19: Experimental results of the BER vs. launch power for 28 GBaud QPSK RGI-DP-CO-OFDM at 3280 km.

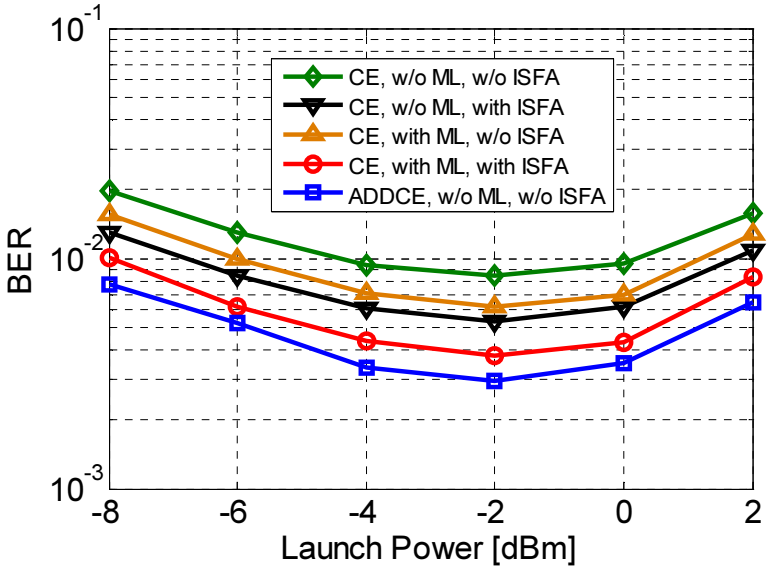

Figure 4-20: Experimental results of the BER vs. launch power for 28 GBaud 16-QAM RGI-DP-CO-OFDM at 328 km.

the ML and ISFA algorithms, in the presence of synchronization timing error for QPSK and 16-QAM RGI-DP-CO-OFDM, respectively. For the case of QPSK, a transmission distance of 3280 km with an optical launch power of -2 dBm is used. For the case of 16-QAM, the

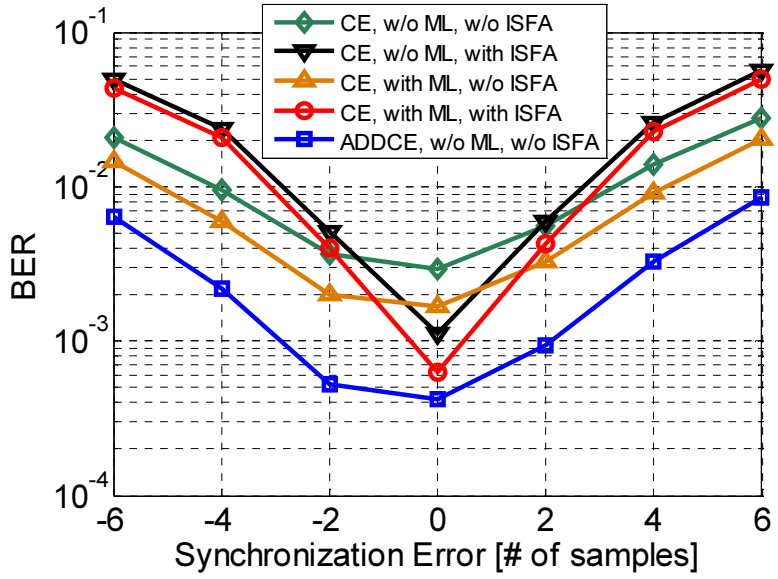

Figure 4-21: Experimental results of the BER vs. synchronization timing error for 28 GBaud QPSK RGI-DP-CO-OFDM at 3280 km.

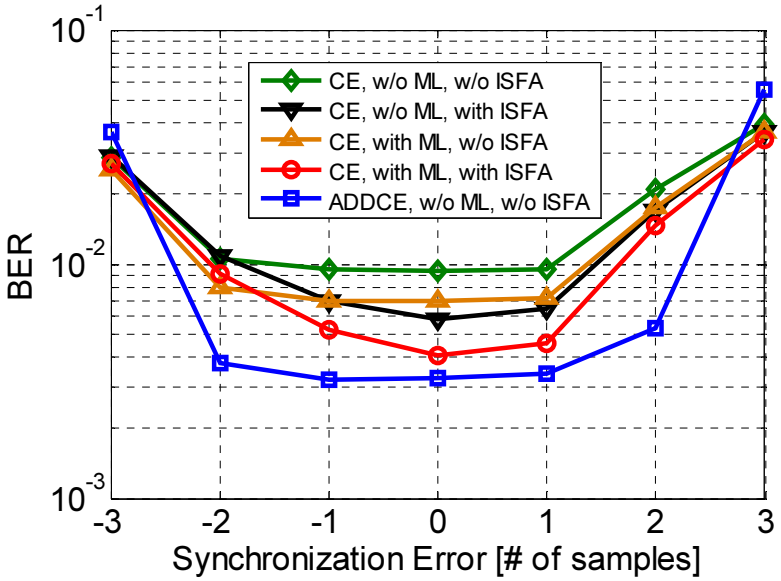

Figure 4-22: Experimental results of the BER vs. synchronization timing error for 28 GBaud 16-QAM RGI-DP-CO-OFDM at 328 km.

transmission distance and the optical launch power are set to 328 km and -3 dBm, respectively. As seen for both the QPSK and 16-QAM cases, the CE with the ISFA algorithm is more susceptible to the synchronization timing error. Additionally, the BER performance

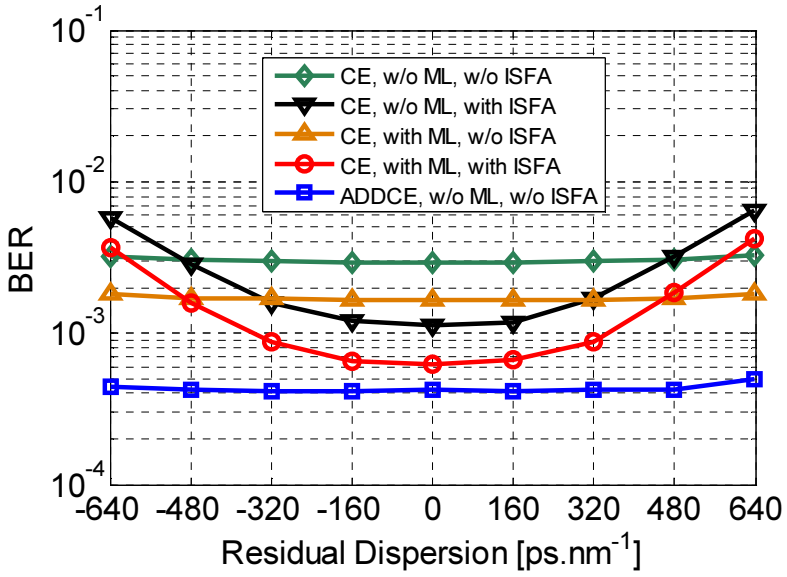

Figure 4-23: Experimental results of the BER vs. residual dispersion for 28 GBaud QPSK RGI-DP-CO-OFDM at 3280 km.

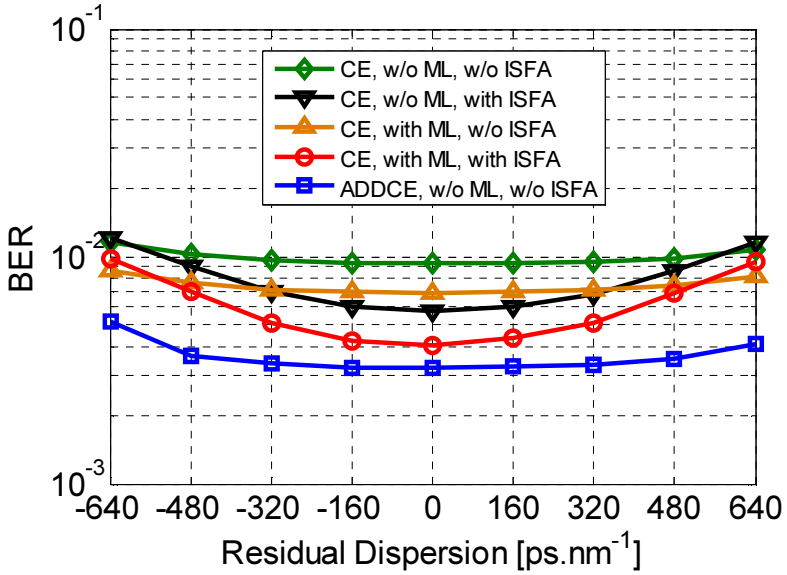

Figure 4-24: Experimental results of the BER vs. residual dispersion for 28 GBaud 16-QAM RGI-DP-CO-OFDM at 328 km.

degrades dramatically due to the effect of inter-symbol-interference (ISI) on the intra-symbol frequency-domain averaging. Moreover, since the optimal averaging parameter of the QPSK is larger than the 16-QAM, the degradation of the CE with ISFA is more pro-

nounced in QPSK. Therefore, the ADDCE demonstrates superior performance; it is more robust than the CE, with both the ML and ISFA algorithms, in the presence of synchronization timing error.

4.4.2.4. Study of the Effect of Residual Dispersion

RGI-CO-OFDM systems are capable of reducing the cyclic prefix (CP) to compensate for the ISI from the PMD and the transmitter bandwidth limitations [25].The nature of this approach is to compensate the CD by using a separate OFDE stage prior to the OFDM channel estimation and demodulation. However, an accurate knowledge of the CD is indispensable for an effective OFDE equalization. In figure 4.23 and figure 4.24, we compare the performance of the ADDCE and the CE in the presence of residual dispersion, due to inaccurate CD estimation and/or equalization in OFDE, for QPSK and 16-QAM RGI-DP-CO-OFDM, respectively. For the case of QPSK, the transmission distance and the optical launch power were 3280 km and -2 dBm, respectively. For the case of 16-QAM, the transmission distance and the optical launch power were 328 km and -3 dBm, respectively. The CEs with ISFA algorithms are vulnerable to residual CD and, consequently, the BER performance degrades dramatically. This is because different OFDM subcarriers now experience different phase rotations due to residual CD and the averaging between neighbouring OFDM sub-channels in the ISFA algorithm results in inaccurate channel transfer matrix estimation. Since the optimal ISFA averaging parameter for QPSK is larger than for 16-QAM, the degradation of the CE with ISFA is more pronounced in the case of QPSK. The ADDCE provides the same signal quality throughout the range of study, demonstrating its robustness to the effect of residual CD.

4.4.3. System Complexity

The complexity of an equalization algorithm directly affects the implementation cost of the transmission link due to hardware costs and power consumption [7,109,110]. In this section, we provide a brief comparison of the complexity of the ADDCE and the CE, without ML and ISFA, in terms of the required number of complex multiplications per bit, while taking into account both the FFT operations and the channel estimation and equaliza-

tion. In this study, multiplication and division are considered to have the same level of complexity. We assume that the channel is estimated every N_{CE} symbols, and that R_{CE} is the training symbol overhead. M denotes the number of bits per symbol. As shown in [83], the complexity of the CE in an RGI-DP-CO-OFDM system, C_{CE}, can be expressed as

$$C_{CE} = \frac{N_1\left(\log_2\left(N_1\right)+1\right)n'_{MC}}{\left(N_1 - N_{CD}+1\right)\log_2\left(M\right)} + \frac{n_{MC}\log_2\left(N_2\right)+2+\dfrac{5}{N_{CE}R_{CE}}}{\log_2\left(M\right)} \tag{4.18},$$

where N_1, N_2, n_{MP}, and n'_{MP} are the FFT lengths of the first static frequency-domain equalization (FDE), the FFT lengths of the second adaptive FDE, the OFDM oversampling ratio, and the modified FDE oversampling ratio, respectively. N_{CD} represents the minimum number of equalizer taps necessary to compensate for chromatic dispersion (CD) [83].

The ADDCE has similar complexity regarding channel estimation however, six more complex multiplications, per used subcarrier per polarization frame, are needed to implement equation 4.15 and equation 4.16. Furthermore, to derive equation 4.17, four more complex multiplications, per subcarrier per polarization frame, are required. To perform equalization, the ADDCE updates the channel transfer matrix inversion of equation 4.11 on a symbol-by-symbol basis. Therefore, the complexity of a 2×2 matrix inversion, with six complex multiplications per subcarrier per polarization frame, needs to be considered. Assuming that every frame transmits $2N_2\log_2\left(M\right)/n_{MC}$ bits, the total complexity for ADDCE, C_{ADDCE}, is given by

$$\begin{aligned} C_{ADDCE} &= \frac{N_1\left(\log_2\left(N_1\right)+1\right)n'_{MC}}{\left(N_1 - N_{CD}+1\right)\log_2\left(M\right)} + \frac{n_{MC}\log_2\left(N_2\right)+2+\dfrac{5}{N_{CE}R_{CE}}}{\log_2\left(M\right)} + \frac{6N_2/n_{MC}+4N_2/n_{MC}+6N_2/n_{MC}}{2N_2\log_2\left(M\right)/n_{MC}} \\ &= C_{CE} + \frac{8}{\log_2\left(M\right)} \end{aligned} \tag{4.19}.$$

For the specific case involving the parameters used in this experiment, we observe a complexity of 28% in regards to the number of complex multiplications required.

4.5. Conclusion

In this chapter, we explained the associated OSNR penalties with overhead in CO-OFDM systems. We reviewed our previous work, on overhead reduction using combined

data-aided and decision-directed estimations in single-polarization CO-OFDM. Furthermore, based on a numerical study we assessed their performance for single-polarization conventional CO-OFDM transport systems. We introduced the concept of an adaptive decision-directed channel equalizer (ADDPE) for dual-polarization CO-OFDM systems. We have summarized a series of experiments for 28 GBaud QPSK and 16-QAM reduced-guard-interval CO-OFDM (RGI-DP-CO-OFDM) transport systems. We compared the BER performance of the ADDCE with that of a conventional equalizer (CE) combined with maximum-likelihood (ML) phase noise compensation and intra-symbol frequency-domain averaging (ISFA) algorithms. By comparing the ADDCE and the CE, we have demonstrated that the ADDCE can perform as reliably as the CE combined with both ML and ISFA algorithms. Transmission distances of 5500 km and 400 km over the uncompensated, EDFA-amplified transmission link were achieved for 28 Gbaud QPSK and 16-QAM RGI-DP-CO-OFDM, respectively, whilst employing a cumulative overhead of less than 2.6%. Moreover, the ADDCE is more resilient than the CE to the effects of synchronization timing error and the residual dispersion. Finally, we characterized the computational complexity of this scheme in terms of the number of required complex multiplications, demonstrating a complexity of 28% for the specific case using the parameters chosen in this experiment.

We believe that the ADDCE's capacity in overhead reduction, improving the transmission reach, and resilience to both the synchronization timing error and the residual dispersion, makes it an attractive alternative equalization algorithm.

Chapter 5

Mitigation of the Inter-Carrier-Interference due to Laser Phase Noise

5.1. Overview

There are two primary detrimental effects of the laser phase noise on coherent optical orthogonal frequency division (CO-OFDM) systems: (i) common-phase-error (CPE) which can be compensated via pilot subcarriers (PSCs) and data-aided estimation, and (ii) inter-carrier-interference (ICI) which cannot be compensated using PSCs or conventional algorithms. The degradation effect of ICI on CO-OFDM signals is increased by using lasers with larger linewidths and/or longer symbol durations [7,10].

In this chapter, we introduce a low-complexity non-iterative phase noise induced inter-carrier interference (ICI) compensation algorithm for CO-OFDM systems and investigate its performance in an experimental reduced-guard-interval dual-polarization CO-OFDM (RGI-DP-CO-OFDM) transport system [36,40,111]. This interpolation-based ICI compensator estimates the time-domain phase noise samples using linear interpolation between the CPE estimates of consecutive OFDM symbols. We experimentally study the performance of this scheme for a 28 Gbaud QPSK RGI-DP-CO-OFDM using a low-cost distributed feedback (DFB) laser. In comparison with the conventional equalizer (CE), experimental results using a DFB laser with a linewidth of 2.6 MHz demonstrate a 24% and 13% improvement in transmission reach in the presence of weak and strong dispersion-enhanced-phase-noise (DEPN), respectively [40]. In addition, a brief analysis of the computational complexity of this scheme in terms of the number of required complex multiplications is provided; a complexity of 25% for the case of the parameters of our experiment is computed. This practical approach does not suffer from error propagation while enjoying low computational complexity.

This chapter is structured as follows; we briefly explain the effect of phase noise on the OFDM signal. Then, the principles of the interpolation-based ICI compensation, including the mathematical concept of the technique and its implementation, are described. We review our earlier simulation studies on the performance of the interpolation-based ICI compensator in conventional single-polarization CO-OFDM systems. We also present our RGI-DP-CO-OFDM experimental setup and, based on experimental data, investigate the concept of ICI compensation. Finally, the complexity of the proposed scheme is studied.

5.2. The Effect of Phase Noise on OFDM Systems

OFDM transmits high-speed serial information through multiple lower-speed sub-channels. This reduction in baud-rate leads to a decrease in inter-symbol interference (ISI) and, therefore, a simplified equalization process at the receiver. However, the performance of coherent transmission systems are known to suffer from laser phase noise and, in the case of CO-OFDM systems, the degradation is more pronounced due to the relatively

longer symbol duration with respect to single-carrier transmission schemes. This degradation limits the transmission reach and, consequently, makes the use of expensive, narrow linewidth laser sources inevitable.

As mentioned earlier, in CO-OFDM, laser phase noise degrades the received signal quality in two ways—common-phase-error (CPE), which is an identical phase rotation for all subcarriers, and inter-carrier interference (ICI), which is due to the loss of orthogonality between subcarriers. Laser phase noise compensation schemes may use RF-pilot enabled [37], pilot subcarrier (PSC) enabled [7,10], decision-directed, and maximum likelihood (ML) algorithms [7,38,112]. In the aforementioned algorithms, with the exception of the RF-pilot enabled algorithm, only the CPE can be mitigated. However, for relatively large laser linewidths, and/or longer symbol durations, the ICI degradation becomes pronounced and must be compensated for. In [113], the authors adopted an orthogonal basis expansion-based technique to suppress both CPE and ICI in CO-OFDM systems. In wireless systems, the effect of ICI on the performance of OFDM systems due to the local oscillator (LO) phase noise has been extensively investigated and several iterative algorithms have been previously proposed to jointly estimate both the data and the phase noise vector [114-116]. Nevertheless, since ICI mitigation requires de-convolving the phase noise spectral components from unknown data subcarriers, such iterative schemes suffer from high latency and hefty implementation complexity making them unsuitable for long-haul ultra high-speed optical transmission applications.

The effect of phase noise on OFDM samples in the time-domain is modeled as a multiplication, which is equivalently expressed as a convolution in the frequency-domain,

$$r_{i,k} = \sum_{q=0}^{N_{sc}-1} p_{i,\langle k-q \rangle} h_q c_{i,q} + w_{i,k} \tag{5.1},$$

where c, p, h, and r are the subcarrier-specific transmitted data symbol in frequency-domain, the phase noise spectral components, the subcarrier-specific channel frequency response and the subcarrier-specific received data symbol in frequency-domain, respectively. k and i denote the subcarrier (frequency) and symbol (time) indexes, respectively, and w

represents the additive noise. The k^{th} phase noise spectral component, $p_{i,k}$, of the i^{th} OFDM symbol can be written as

$$p_{i,k} = \frac{1}{N}\sum_{n=0}^{N-1} e^{j\phi_n^i} \exp\left(\frac{-j2\pi nk}{N}\right) \qquad 0 \le k \le N-1 \qquad (5.2),$$

where $\phi_n^i = \phi_{n-1}^i + \varepsilon$ is a random phase rotation at the n^{th} sample of the i^{th} OFDM symbol in the time-domain. ε is believed to follow a Gaussian random process with a phase noise variance which can be given by

$$\sigma_\varepsilon^2 = 2\pi\beta T_s \qquad (5.3),$$

where T_s and β are the OFDM symbol duration and two-sided 3-dB bandwidth of the phase noise process, respectively.

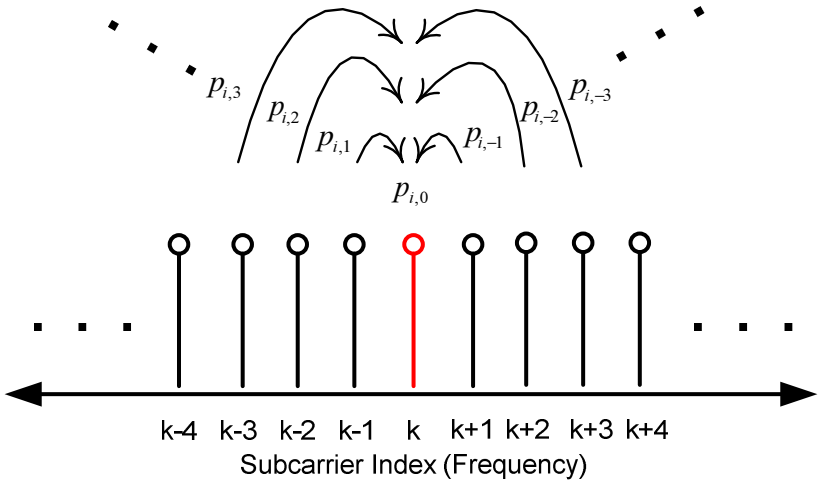

Figure 5-1: Illustration of the effect of ICI due to the phase noise spectral components.

One can rewrite equation 5.1 by separating the first term as

$$r_{i,k} = \sum_{q=0}^{N_{sc}-1} p_{i,\langle k-q\rangle} h_q c_{i,q} + w_{i,k} = p_{i,0} h_k c_{i,k} + \sum_{q=0, q\neq k}^{N_{sc}-1} p_{i,\langle k-q\rangle} h_q c_{i,q} + w_{i,k} \qquad (5.4).$$

As seen in equation 5.4, $p_{i,0}$ is a common term, rotating every subcarrier and therefore, based on the definition, it reflects the CPE contribution. The summation term represents the effect of neighboring subcarriers via other phase noise harmonics that cause ICI. Figure 5.1

depicts this relation. In other words, the received subcarrier, $r_{i,k}$, is influenced not only by the rotation of the k^{th} subcarrier due to $p_{i,0}$ but also by ICI of the adjacent subcarriers because of $p_{i,k}$ where $1 \le k \le N_{SC} - 1$. Estimating these harmonics is the key to ICI compensation.

On the other hand, unlike conventional CO-OFDM systems, reduced-guard-interval CO-OFDM (RGI-CO-OFDM) systems experience dispersion-enhanced-phase-noise (DEPN) due to the phase noise generated by LO at the receiver side. This occurs because the chromatic dispersion (CD) induced walk-off becomes comparable to the OFDM symbol length. Therefore, as shown in [82,117], the same induced phase noise process would degrade the signal quality more if applied at the receiver instead of at the transmitter. The grouped-maximum-likelihood (GML) phase compensation approach is known to partially mitigate the DEPN impairments [117].

5.3. The Concept of Interpolation-Based ICI Compensation

In this section, we study the concepts behind interpolation-based ICI compensation. This compensation scheme operates based on a linear interpolation between the CPE estimates of consecutive OFDM symbols for CO-OFDM transport systems. It is shown in [118] that this approach can minimize the mean-square-error (MSE) of the estimated interpolation of the time-domain phase noise samples. First, we introduce the implementation of the algorithm through a three-step procedure and then we review the mathematical analysis associated with such a scheme to prove that linear interpolation is the most optimal method.

5.3.1. Interpolation-Based ICI Compensation; Implementation

The interpolation-based ICI compensator performs the following three steps [36,40].

Step1: As with the conventional equalizer (CE), scattered pilot subcarriers are used to estimate the CPE in every OFDM data symbol as

$$CPE_i = p_{i,0} = angle\left\{r_{i,k} \times conj\left(h_k c_{i,k}\right)\right\} \qquad k \in PSC \tag{5.5}$$

This estimated CPE value is set equal to the phase noise corresponding to the middle time-domain sample of the same data symbol.

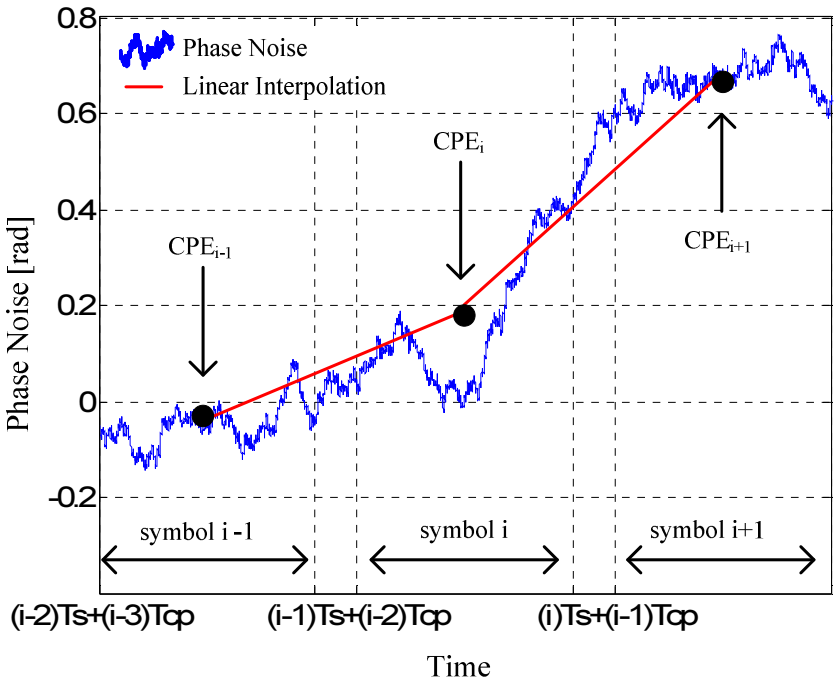

Figure 5-2: The concept of linear interpolation between the CPE estimates of consecutive OFDM symbols for phase noise ICI compensation. T_{cp} is the time duration of the cyclic prefix (CP).

Step 2: The phase noise values of the remaining intermediate samples of each symbol in the time-domain are determined by a linear interpolation using the CPE estimates of the previous, current and next OFDM symbols. This linear interpolation provides the optimum MSE interpolation as long as $\beta T_s << 1$, where β and T_s are the two-sided 3-dB bandwidth of the phase noise process and the symbol duration, respectively [118]. Consequently, the equalization of the i^{th} received symbol can be completed only after reception of the $(i+1)^{th}$ symbol. Therefore, the interpolation-based ICI compensator requires a one-symbol buffer, resulting in a one-symbol latency. Figure 5.2 illustrates this process.

Step 3: After the time-domain phase noise vector is approximated by linear interpolation between consecutive OFDM symbols in step 2, we can derive the spectral components of phase noise estimation using a Fourier transform operation. Then, the received symbol can be equalized as

$$\hat{S}_{i,k} = \left(\sum_{q=-Q/2}^{Q/2} conj\left(\hat{p}_{i,\langle q \rangle}\right) \times r_{i,\langle k-q \rangle} \right) \Big/ \hat{h}_k \tag{5.6},$$

where the ^ symbol above a letter indicates that the corresponding parameter is based on an estimation. $\hat{S}_{i,k}$ is the subcarrier-specific equalized symbol; $\hat{p}$ represents the spectral components of estimated phase noise; the total number of spectral components that are taken into account is controlled by the parameter Q. As equation 5.6 indicates, instead of de-rotating the OFDM samples in the time-domain, the receiver can simply convolve the received symbol with the spectral components of the estimated phase noise followed by a one-tap frequency-domain equalizer. Since the laser phase noise can be approximated as a Wiener process and most of the energy of a Wiener process is concentrated in the first few harmonics, a small value for Q can be used to reduce the number of complex multiplications required in equation 5.6.

5.3.2. Interpolation-Based ICI Compensation; Mathematics

In this subsection, we follow the same approach as that presented in [118]. Considering that the interpolation is performed in the same way for all data OFDM symbols, regardless of symbol index, then without loss of generality the optimum interpolator between the CPE points of the first and second data OFDM symbols can be derived. Generalization to arbitrary symbol indices is then straightforward.

Assume that the sample length of the OFDM symbol and the cyclic prefix (CP) are N and N_{cp}, respectively. The estimated CPEs of the first and the second data OFDM symbols are interpolated into $N+N_{cp}$ intermediate points by designing a filter which minimizes the mean square difference between the actual phase noise process and the phase-interpolating function. This can be expressed as

$$G_{opt} = \arg\min_{G} E\left[\left|\bar{\theta} - Gu\right|^2\right] = \Phi_{\theta u}\Phi_{uu}^{-1} \tag{5.7},$$

where $u = \begin{bmatrix} \hat{p}_{1,0} & \hat{p}_{2,0} \end{bmatrix}^T$. Further, $\bar{\theta} = \begin{bmatrix} e^{j\phi^1_{N/2}} ... e^{j\phi^2_{N/2}} \end{bmatrix}^T$ is an array of the actual phase noise samples which starts from the middle point of the first data OFDM symbol to the middle point of the second OFDM symbol. Therefore, the interpolation region starts from the sample index $N/2$ and ends at the sample index $3N/2+N_{cp}$. The parameter $\Phi_{\theta u}$ is the cross-correlation matrix between $\bar{\theta}$ and u, and Φ_{uu} is the auto-correlation matrix of u. Lastly, G is an $\left(N + N_{cp}\right) \times 2$ interpolation matrix with an optimum solution.

The linear interpolator that connects the CPEs corresponding to the first and the second data OFDM symbols is given by

$$\bar{\theta}_L = G_L \times u \tag{5.8},$$

where the n^{th} element of $\bar{\theta}_L$ and the n^{th} row of G_L are given by

$$\bar{\theta}_L = \frac{1}{N + N_{cp}} \left[\frac{3N}{2} + N_{cp} - n \quad n - \frac{N}{2} \right] \begin{bmatrix} \hat{p}_{1,0} \\ \hat{p}_{2,0} \end{bmatrix}, \qquad \frac{N}{2} \le n < \frac{3N}{2} + N_{cp} \tag{5.9}$$

$$G_L(n,:) = \frac{1}{N + N_{cp}} \left[\frac{3N}{2} + N_{cp} - n \quad n - \frac{N}{2} \right] \tag{5.10}.$$

To prove that the linear interpolation of equation 5.10 is the optimum solution for equation 5.7, we need to evaluate the auto-correlation and the cross-correlation matrices in equation 5.7. To find the auto-correlation matrix of Φ_{uu}, we have

$$\begin{aligned} E\left[e^{j\phi_n} e^{-j\phi_m} \right] &= \frac{1}{\sqrt{2\pi\sigma_\varepsilon^2 |n-m|}} \int_{-\infty}^{\infty} e^{j\Delta\phi} \exp\left(-\frac{(\Delta\phi)^2}{2\pi\sigma_\varepsilon^2 |n-m|} \right) d\Delta\phi \\ &= \exp\left(-\frac{|n-m|\sigma_\varepsilon^2}{2} \right) \end{aligned} \tag{5.11},$$

where $\Delta\phi = \phi_n - \phi_m$. Using the result of equation 5.11 to compute the expected value of the CPE term, we get

$$\begin{aligned} E\left[\left| \hat{p}_{1,0} \right|^2 \right] &= \frac{1}{N^2} \sum_{n=0}^{N-1} \sum_{m=0}^{N-1} E\left[e^{j\phi^1_n} e^{-j\phi^1_m} \right] = \frac{1}{N^2} \sum_{n=0}^{N-1} \sum_{m=0}^{N-1} \exp\left(-\frac{|n-m|\sigma_\varepsilon^2}{2} \right) \\ &= \frac{2\left(1 - \xi^{-N}\right) + N\xi^{-1} - N\xi}{N^2 \left(1 - \xi\right)\left(1 - \xi^{-1}\right)} = E\left[\left| \hat{p}_{2,0} \right|^2 \right] \end{aligned} \tag{5.12},$$

where $\xi = e^{\sigma_\varepsilon^2/2}$. For relatively small values of phase noise variance, we can use the following approximation:

$$e^x \approx \sum_{i=0}^{2}\left(\frac{x^i}{i!}\right) \tag{5.13}.$$

Substituting these values into equation 5.12, we get $E\left[\left|\hat{p}_{1,0}\right|^2\right] = E\left[\left|\hat{p}_{2,0}\right|^2\right] \approx 1$. Similarly, we can compute

$$\begin{aligned} E\left[\hat{p}_{1,0}\hat{p}_{2,0}^*\right] &= \frac{1}{N^2}\sum_{n=0}^{N-1}\sum_{m=N+N_{cp}}^{(2N+N_{cp}-1)} E\left[e^{j\phi_n^1}e^{-j\phi_m^2}\right] \\ &= \frac{\left(1-\xi^N\right)\left(\xi^{-(N+N_{cp})}-\xi^{-(2N+N_{cp})}\right)}{N^2\left(1-\xi\right)\left(1-\xi^{-1}\right)} = E\left[\hat{p}_{1,0}^*\hat{p}_{2,0}\right] \end{aligned} \tag{5.14}.$$

Applying the approximation of equation 5.13, we have

$$E\left[\hat{p}_{1,0}\hat{p}_{2,0}^*\right] = E\left[\hat{p}_{1,0}^*\hat{p}_{2,0}\right] \approx 1 - \frac{\sigma_\varepsilon^2}{2}\left(N+N_{cp}\right) \tag{5.15}.$$

Therefore, the inverse of the auto-correlation matrix Φ_{uu} can be approximated as

$$\Phi_{uu}^{-1} \approx \frac{1}{\left(N+N_{cp}\right)\sigma_\varepsilon^2}\begin{bmatrix} 1 & \frac{\sigma_\varepsilon^2}{2}\left(N+N_{cp}\right)-1 \\ \frac{\sigma_\varepsilon^2}{2}\left(N+N_{cp}\right)-1 & 1 \end{bmatrix} \tag{5.16}.$$

The cross-correlation matrix, $\Phi_{\theta u}$, is an $\left(N+N_{cp}\right)\times 2$ matrix that can be computed in a manner similar to Φ_{uu}. The expression for the first and second column of $\Phi_{\theta u}$ can be written as follows:

$$\begin{aligned} \Phi_{\theta u}(n,1) &= E\left[\bar{\theta}_n^*\hat{p}_{1,0}\right] = \frac{1}{N}\sum_{m=0}^{N-1}\exp\left(-\frac{|n-m|\sigma_\varepsilon^2}{2}\right) \\ &\approx 1-\frac{\sigma_\varepsilon^2}{4}(2n-N), \qquad \frac{N}{2} \le n \le \frac{3N}{2}+N_{cp} \end{aligned} \tag{5.17.a}$$

$$\begin{aligned} \Phi_{\theta u}(n,2) &= E\left[\bar{\theta}_n^*\hat{p}_{2,0}\right] = \frac{1}{N_{sc}}\sum_{m=N+N_{cp}}^{2N+N_{cp}-1}\exp\left(-\frac{|n-m|\sigma_\varepsilon^2}{2}\right) \\ &\approx 1+\frac{\sigma_\varepsilon^2}{4}\left(2n-3N-2N_{cp}\right), \qquad \frac{N}{2} \le n \le \frac{3N}{2}+N_{cp} \end{aligned} \tag{5.17.b}.$$

Therefore, we can write the linear form of the optimum interpolator matrix between the first and the second OFDM data symbols as

$$G_{opt}(n,:) \approx \Phi_{\theta u}(n,:)\Phi_{uu}^{-1} \approx \frac{1}{N+N_{cp}}\left[-n+\frac{3N}{2}+N_{cp} \quad n-\frac{N}{2}\right] = G_L(n,:) \qquad (5.18),$$

where $G_{opt}(n,:)$ represents the n^{th} row of G_{opt}.

5.4. Earlier Simulation Studies of the Performance of Interpolation-Based ICI Compensator

In this section, we present a selection of our early investigations on the performance of the interpolation-based ICI compensator [36,111]. Our study is conducted in a conventional single-polarization CO-OFDM system, based on direct electro-optic (E/O) up-conversion and direct opto-electronic (O/E) down-conversion. The original data at 40 Gb/s is first divided and mapped onto 1024 frequency subcarriers with 16-QAM modulation format, and subsequently transferred to the time-domain using an IFFT of size 2048 with zeros occupying the unused portion. A cyclic prefix of length 300 is used to accommodate dispersion. The overheads of pilot symbols and subcarriers are 3% and 5%, respectively. The resulting electrical OFDM data signal is then electro-optically converted using an I/Q Mach-Zehnder modulator (I/Q-MZM). The optical transmission link consists of 10 uncompensated SMF spans with a dispersion parameter of 17 ps/nm.km, a nonlinear coefficient of 1.2 $W^{-1}.km^{-1}$, a PMD coefficient of 0.2 ps/√km and a loss parameter of 0.2 dB/km. Spans are 80 km long and are separated by erbium doped fibre amplifiers (EDFAs) with a noise figure of 5 dB. The launch power to each fibre span is set at -6 dBm. To mimic the continuous time characteristics of the optical channel, 50 different random sets of time-domain realizations of the laser phase noise is simulated. The laser phase noise is modeled using the well-established model described in [104]. This model assumes that the laser phase undergoes a random walk where the steps are individual spontaneous emission events that instantaneously change the phase by a small amount in a random way. At the optical receiver, an optical filter with a bandwidth of 0.4 nm is applied to reject the out-of-band ASE noise. The receiver is based on an intradyne CO-OFDM scenario in which the OFDM signal beats with

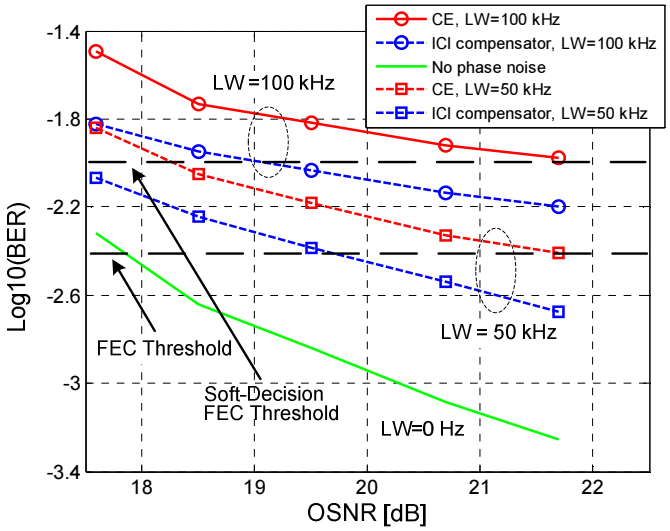

Figure 5-3: Simulation results of the BER performance of ICI compensator for laser linewidth scenarios of 50 kHz and 100 kHz. OSNR bandwidth is 0.1 nm.

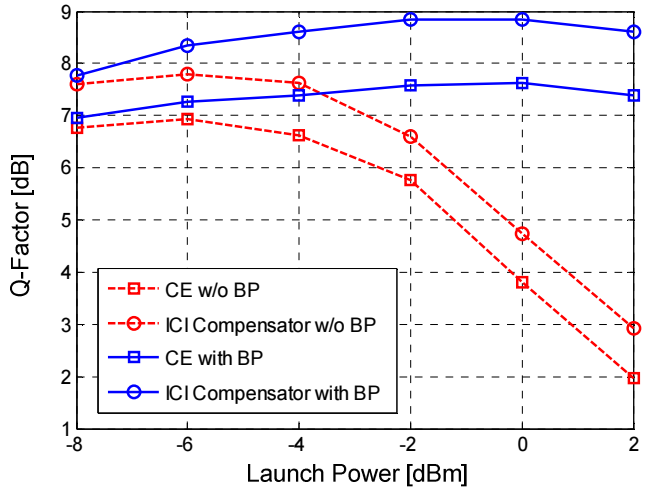

Figure 5-4: Simulation results of the Q-factor versus launch power for ICI compensator and CE with and without BP nonlinearity compensation scheme.

the optical LO signal in an optical 90° hybrid to obtain the signal I and Q components. Throughout this simulation study, a *Q* parameter of 10 is considered.

Figure 5.3 compares the bit-error rate (BER) performance of the interpolation-based ICI compensator and the CE versus the received optical signal-to-noise-ratio (OSNR) for two

different laser linewidths of 50 kHz and 100 kHz. The linewidths of the transmitter and receiver lasers are identical. The signal quality after transmission is degraded by ASE noise, fibre nonlinearities, and laser phase noise. The ICI compensator provides better signal quality than CE does across the received OSNR range of study, demonstrating that it does not suffer from error propagation even in noisy scenarios. At the error-free threshold of forward-error-correction (FEC), the commonly reported BER value of 3.8×10^{-3}, the ICI compensator improves the OSNR requirement by 2 dB for the laser linewidth of 50 kHz. At a BER value of 1.12×10^{-2}, the threshold of soft-decision FEC [119], the ICI compensator improves the OSNR requirement by 2.5 dB for the laser linewidth of 100 kHz. Slightly higher improvements can be achieved by increasing the Q parameter in equation 5.6.

Since the fibre nonlinearity is one of the main impairments in CO-OFDM transmission systems [7], we investigate the Q-factor performance (derived from BER) of the interpolation-based ICI compensator and the CE versus the fibre launch power in order to compare their behaviours in the presence of strong nonlinearity. In addition, we study the same scenario in conjunction with the back-propagation (BP) nonlinearity compensation scheme [106]. In this study, the BP employs two equidistant steps per fibre span, and the linewidth of the lasers at both the transmitter and the receiver is set to 100 kHz. As seen in figure 5.4, the interpolation-based ICI compensator provides better performance than CE does across the launch power range of study for scenarios both with and without BP. The ICI compensator in conjunction with BP enhances the signal quality more effectively; this is due to the nonlinearity not being considered the main impairment of the transmission link, and the effect of the phase noise induced ICI is more pronounced. However, for extreme nonlinear scenarios, i.e. relatively higher launch power without BP, the performance of the ICI compensator is compromised since the degeneration due to nonlinearity is the prominent impairment.

5.5. Experimental Study of the Performance of Interpolation-Based ICI Compensator

Figure 5.5 provides a schematic of the experimental setup. The original binary pseudo-random bit sequence (PRBS) data with a length of 2^{17}-1 is first divided and mapped onto 224 frequency subcarriers with QPSK modulation format and is subsequently transferred to the time-domain using an IFFT of size 256 with zeros occupying the remainder of the unused space, fixing the value 1.14 as the oversampling ratio. In this RGI-DP-CO-OFDM system, a cyclic prefix of length 8, 2 pilot symbols for every 50 data symbols, and 4 pilot subcarriers are employed. The in-phase (I) and quadrature (Q) parts of the resulting digital OFDM signal are then loaded separately onto two field-programmable gate arrays (FPGAs) to electrically generate the electrical I and Q via two digital to analog converters (DACs), operating at 32 GS/s. Taking into consideration the the oversampling ratio of 1.14, the analog electrical I and Q signals at 28 Gbaud OFDM are generated and then fed into an I/Q Mach-Zehnder modulator (I/Q-MZM). Immediately following the I/Q-MZM, a dual polarization emulator is used to imitate a dual-polarization multiplexed transmitter. The optical transmission link consists of an uncompensated four-span optical recirculating loop with SMF having a dispersion parameter of 17 ps/nm.km, a nonlinear coefficient of 1.2 $W^{-1}.km^{-1}$ and a loss parameter of 0.18 dB/km. The spans are each 80 km long and are separated by EDFAs with a noise figure of 5-6 dB. At the optical receiver, two optical filters with bandwidths of 0.4 nm and 0.8 nm are applied before and after the preamplifier, respectively, to reject the out-of-band accumulated spontaneous emission (ASE) noise. The receiver is based on the intradyne scenario in which the received signal beats with the optical LO signal in an optical polarization-diversity 90° hybrid to obtain the I and Q components. The LO is tuned such that it is within the range of approximately tens of MHz of the received signal's centre frequency. The four pairs of balanced outputs from the hybrid are detected by four balanced photodetectors and are then electrically sampled and asynchronously digitized at 80 GS/s using two commercial 4-channel real-time oscilloscopes, equipped with analog-to-digital converters (ADCs) characterized by 33 GHz of analog bandwidth, a nominal resolution of 8-bits, and a frequency-dependent effective number of bits (ENoB)

between 4 and 5. The four signals are then transferred to a PC for off-line processing. Throughout this study an intra-symbol frequency-domain averaging (ISFA) algorithm with an averaging parameter of 9 and a maximum likelihood (ML) phase estimation were incorporated in the off-line processing [65].

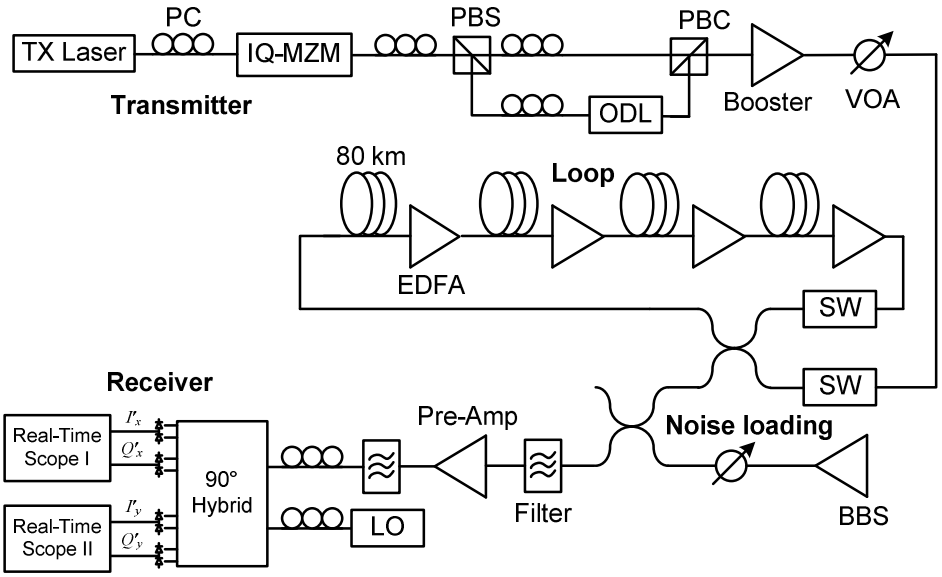

Figure 5-5: RGI-DP-CO-OFDM experimental setup.

The linewidth of the ECL was less than 100 kHz. For the DFB laser used in this experiment, we measured the laser phase noise variance σ_ϕ^2 using a coherent detection algorithm as described in [120,121] with an averaging window of 50 symbols and a relative delay of 50 symbols. The measured data was then converted to linewidth using $LW = \sigma_\phi^2 / 2\pi T_s$ where T_s represents the symbol duration; this formula is applied assuming that the laser phase noise exhibits a Wiener process [120,121].

Figures 5.6 and 5.7 show the BER performance of the interpolation-based ICI compensator versus the optical-signal-to-noise-ratio (OSNR) at optical back-to-back (B2B) for different numbers of estimated phase noise spectral components (harmonics). In figure 5.6 the DFB laser is employed at the transmitter, and in figure 5.7 the DFB laser is used at the receiver. The performance of the ICI compensator would be improved by increasing the

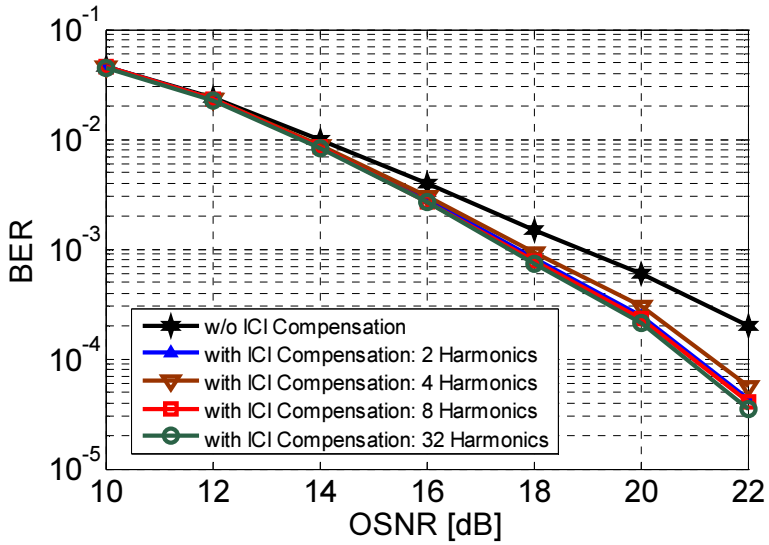

Figure 5-6: Experimental results of the BER versus OSNR for different ICI estimation harmonics. The DFB laser is employed at the transmitter.

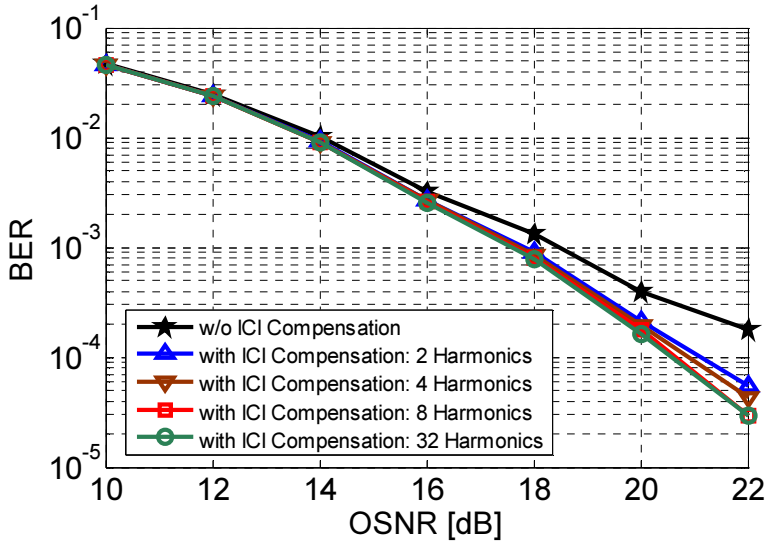

Figure 5-7: Experimental results of the BER versus OSNR for different ICI estimation harmonics. The DFB laser is employed at the receiver.

number of estimated phase noise spectral components. Nevertheless, considering that most of the energy of the phase noise process is concentrated in the first few harmonics, most of the signal quality improvement is observed for the first few harmonics. As one can see, the higher the OSNR, the more effectively the ICI compensator performs. The ICI compensator

always provides better signal quality than does the CE (or similar quality for lower OSNRs) over the received OSNR range of study. This confirms that the ICI compensator does not suffer from error propagation even in noisy scenarios. We choose a harmonic number of 8 for further studies in the rest of this chapter. Furthermore, in figures 5.6 and 5.7 we see very similar performances, this is due to the fact that DEPN does not exist in case of B2B (no dispersion).

Figure 5.8 compares the BER performance of the interpolation-based ICI compensator and the CE versus transmission distance in the presence of weak DEPN. The DFB laser and the ECL were used at the transmitter and the receiver, respectively. The blue and red curves correspond to equalization without and with ICI compensation, respectively. The ICI compensator, red curve, shows better performance than does the CE, blue curve, achieving a transmission reach of 2300 km at the BER threshold of 1×10^{-3} and demonstrating a transmission reach improvement of 24%. In figure 5.9, we again present the BER performance of the ICI compensator and the CE versus transmission distance; however, this time, the ECL is used at transmitter and the DFB laser is employed at receiver, stimulating a strong DEPN effect. The blue and red curves correspond to equalization without and with ICI compensation, respectively. Comparing figures 5.8 and 5.9, a significant degradation in the transmission reach is observed due to the strong DEPN effect. However, the ICI compensator, red curve, still provides better performance than does the CE, blue curve, achieving a transmission reach of 1800 km at the BER threshold of 1×10^{-3} and demonstrating a transmission reach improvement of 13%.

In [82,117], the grouped maximum likelihood (GML) algorithm was proposed to compensate for the DEPN impairment. To further our study, we applied the ICI compensation scheme in conjunction with the GML algorithm. In figures 5.9, the green and black curves correspond to the GML equalization with and without ICI compensation, respectively. As can be seen from figure 5.9, the ICI compensator in conjunction with the GML algorithm, black curve, improves the transmission reach by 13% providing a total reach of 2300 km.

Finally, in order to compare our results with the theoretical values, we conduct a numerical study to observe the behaviour of the ICI compensator; we use the OptiSystem and

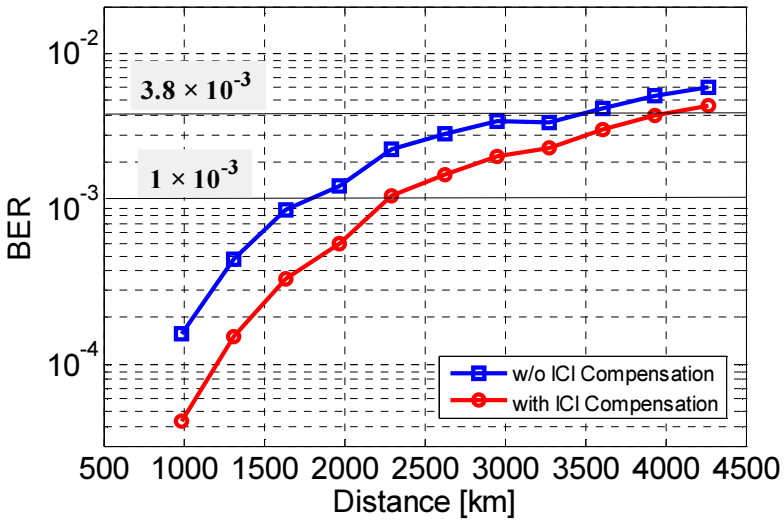

Figure 5-8: Experimental results of the BER versus distance when the DFB laser is employed at the transmitter (weak DEPN).

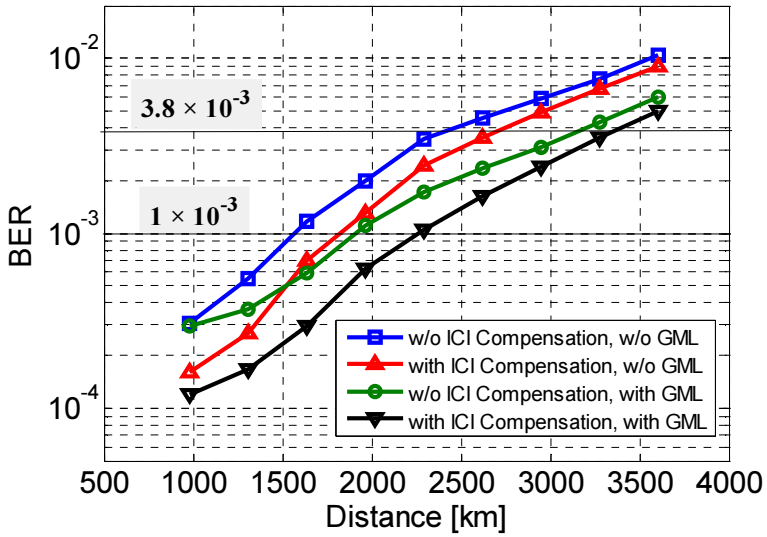

Figure 5-9: Experimental results of the BER versus distance when the DFB laser is employed at the receiver (strong DEPN).

MATLAB co-simulators, with numerical models based on the experimental structure and parameters. Figures 5.10 and 5.11 show the simulation results for the DFB laser at the transmitter and receiver, respectively. Although we note differences in the simulated and measured transmission reach, the overall performance trends exhibited by the equalizers are

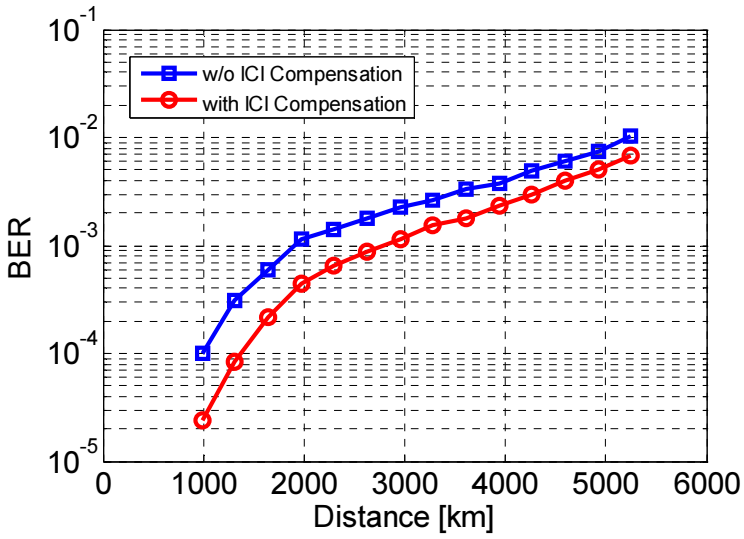

Figure 5-10: Simulation of the BER versus distance when the DFB laser is employed at the transmitter (weak DEPN).

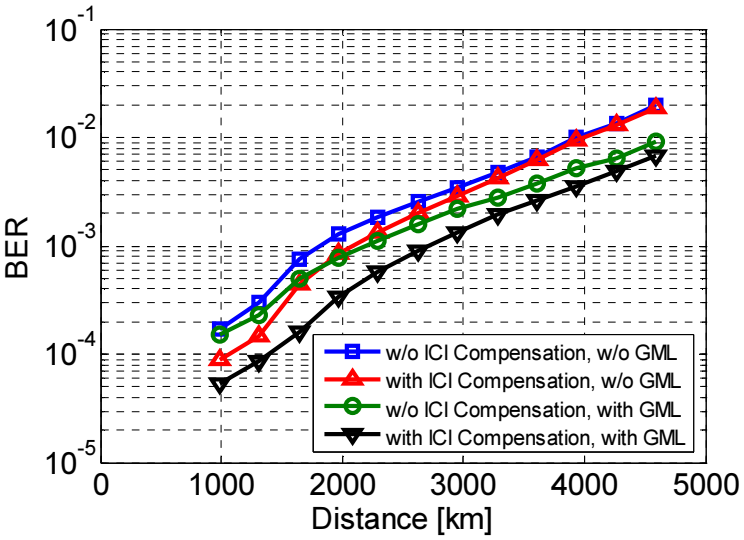

Figure 5-11: Simulation of the BER versus distance when the DFB laser is employed at the receiver (strong DEPN).

similar. From the plots, it is seen that the numerical simulations suggest a longer transmission reach for the ICI compensator. Differences between simulation and experimental results can be attributed to several reasons including the noise of the real-time oscilloscope, the simplified transmitter and receiver models in OptiSystem simulator and the non-ideal

DAC and ADC models considering the mismatch between the physical resolution in simulation and the ENoB in practice.

5.6. System Complexity

As discussed in subsection 4.4.3, the complexity of an equalization algorithm directly affects the implementation cost of the transmission link because of hardware costs and power consumption. In this section, we provide a brief comparison of the complexity of the interpolation-based ICI compensator and the CE in terms of the number of required complex multiplications per bit, taking into account the FFT operations, the channel estimation, and equalization. As in subsection 4.4.3, in this study we use the same complexity for multiplication and division. We assume that the channel is estimated every N_{CE} symbols and that R_{CE} is the training symbol overhead. M denotes the number of bits per symbol. As presented in equation 4.18, the complexity of the CE in an RGI-DP-CO-OFDM system, C_{CE}, can be expressed as

$$C_{CE} = \frac{N_1\left(\log_2\left(N_1\right)+1\right)n'_{MC}}{\left(N_1 - N_{CD}+1\right)\log_2\left(M\right)} + \frac{n_{MC}\log_2\left(N_2\right)+2+\dfrac{5}{N_{CE}R_{CE}}}{\log_2\left(M\right)}, \tag{5.19}$$

where N_1, N_2, n_{MP} and n'_{MP} are the FFT lengths of the first static frequency-domain equalization (FDE), the FFT lengths of the second adaptive FDE, the OFDM oversampling ratio and the modified FDE oversampling ratio, respectively. N_{CD} represents the minimum number of equalizer taps necessary to compensate for chromatic dispersion (CD) [83]. The interpolation-based ICI compensator has similar complexity to the CE in terms of channel estimation; however, one more FFT operation per symbol is required to derive the phase noise spectral components from the estimated time-domain phase noise samples. This can be realized by $N_3\log_2\left(N_3\right)/2$ complex multiplications per symbol for each polarization where N_3 is the corresponding FFT size. A Q-point FFT ($N_3 = Q$) provides the least complexity. Moreover, the equalization is performed based on (3) resulting in $QN_2\left(1-R_{CE}\right)/n_{MC}$ more complex multiplications per symbol per polarization used to de-convolve the estimated phase noise spectral harmonics. Assuming that for each polarization every symbol

transmits $N_2 \log_2(M)/n_{MC}$ bits then the total complexity for the interpolation-based ICI compensator, C_{ICI}, reduces to

$$C_{ICI} = \frac{N_1(\log_2(N_1)+1)n'_{MC}}{(N_1 - N_{CD}+1)\log_2(M)} + \frac{n_{MC}\log_2(N_2)+2+\frac{5}{N_{CE}R_{CE}}}{\log_2(M)} + \frac{QN_2(1-R_{CE})/n_{MC} + N_3\log_2(N_3)}{N_2\log_2(M)} \quad (5.20).$$
$$= C_{CE} + \frac{QN_2(1-R_{CE})/n_{MC} + N_3\log_2(N_3)/2}{N_2\log_2(M)}$$

In retrieving the spectral components of the estimated phase noise, a relatively small FFT size, N_3, offers less complexity but the corresponding aliasing effect can reduce the improvement. We investigated and empirically observed that an FFT size of $4Q$ points guarantees a negligible aliasing effect that does not compromise the ICI mitigation.

Considering that a small value can be used as the parameter Q, as we have seen in figures 5.6 and 5.7, the overall complexity of the interpolation-based ICI compensator can be quite low. For this experiment, we considered 8 harmonics and a $4Q$-point FFT for the ICI compensation and observed a complexity of 25% in terms of the number of complex multiplications required.

5.7. Conclusion

In this chapter, we proposed a non-iterative interpolation-based compensation algorithm to partially mitigate the phase noise induced ICI in CO-OFDM transport systems. We investigated the performance of this algorithm via simulations and experiments. Experimental results demonstrated an improvement in signal quality for a 112 Gb/s QPSK RGI-DP-CO-OFDM transmission scheme over an uncompensated link employing a low-cost DFB laser. An improvement of 24% and 13% in the transmission distance was observed in the presence of weak and strong dispersion-enhanced-phase-noise (DEPN), respectively. Robustness to error propagation and the low computational complexity are the main advantages of this approach. Using more sophisticated methods, such as iterative algorithms and/or joint data and phase noise estimation, can result in better performance; however, their associated implementation complexity with respect to the proposed interpolation-based ICI compensation method is significantly higher.

Chapter 6

Conclusions

6.1. Summary

Traditional optical communication systems have incorporated moderately straightforward signal modulation and demodulation schemes for quasi-static optical-fibre channels, whereas wireless communications have developed more sophisticated schemes due to their need for adaptation to relatively fast deep fading environments. However, the recent trend towards agile, reconfigurable, and adaptive optical networks that support transmission rates beyond 100 Gb/s has pushed optical transport technologies closer to their wireless counterparts. Thanks to recent advances in both complementary-symmetry metal-oxide-semiconductor (CMOS) and silicon technologies, digital signal processing (DSP) enabled

software-defined optical transmission (SDOT) has become a mainstream technology in recent years in not only the research domain but also commercially. Coherent optical orthogonal frequency division multiplexing (CO-OFDM) has been intensively investigated as a promising modulation format for realizing coherent transmission systems. With its high spectral efficiency attributed to the subcarriers overlapping in the frequency-domain, CO-OFDM can alleviate the required oversampling ratio and consequently the required electrical bandwidth at the transmitter and the receiver. In addition it provides sub-wavelength bandwidth access and adaptive data rates via bit and power loading, which are ideal features for agile, adaptive, and reconfigurable optical networks.

This thesis reviewed the concepts behind CO-OFDM transmission systems and their associated DSP algorithms. The original contributions presented in this thesis are two equalization schemes: the adaptive decision-directed channel equalizer (ADDCE), which aims to reduce the required overhead in CO-OFDM systems, and the non-iterative interpolation-based inter-carrier-interference (ICI) compensator that mitigates the laser phase noise induced ICI.

In chapter 1, we discussed the new era in optical communication networks arising from rapid growth in traffic, merging video applications, and recent advances in CMOS technology. The motivations for using reconfigurable optical networks, along with DSP-based and software-defined optical transmission (SDOT) systems, were described. A brief background on CO-OFDM transports systems, and their associated merits, was provided. Finally, we identified and described briefly the original contributions of this thesis.

Chapter 2 was dedicated to the fundamentals of CO-OFDM systems, including the mathematical background of OFDM signal generation, and the DSP algorithms for cyclic prefix (CP), synchronization, carrier frequency offset compensation, and channel estimation. Commonly used channel estimation algorithms, such as intra-symbol-frequency-averaging (ISFA), least square (LS), and maximum likelihood (ML), were explained. We also reviewed different multiple-input multiple-output (MIMO) configurations in CO-OFDM systems and analytically studied the signal profile and the channel estimation in a

2x2 MIMO-CO-OFDM. Moreover, different implementations of CO-OFDM to mitigate the CP overhead were introduced.

In chapter 3, we described our experimental coherent optical transmission setup, including: digital-to-analog converter (DAC), electro-optic (E/O) up-conversion, optical recirculating loop, opto-electronic (O/E) down-conversion, and analog-to-digital converter (ADC).

In chapter 4, we explained our work on decision-directed equalizers in CO-OFDM systems. First, we presented early simulation studies for single-polarization CO-OFDM systems, namely the adaptive weighted channel equalizer (AWCE) and the decision-directed phase equalizer (DDPE). We then expanded this same idea to 2x2 MIMO-CO-OFDM systems by proposing the adaptive decision-directed channel equalizer (ADDCE). Experimental studies, at 28 GBaud for reduced-guard-interval dual-polarization CO-OFDM (RGI-DP-CO-OFDM) transport systems with quadrature-phase-shift-keying (QPSK) and 16-quadrature-amplitude-modulation (16-QAM) formats, were presented. Moreover, we characterized the computational complexity of the ADDCE. By comparing the ADDCE and the conventional equalizer (CE), we demonstrated that the ADDCE requires significantly less overhead, offers longer transmission reach, and has higher resilience against the effects of synchronization timing error and residual dispersion.

In chapter 5, the concept of interpolation-based ICI compensation was investigated. First, we briefly explained the effect of phase noise on the OFDM signal. Afterward, the principles of interpolation-based ICI compensation, including its implementation and mathematical foundation, were reviewed. We presented preliminary simulation studies on the performance of the interpolation-based ICI compensator in conventional single-polarization CO-OFDM systems. We then experimentally investigated this algorithm in an RGI-DP-CO-OFDM experimental setup, at 28 GBaud for QPSK format, employing a low-cost distributed-feedback (DFB) laser. Finally, the complexity of the proposed scheme was characterized. By comparing the interpolation-based ICI compensator and the conventional equalizer (CE), we demonstrated that the proposed ICI compensator provides longer transmission reach.

6.2. Future Research Direction

CO-OFDM is a fast-progressing research area in optical communications; it is very exciting to observe that one of the most advanced concepts in the field of modulation, coding, and reception is now being applied to the optical domain. Considering that OFDM has been an important modulation scheme in wireless technology for decades, the process of finding equalization and compensation algorithms is facilitated since already existing approaches from wireless channels can be adopted for use in optical channels. However, there are a few major distinctions. In optical fibre communications, the signals are typically transmitted and processed at much higher speeds. Commercial products at 100 Gb/s have been deployed since 2010 and 1 Tb/s products will be shipped by early 2013. This presents tremendous challenges and opportunities in the fields of high-speed electronics and photonics. In addition, it highlights the need for computationally efficient DSP schemes with the least possible buffer delay and overhead. On the other hand, fibre nonlinearities, in conjunction with a dispersive medium and a channel with memory, come with new challenges in the field of fibre-optic transmissions that have never been investigated by the wireless community.

A natural next step in line with this work would be to investigate the performance of the ADDCE and the ICI compensator in a superchannel structure with a transmission rate of 1 Tb/s or higher. A superchannel is a set of very tightly spaced channels that supports a high data rate signal originating from a single laser source and consisting of multiple frequency-locked carriers that are synchronously modulated [122-124]. Following synthesis via parallel multiplexing, the superchannel signal propagates, goes through routing devices, and gets detected, all as a single entity [122-124]. The main idea is that by establishing a suitable orthogonal condition among the modulated optical carriers, coherent crosstalk can be eliminated. The overall bit-rate can be in the terabit per second range; this could constitute the future of terabit Ethernet technology. Due to the nearly rectangular shape of the spectrum and the concept of orthogonality, a CO-OFDM signal is considered a favourable candidate for realizing high-capacity transmission using a superchannel structure by close allocation of multiple OFDM signals in the frequency-domain [81,124,125]. In this thesis, we

demonstrated the capability of the ADDCE at 112 Gb/s and 224 Gb/s for long-haul transmission with an overhead of less than 2.6%; however, realization of terabit transmission with such a low overhead would be an interesting development. On the other hand, employing DFB lasers at the transmitting side of the superchannel structure is an economical solution for some commercial systems. In this case, the interpolation-based ICI compensator can be exploited to partially mitigate the ICI effect due to the laser phase noise.

In optical fibre communications, wavelength-division multiplexing (WDM) is the technology, capable of multiplexing a number of optical carrier signals onto a single optical fibre by using different wavelengths. Bidirectional communications over one strand of fibre, as well as multiplication of capacity are the main advantages of WDM and dense WDM (DWDM) systems. Considering the fact that in WDM systems, several optical channels are sharing the same fibre medium, the transmitted signals would be susceptible to fibre nonlinearities especially cross-phase modulation (XPM) and four-wave-mixing (FWM). An experimental study can investigate the performance of ADDCE and interpolation-based ICI equalizer for WDM and DWDM transmission systems.

OFDM is also an excellent candidate for use in indoor optical wireless applications, radio-over-fibre (RoF) systems, and passive optical network (PON) applications. PON is the technology to replace conventional cable-based access networks to support higher transmission, longer reach, and higher overall capacity for more users. For future PON applications different PON technologies have been proposed, including wavelength-division-multiplexing (WDM) [126], subcarrier-multiplexing (SCM) [127], optical-code-division-multiplexing (OCDM) [128], and orthogonal-frequency-division-multiple-access (OFDMA) [129]. OFDMA-PON is a multiple-access technology that allows assigning subsets of subcarriers to multiple users in a dynamic manner. OFDMA enables flexible time- and frequency-domain resource partitioning. In addition, it can easily bridge wireless and optical access networks via RoF systems. Coherent OFDMA-PON has also been shown to be a promising approach in offering resource management [130,131]. Optical fibre transmissions in metro areas are known to experience polarization-mode-dispersion (PMD) with higher rate of change due to mechanical stress and vibrations. The use of adaptive algo-

rithms such as the ADDCE in OFDMA-PON would be beneficial for improving the signal quality while alleviating the overhead requirements. Furthermore, inexpensive implementation is an integral feature of PON technologies. Therefore, employing DFB lasers rather than external cavity lasers (ECLs) would be a significant step towards cost reduction. Low-complexity interpolation-based ICI compensators can be used to mitigate the laser phase noise induced ICI in such scenarios.

Raman amplifiers are another type of optical amplifiers which operate based on Raman gain resulted from the stimulated Raman scattering effect. Although, the Raman-active medium is often an optical fibre in telecom applications, it can also be a bulk crystal, a waveguide in a photonic integrated circuit, or a cell with a gas or liquid medium [4]. In optical transmission systems, Raman amplifiers are known to improve the noise figure and reduce the nonlinear penalty of the amplifier, enabling longer amplifiers spans, higher bit rates, closer channel spacing and operation near the zero dispersion wavelength [4]. In the work of this thesis, erbium-doped fibre amplifiers (EDFA) were employed as the amplification units in the transmission link due to the lab availability. It would be interesting to launch a separate study to investigate the performance of CO-OFDM transmission systems equipped with Raman amplifiers.

References

1. Cisco Visual Networking Index: Global Mobile Data Traffic Forecast Update, 2011-2016. Information available at: http://www.cisco.com/en/US/solutions/collateral/ns341/ns525/ns537/ns705/ns827/white_paper_c11-520862.pdf
2. Cisco Visual Networking Index: Forecast and Methodology, 2011-2016. Information available at: http://www.cisco.com/en/US/solutions/collateral/ns341/ns525/ns537/ns705/ns827/white_paper_c11-481374.pdf
3. R. E. Wagner, and R. A. Linke, "Heterodyne lightwave systems: moving towards commercial use," IEEE Lightwave Commun. System Magazine 1, pp. 28-35 (1990).
4. G. P. Agrawal, Fibre-optic communication systems (Wiley, New York, 2002).
5. K. P. Ho, Phase-modulated optical communication systems (Springer, New York, 2005).
6. P. J. Winzer, and R. J. Essiambre, "Advanced optical modulation formats," Proc. IEEE 94, 952-985 (2006).
7. W. Shieh, and I. Djordjevic, OFDM for optical communications (Elsevier/Academic Press, San Diego, 2009).
8. S. J. Savory, "Digital coherent optical receivers: algorithms and subsystems," IEEE J. Sel. Top. Quantum Electron. 16, pp. 1164-1179 (2010).
9. R. W. Chang, "Orthogonal frequency division multiplexing," U.S. patent 3,488,445 (1970).
10. W. Shieh, H. Bao, and Y. Tang, "Coherent optical OFDM: theory and design," Opt. Express 16, pp. 841-859 (2008).
11. W. Shieh and C. Athaudage, "Coherent optical orthogonal frequency division multiplexing," Electron. Lett. 42, pp. 587-589 (2006).
12. F. Buchali, R. Dischler, and X. Liu, "Optical OFDM: a promising high-speed optical transport technology," Bell Labs Tech. J. 14, pp. 125-148 (2009).

13. T. Strasser, and J. Taylor, “ROADMS unlock the edge of the network”, IEEE Commun. Magazine 46, pp. 146-169 (2008).
14. E. B. Basch, R. Egorov, S. Gringeri, and S. Elby “Architectural tradeoffs for reconfigurable dense wavelength-division multiplexing systems,” IEEE J. Sel. Top. Quantum Electron. 12, pp. 615-626 (2006).
15. H. Sunnerud, C. Xie, M. Karlsson, R. Samuelsson, and P. A. Andrekson, “A comparison between different PMD compensation techniques,” IEEE J. Lightwave Technol. 20, pp. 368-378 (2002).
16. B. J. Eggleton, A. Ahuja, P. S. Westbrook, J. A. Rogers, P. Kuo, T. N. Nielsen, and B. Mikkelsen, “Integrated tunable fibre gratings for dispersion management in high-bit rate systems,” IEEE J. Lightwave Technol. 18, pp. 1418-1432 (2000).
17. T. Takahashi, T. Imai, and M. Aiki, “Automatic compensation technique for timewise fluctuating polarisation mode dispersion in in-line amplifier systems,” Electron. Lett. 30, pp. 348-349 (1994).
18. D. McGhan, C. Laperle, A. Savchenko, C. Li, G. Mak, and M. O'Sullivan, “5120 km RZ-DPSK transmission over G652 fibre at 10 Gb/s with no optical dispersion compensation,” in Optical Fibre Communication Conference and Exposition and The National Fibre Optic Engineers Conference, Technical Digest (CD) (Optical Society of America, 2005), paper PDP27.
19. H. Sun, K. T. Wu, and K. Roberts, “Real-time measurements of a 40 Gb/s coherent system,” Opt. Express 16, pp. 873-879 (2008).
20. S. J. Savory, G. Gavioli, R. I. Killey, and P. Bayvel, “Electronic compensation of chromatic dispersion using a digital coherent receiver,” Opt. Express 15, pp. 2120-2126 (2007).
21. J. Mitola, “The software radio architecture,” IEEE Commun. Magazine 33, pp. 26-38 (1995).
22. H. F. Haunstein, T. Schorr, A. Zottmann, W. Sauer-Greff, and R. Urbansky, “Performance comparison of MLSE and iterative equalization in FEC systems for PMD channels with respect to implementation complexity,” IEEE J. Lightwave Technol. 24, pp. 4047-4054 (2006).

23. A. Färbert, “Application of digital equalization in optical transmission systems,” in Optical Fibre Communication Conference and Exposition and The National Fibre Optic Engineers Conference, Technical Digest (CD) (Optical Society of America, 2006), paper OTuE5.
24. W. Shieh, X. Yi, Y. Ma, and Q. Yang, “Coherent optical OFDM: has its time come? [Invited],” J. Opt. Netw. 7, pp. 234-255 (2008)
25. X. Liu, S. Chandrasekhar, B. Zhu, P. J. Winzer, A. H. Gnauck, and D. W. Peckham, “448-Gb/s reduced-guard-interval CO-OFDM transmission over 2000 km of ultra-large-area fibre and five 80-GHz-grid ROADMs,” IEEE J. Lightwave Technol. 29, pp. 483-490 (2011).
26. Y. Ma, Q. Yang, Y. Tang, S. Chen, and W. Shieh, “1-Tb/s single-channel coherent optical OFDM transmission over 600-km SSMF fibre with subwavelength bandwidth access,” Opt. Express 17, pp. 9421-9427 (2009).
27. A. Sano, H. Masuda, T. Kobayashi, M. Fujiwara, K. Horikoshi, E. Yoshida, Y. Miyamoto, M. Matsui, M. Mizoguchi, H. Yamazaki, Y. Sakamaki, and H. Ishii, “69.1-Tb/s (432 x 171-Gb/s) C- and extended L-band transmission over 240 Km using PDM-16-QAM modulation and digital coherent detection,” in Optical Fibre Communication Conference, OSA Technical Digest (CD) (Optical Society of America, 2010), paper PDPB7.
28. S. L. Jansen, B. Spinnlera, I. Moritab, S. Randelc and H. Tanakab, “100GbE: QPSK versus OFDM,” J. of Optical Fibre Technol. 15, pp. 407-413 (2009).
29. W. Shieh, R. S. Tucker, W. Chen, X. Yi, and G. Pendock, “Optical performance monitoring in coherent optical OFDM systems,” Opt. Express 15, pp. 350-356 (2007).
30. M. Mayrock and H. Haunstein, “Performance monitoring in Optical OFDM systems,” in Optical Fibre Communication Conference, OSA Technical Digest (CD) (Optical Society of America, 2009), paper OWM3.
31. Q. Yang, W. Shieh, and Y. Ma, “Bit and power loading for coherent optical OFDM,” IEEE Photon. Technol. Lett. 20, pp. 1305-1307 (2008).

32. B. S. Krongold, K. Ramchandran, and D. L. Jones, “Computationally efficient optimal power allocation algorithms for multicarrier communication systems,” IEEE Trans. on Commun. 48, pp. 23-27 (2000).
33. L. Christen, Y. Lize, S. Nuccio, A. Willner, and L. Paraschis, “Variable rate, multi-format receiver design for 10 to 40 Gb/s DPSK and OOK formats,” Opt. Express 16, pp. 3828-3833 (2008).
34. M. E. Mousa-Pasandi and D. V. Plant, “Data-aided adaptive weighted channel equalizer for long-haul optical OFDM transmission systems,” Opt. Express 18, pp. 3919-3927 (2010).
35. M. E. Mousa-Pasandi, Q. Zhuge, X. Xu, M. M. Osman, M. Chagnon, and D. V. Plant, “Experimental Study of a novel adaptive decision-directed channel equalizer in 28 GBaud RGI-DP-CO-OFDM transport systems,” Optics Express 20, pp. 17017-17028 (2012).
36. M. E. Mousa Pasandi, and D. V. Plant, “Non-iterative interpolation-based phase noise ICI mitigation for CO-OFDM transport systems,” IEEE Photon. Technol. Lett. 23, pp. 1594-1596 (2011).
37. S. L. Jansen, I. Morita, T. Schenk, N. Takeda and H. Tankada, “Coherent optical 25.8-Gb/s OFDM transmission over 4160-km SSMF,” IEEE J. of Lightwave Technol. 26, pp. 6-15 (2008).
38. M. E. Mousa-Pasandi, and D. V. Plant, “Zero-overhead phase noise compensation via decision-directed phase equalizer for coherent optical OFDM,” Optics Express 18, pp. 20651-20660 (2010).
39. Q. Zou, A. Tarighat and A. H. Sayed, “Compensation of phase noise in OFDM wireless systems,” IEEE Trans. on Signal Processing 55, pp. 5407-5424 (2007).
40. M. E. Mousa-Pasandi, Q. Zhuge, X. Xu, M. M. Osman, Z. A. El-Sahn, M. Chagnon, and D. V. Plant, “Experimental demonstration of non-iterative interpolation-based partial ICI compensation in 100G RGI-DP-CO-OFDM transport systems,” Optics Express 20, pp. 14825-14832 (2012).
41. J. A. C. Bingham, “Multicarrier modulation for data transmission: an idea whose time has come,” IEEE Commun. Magazine 28, pp. 5-14 (1990).

42. R. van Nee, and R. Prasad, OFDM wireless multimedia communications (Artech House, Boston 2000).
43. W. Y. Zou, and Y. Wu, "COFDM: an overview," IEEE Trans. on Broadcasting 41, pp. 1-8 (1995).
44. R. W. Chang, "Synthesis of band-limited orthogonal signals for multi-channel data transmission," Bell Labs Tech. J. 45, pp. 1775-1796 (1966).
45. R. W. Chang, and R. Gibby, "A theoretical study of performance of an orthogonal multiplexing data transmission scheme," IEEE Trans. on Commun. Technol. 16, pp. 529-540 (1968).
46. S. B. Weinstein, and P. Ebert, "Data transmission by frequency-division multiplexing using the discrete Fourier transform," IEEE Trans. on Commun. Technol. 19, pp. 628-634 (1971).
47. L. J. Cimini, "Analysis and simulation of a digital mobile channel using orthogonal frequency division multiplexing," IEEE Trans. on Commun. 33, pp. 665-675 (1985).
48. Q. Pan, and R. J. Green, "Bit-error-rate performance of lightwave hybrid AM/OFDM systems with comparison with AM/QAM systems in the presence of clipping impulse noise," IEEE Photon. Technol. Lett. 8, pp. 278-280 (1996).
49. I. B. Djordjevic, and B. Vasic, "Orthogonal frequency division multiplexing for high-speed optical transmission," Opt. Express 14, pp. 3767-3775 (2006).
50. A. Lowery, and J. Armstrong, "Orthogonal-frequency-division multiplexing for dispersion compensation of long-haul optical systems," Opt. Express 14, pp. 2079-2084 (2006).
51. W. Shieh, X. Yi, and Y. Tang, "Transmission experiment of multi-gigabit coherent optical OFDM systems over 1000 km SSMF fibre," Electron. Lett. 43, pp. 183-185 (2007).
52. E. Yamada, A. Sano, H. Masuda, E. Yamazaki, T. Kobayashi, E. Yoshida, K. Yonenaga, Y. Miyamoto, K. Ishihara, Y. Takatori, T. Yamada, and H. Yamazaki, "1Tb/s (111Gb/s/ch × 10ch) no-guard-interval CO-OFDM transmission over 2100 km DSF," Opto-Electronics Communications Conference/Australian Conference on Optical Fibre Technology, paper PDP6, Sydney, Australia (2008).

53. D. Wulich, “Definition of efficient PAPR in OFDM,” IEEE Commun. Lett. 9, pp. 832-834 (2005).
54. B. Goebel, S. Hellerbrand, and N. Hanik, “Link-aware precoding for nonlinear optical OFDM transmission,” in Optical Fibre Communication Conference, OSA Technical Digest (CD) (Optical Society of America, 2010), paper OTuE4.
55. R. O’Neil, and L. N. Lopes, “Envelope variations and spectral splatter in clipped multicarrier signals,” in Proc. IEEE Int. Symp. Personal Indoor Mobile Radio Commun., pp. 71-75 (1995).
56. J. Armstrong, “Peak-to-average power reduction for OFDM by repeated clipping and frequency domain filtering,” Electron. Lett. 38, pp. 246-247 (2002).
57. R. W. Bauml, R. F. H. Fischer, and J. B. Huber “Reducing the peak-to-average power ratio of multicarrier modulation by selected mapping,” Electron. Lett. 32, pp. 2056-2057 (1996).
58. S. H. Muller, and J. B. Huber, “A novel peak power reduction scheme for OFDM,” in Proc. IEEE Int. Symp. Personal Indoor Mobile Radio Commun., pp. 1090-1094 (1997).
59. S. Hara, and R. Prasad, Multicarrier techniques for 4G mobile communications (Artech House, Boston, 2003).
60. L. Hanzo, M. Munster, B. J. Choi, and T. Keller, OFDM and MC-CDMA for broadband multi-user communications, WLANs and broadcasting (Wiley-IEEE Press, West Sussex, 2004).
61. T. M. Schmidl, and D. C. Cox, “Robust frequency and timing synchronization for OFDM,” IEEE Trans. on Commun. 45, pp. 1613-1621 (1997).
62. H. Minn, V. K. Bhargava, and K. B. Letaief, “A robust timing and frequency synchronization for OFDM systems,” IEEE Trans. on Wireless Commun. 2, pp. 822-839 (2003).
63. H. Sari, G. Karam, and I. Jeanclaude, “Transmission techniques for digital terrestrial TV broadcasting,” IEEE Commun. Magazine 33, pp. 100-109 (1995).
64. P. Moose, “A technique for orthogonal frequency division multiplexing frequency offset correction,” IEEE Trans. Commun. 42, pp. 2908-2914 (1994).

65. X. Liu, and F. Buchali, “Intra-symbol frequency-domain averaging based channel estimation for coherent optical OFDM,” Opt. Express 16, pp. 21944-21957 (2008).
66. M. Karlsson, J. Brentel, and P. A. Andrekson, “Long-term measurement of PMD and polarization drift in installed fibres,” IEEE J. Lightwave Technol. 18, pp. 941-951 (2000).
67. P. Krummrich, and K. Kotten, “Extremely fast (microsecond timescale) polarization changes in high speed long haul WDM transmission systems,” in Optical Fibre Communication Conference, OSA Technical Digest Series (CD) (Optical Society of America, 2004), paper FI3.
68. S. Hara, M. Mouri, M. Okada, and N. Morinaga, “Transmission performance analysis of multi-carrier modulation in frequency selective fast Rayleigh fading channel,” Wireless Personal Commun. 2, pp. 335-356 (1996).
69. X. Yi, W. Shieh, and Y. Tang, “Phase estimation for coherent optical OFDM,” IEEE Photon. Technol. Lett. 19, pp. 919-921 (2007).
70. J. J. Van de Beek, O. S. Edfors, M. Sandell, S. K. Wilson, and O. P. Börjesson, “On channel estimation in OFDM systems,” in Proc. of IEEE Vehicular Technol. 1995, (Institute of Electrical and Electronics Engineers, Chicago, 1995), pp. 815-819.
71. T. Kimura, “Coherent optical fibre transmission,” IEEE J. Lightwave Technol 5, pp. 414-428 (1987).
72. F. Auracher, and R. Keil, “Method for measuring the RF modulation characteristics of Mach-Zehnder-type modulators,” Appl. Phys. Lett. 36, pp. 626-629 (1980).
73. A. J. Paulraj, D. A. Gore, R. U. Nabar, and H. Bolcskei, “An overview of MIMO communications-A key to gigabit wireless,” in Proc. IEEE 92, pp. 198-218 (2004).
74. J. Armstrong, “OFDM for Optical Communications,” IEEE J. Lightwave Technol. 27, pp. 189-204 (2009).
75. A. P. T. Lau, L. Xu, and T. Wang, “Performance of receivers and detection algorithms for modal multiplexing in multimode fibre systems,” IEEE Photon. Technol. Lett.19, pp. 1087-1089 (2007).

76. A. Al Amin, A. Li, S. Chen, X. Chen, G. Gao, and W. Shieh, "Dual-LP_{11} mode 4x4 MIMO-OFDM transmission over a two-mode fibre," Opt. Express 19, pp. 16672-16679 (2011).
77. S. Randel, M. Magarini, R. Ryf, A. Gnauck, P. Winzer, T. Hayashi, T. Taru, and T. Sasaki, "MIMO-based signal processing of spatially multiplexed 112-Gb/s PDM-QPSK signals using strongly-coupled 3-Core fibre," in 37th European Conference and Exposition on Optical Communications, OSA Technical Digest (CD) (Optical Society of America, 2011), paper Tu.5.B.1.
78. N. Gisin, and B. Huttner, "Combined effects of polarization mode dispersion and polarization dependent losses in optical fibres," Opt. Commun. 142, pp. 119-125 (1997).
79. S. L. Jansen, I. Morita, T. C. Schenk, and H. Tanaka, "Long-haul transmission of 16×52.5 Gbits/s polarization-division-multiplexed OFDM enabled by MIMO processing (Invited)," J. Opt. Netw. 7, pp. 173-182 (2008).
80. X. Liu, and F. Buchali, "A novel channel estimation method for PDM-OFDM enabling improved tolerance to WDM nonlinearity," in Optical Fibre Communication Conference, OSA Technical Digest (CD) (Optical Society of America, 2009), paper OWW5.
81. S. Chandrasekhar, X. Liu, B. Zhu, and D. W. Peckham, "Transmission of a 1.2-Tb/s 24-carrier no-guard-interval coherent OFDM superchannel over 7200-km of ultra-large-area fibre," in Proc. of European Conference on Optical Communication (IEEE, 2009), paper PD2.6.
82. Q. Zhuge, C. Chen and D. V. Plant, "Dispersion-enhanced phase noise effects on reduced-guard-interval CO-OFDM transmission," Opt. Express 19, pp. 4472-4484 (2011).
83. B. Spinnler, "Equalizer design and complexity for digital coherent receivers," IEEE J. Sel. Top. Quantum Electron. 16, pp. 1180-1192 (2010).
84. Raj Kamal, Digital systems principles and design (Pearson Education India, New Delhi, 2006).

85. Steve Kilts, Advanced FPGA design: architecture, implementation, and optimization (Wiley-IEEE Press, New Jersey, 2007).
86. B. Zhang, C. Malouin, and T. J. Schmidt, “Design of coherent receiver optical front end for unamplified applications,” Opt. Express 20, pp. 3225-3234 (2012).
87. C. R. Doerr, L. Zhang, P. J. Winzer, N. Weimann, V. Houtsma, T. Hu, N. J. Sauer, L. L. Buhl, D. T. Neilson, S. Chandrasekhar, and Y. K. Chen, “Monolithic InP dual-polarization and dual-quadrature coherent receiver,” IEEE Photon. Technol. Lett. 23, pp. 694-696 (2011).
88. Sanjay Pithadia, “Smart selection of ADC/DAC enables better design of software-defined radio,” Texas Instruments Application Reports (2009).
89. Q. Zhuge, M. E. Mousa-Pasandi, M. Morsy-Osman, X. Xu, M. Chagnon, Z. Elsahn, and D. Plant, “High performance, low overhead CO-OFDM for next generation fibre transmission systems,” in Signal Processing in Photonic Communications, OSA Technical Digest (online) (Optical Society of America, 2012), paper SpTu2A.4.
90. J. G. Proakis, Digital communications (McGraw-Hill, New York, 1995).
91. B. Muquet, M. de Courville, and P. Duhamel, “Subspace-based blind and semi-blind channel estimation for OFDM systems,” IEEE Trans. on Signal Processing 50, pp. 1699-1712 (2002).
92. M. C. Necker, and G. L. Stuber, “Totally blind channel estimation for OFDM on fast varying mobile radio channels,” IEEE Trans. on Wireless Commun. 3, pp. 1514-1525 (2004).
93. H. Wang, Y. Lin, and B. Chen, “Data-efficient blind OFDM channel estimation using receiver diversity,” IEEE Trans. on Signal Processing 51, pp. 2613-2623 (2003).
94. K. Kikuchi, “Performance analyses of polarization demultiplexing based on constant-modulus algorithm in digital coherent optical receivers,” Opt. Express 19, pp. 9868-9880 (2011).
95. C. Xie, and S. Chandrasekhar, “Two-stage constant modulus algorithm equalizer for singularity free operation and optical performance monitoring in optical coherent

receiver," in 2010 OSA Technical Digest of Optical Fibre Communication Conference (Optical Society of America, 2010), paper OMK3.

96. M. Rim, "Optimally combining decision-directed and pilot-symbol-aided channel estimation," IEE Electronics Lett. 39, pp. 558-560 (2003).
97. J. Ran, R. Grunheid, H. Rohling, E. Bolinth, and R. Kern, "Decision-directed channel estimation method for OFDM systems with high velocities," in Proceedings of IEEE Vehicular Technology Conference, (Institute of Electrical and Electronics Engineers, New York, 2003), pp. 2358-2361.
98. K. G. Wu, and J. A. Wu, "Efficient decision-directed channel estimation for OFDM systems with transmit diversity," IEEE Commun. Lett. 15, pp.740-742, (2011).
99. W. Peng, X. Wu, V. R. Arbab, K.-M. Feng, B. Shamee, L. C. Christen, J.-Y. Yang, A. E. Willner, and S. Chi, "Theoretical and experimental investigations of direct-detected RF-tone assisted optical OFDM systems," IEEE J. Lightwave Technol. 27, pp. 1332-1339 (2009).
100. S. L. Jansen, I. Morita, N. Takeda, and H. Tanaka; "20-Gb/s OFDM transmission over 4,160-km SSMF enabled by RF-Pilot tone phase noise compensation," in Optical Fibre Communication Conference, OSA Technical Digest Series (CD) (Optical Society of America, 2007), paper PDP15.
101. M. E. Mousa Pasandi, and D. V. Plant, "Improvement of phase noise compensation for coherent optical OFDM via data-aided phase equalizer," in National Fibre Optic Engineers Conference, OSA Technical Digest (CD) (Optical Society of America, 2010), paper JThA10.
102. M. E. Mousa Pasandi, J. Haghighat, and D. V. Plant, "Adaptive weighted channel equalizer for direct-detection optical OFDM transmission systems," in Proceedings of IEEE Photonics Society Summer Topicals'09, (Institute of Electrical and Electronics Engineers, New York, 2009), pp. 85-86.
103. J. Palicot, and A. Goupil, "Performance analysis of the weighted decision feedback equalizer," J. Signal Processing 88, pp. 284–295 (2008).
104. R. W. Tkach, and A. R. Chraplyvy, "Phase noise and linewidth in an InGaAsP DFB laser," IEEE J. Lightwave Technol. 4, pp. 1711-1726 (1986).

105. C. Xie, D. Werner and H. F. Haunstein, “Dynamic performance and speed requirement of polarization mode dispersion compensators,” IEEE J. Lightwave Technol. 24, pp. 3968-3975 (2006).

106. E. Ip, and J. M. Kahn, “Compensation of dispersion and nonlinear impairments using digital backpropagation,” IEEE J. Lightwave Technol. 26, pp. 3416-3425 (2008).

107. C. J. Youn, X. Liu, S. Chandrasekhar, Y. H. Kwon, J. H. Kim, J. S. Choe, D. J. Kim, K. S. Choi, and E. S. Nam, “Channel estimation and synchronization for polarization-division multiplexed CO-OFDM using subcarrier/polarization interleaved training symbols,” Opt. Express 19, pp. 16174-16181 (2011).

108. S. Chen, Qi Yang, Y. Ma and W. Shieh, “Real-time multi-gigabit receiver for coherent optical MIMO-OFDM signals,” IEEE J. Lightwave Technology 27, pp. 3699-3704 (2009).

109. B. Inan, B. Spinnler, F. Ferreira, A. P. Lobato Polo, S. Adhikari, V. Sleiffer, D. van den Borne, N. Hanik, and S. L. Jansen, “Equalizer complexity of mode division multiplexed coherent receivers,” in Optical Fibre Communication Conference, OSA Technical Digest (Optical Society of America, 2012), paper OW3D.4

110. M. Kuschnerov, F. N. Hauske, K. Piyawanno, B. Spinnler, M. S. Alfiad, A. Napoli, and B. Lankl, “DSP for coherent single-carrier receivers,” IEEE J. Lightwave Technol. 27, pp. 3614-3622 (2009).

111. M. E. Mousa Pasandi, and D. V. Plant, “Non-iterative interpolation-based phase noise ICI mitigation for CO-OFDM transport systems,” in Signal Processing in Photonic Communications, OSA Technical Digest (CD) (Optical Society of America, 2011), paper SPMB6.

112. W. Shieh, “Maximum-likelihood phase and channel estimation for coherent optical OFDM,” IEEE Photon. Technol. Lett. 20, pp. 605-607 (2008).

113. C. Yang, F. Yang, and Z. Wang, “Orthogonal basis expansion-based phase noise estimation and suppression for CO-OFDM systems,” IEEE Photon. Technol. Lett. 22, pp. 51-53 (2010).

114. Q. Zou, A. Tarighat, and A. H. Sayed, “Compensation of phase noise in OFDM wireless systems,” IEEE Transaction on Signal Processing 55, pp. 5407-5424 (2007).

115. L. Tomba, “On the effect of Wiener phase noise in OFDM systems,” IEEE Trans. on Commun. 46, pp. 580-583 (1998).

116. Y. Mostofi, and D. C. Cox, “ICI mitigation for pilot-aided OFDM mobile systems,” IEEE Trans. on Wireless Commun. 4, pp. 765-774 (2005).

117. Q. Zhuge, M. E. Mousa-Pasandi, M. M. Osman, X. Xu, M. Chagnon, Z. A. El-Sahn, andD. V. Plant, “Demonstration of dispersion-enhanced phase noise in RGI CO-OFDM systems,” accepted for publication in IEEE Photon. Technol. Lett. (2012).

118. P. Rabiei, W. Namgoong, and N. Al-Dhahir, “A non-iterative technique for phase noise ICI mitigation in packet-based OFDM systems,” IEEE Trans. on Signal Processing 58, pp. 5945-5950 (2010).

119. K. Onohara, Y. Miyata, T. Sugihara, K. Kubo, H. Yoshida, and T. Mizuochi, “Soft decision FEC for 100G transport systems,” in Proc. Optical Fibre Communication Conf. 2010, OSA Tech. Dig. (CD), San Diego, CA, Paper OThL1.

120. K. Kikuchi, and K. Igarashi, “Characterization of semiconductor-laser phase noise with digital coherent receivers,” in Optical Fibre Communication Conference, OSA Technical Digest (CD) (Optical Society of America, 2011), paper OML3.

121. X. Chen, A. Al-Amin, and W. Shieh, “Characterization and monitoring of laser linewidths in coherent systems,” IEEE J. Lightwave Technol. 29, pp. 2533-2537 (2011).

122. G. Bosco, V. Curri, A. Carena, P. Poggiolini, and F. Forghieri, “On the performance of Nyquist-WDM terabit superchannels based on PM-BPSK, PM-QPSK, PM-8QAM or PM-16QAM subcarriers,” IEEE J. Lightwave Technol. 29, pp. 53-61 (2011).

123. G. Bosco, “Spectrally efficient transmission: a comparison between Nyquist-WDM and CO-OFDM approaches,” in Signal Processing in Photonic Communications, OSA Technical Digest (Optical Society of America, 2012), paper SpW3B.1.

124. Z. Benyuan, S. Chandrasekhar, X. Liu, and D. W. Peckham, “Transmission performance of a 485-Gb/s CO-OFDM superchannel with PDM-16QAM subcarriers

over ULAF and SSMF-based links," IEEE Photon. Technol. Lett. 23, pp.1400-1402 (2011).

125. J. Yu, Z. Dong, and N. Chi, "Generation, Transmission and Coherent Detection of 11.2 Tb/s (112x100Gb/s) Single Source Optical OFDM Superchannel," in Optical Fibre Communication Conference, OSA Technical Digest (CD) (Optical Society of America, 2011), paper PDPA6.

126. G. K. Chang, A. Chowdhury, Z. Jia, H. C. Chien, M. F. Huang, J. Yu, and G. Ellinas, "Key technologies of WDM-PON for future converged optical broadband access networks [Invited]," J. Opt. Commun. Netw. 1, C35-C50 (2009).

127. J.-M. Kang, and S. K. Han, "A novel hybrid WDM/SCM-PON sharing wavelength for up- and down-link using reflective semiconductor optical amplifier," IEEE Photon. Technol. Lett.18, pp. 502-504 (2006).

128. K. Kitayama, X. Wang, and N. Wada, "OCDMA over WDM-PON—Solution path to gigabit-symmetric FTTH," IEEE J. Lightwave Technol. 24, pp. 1654-1662 (2006).

129. N. Cvijetic, "OFDM for next-generation optical access networks," IEEE J. Lightwave Technol. 30, pp. 384-398 (2012).

130. N. Cvijetic, M. F. Huang, E. Ip, Y. Shao, Y. K. Huang, M. Cvijetic, and T. Wang, "1.92Tb/s coherent DWDM-OFDMA-PON with no high-speed ONU-side electronics over 100km SSMF and 1:64 passive split," Opt. Express 19, pp. 24540-24545 (2011).

131. N. Cvijetic, M. F. Huang, E. Ip, Y. K. Huang, D. Qian, and T. Wang, "1.2 Tb/s symmetric WDM-OFDMA-PON over 90 km straight SSMF and 1:32 passive split with digitally-selective ONUs and coherent receiver OLT," in Optical Fibre Communication Conference, OSA Technical Digest (Optical Society of America, 2011), paper PDPD7.